Biological production and carbon sequestration functions in estuarine and coastal ecosystems

2019

Kenta Watanabe

Contents

Abbreviations

AIC: Akaike information criterion
Cal yr BP: calendar date in years before present
CDOM: chromophoric dissolved organic matter
chl. *a*: chlorophyll *a*
CO_2: carbon dioxide
C_{org}: organic carbon
DBD: dry bulk density
D_E: euphotic zone depth
DFe: dissolved iron
DIC: dissolved inorganic carbon
DIN: dissolved inorganic nitrogen
DOC: dissolved organic carbon
DOM: dissolved organic matter
DON: dissolved organic nitrogen
DSi: dissolved silica
ECE: estuarine and coastal ecosystem
ED: embayment degree
EEMs: excitation-emission matrices
Em: emission
Ex: excitation
fCO_2: fugacity of CO_2
FDOM: fluorescent dissolved organic matter
FI: fluorescence intensity
GLM: generalized linear model
GSR: global solar radiation
H-flu: humic-type fluorescence intensity
HS: humic substances
MAR: mineral mass accumulation rate
MPB: microphytobenthos
NEP: net ecosystem production
NO_x: nitrate+nitrite
OM: organic matter
PARAFAC: parallel factor analysis
PN: particulate nitrogen
POC: particulate organic carbon
POM: particulate organic matter
RSL: relative sea-level
SAR: sediment accretion rate
TDN: total dissolved nitrogen
TN: total nitrogen
TOC: total organic carbon

Abstract

Estuarine and coastal ecosystems (ECEs) are the most productive marine ecosystems and provide the diverse and valuable functions and services. Because ECEs are the 'open' systems strongly connected with both the land and ocean, the connectivity and interactions across land–ocean gradients determine ecosystem structure, functions and processes. However, there are knowledge gaps concerning the regulating factors of the ecosystem functions in ECEs, which have complex connectivity and interactions. This thesis focuses on the nutrient and carbon dynamics in ECEs, and aims to investigate the regulating factors of the ecosystem functions, both biological production and carbon sequestration, in ECEs.

Influence of salt-wedge intrusion on ecological processes at lower trophic levels in the Yura River estuary, Japan

To examine the influence of salt-wedge intrusion on ecological processes at lower trophic levels in estuaries, seasonal variability in the nutrients, phytoplankton biomass (chlorophyll *a*), zooplankton density, and composition was investigated in the Yura River, which is flowing into Tango Bay. Phytoplankton composition was determined under two discriminative regimes: salt-wedge regime (summer) and freshwater regime (winter). Phytoplankton from two groups bloomed simultaneously under the salt-wedge regime. Freshwater and brackish phytoplankton dominated the upper freshwater layer (~16,100 cells mL^{-1}) while marine phytoplankton were dominant below the halocline (~12,200 cells mL^{-1}). Both phytoplankton groups grew using riverine nutrients. Marine phytoplankton increased closer to the tip of the salt wedge, indicating that marine phytoplankton grew in situ in the river. The residence time of salt water increased due to the low river discharge from spring to summer, enhancing mineralization in the salt

wedge. Regenerated nutrients in the salt wedge would contribute to subsequent marine phytoplankton blooms. Copepods were more abundant in the salt wedge (~80.9 ind. L^{-1}) than in the upper freshwater layer (~14.2 ind. L^{-1}) during summer. Phytoplankton and zooplankton densities under the freshwater regime (winter; ~360 cells mL^{-1}, ~39.7 ind. L^{-1}) were lower than under the salt-wedge regime (summer). The high river discharge under the freshwater regime flushed out the salt wedge and discourages biological production in the river. Our results shows that salt-wedge intrusions change the physical conditions and nutrient dynamics, enhancing biological production in the salt-wedge estuary.

Estuarine circulation-driven entrainment of oceanic nutrients fuels coastal phytoplankton in an open coastal system in Japan

I investigated interactions among seasonal fluctuations in phytoplankton biomass, riverine nutrient flux, and the fluxes of nutrients entrained by estuarine circulation in Tango Bay, Japan, to determine the influence of freshwater inflows to an open bay on coastal phytoplankton productivity. The riverine nutrient flux was strongly regulated by river discharge. Estuarine circulation was driven by river discharge, with high fluxes of nutrients (mean nitrate+nitrite flux: 5.3±3.5 Mg [mega grams]-N day^{-1}) between winter and early spring, enhanced by nutrient supply to the surface water via vertical mixing. In contrast, low-nutrient seawater was delivered to the bay between late spring and summer (1.0±0.8 Mg-N day^{-1}). Seasonal fluctuations in phytoplankton biomass were affected by the entrained fluxes of oceanic nutrients and variation in the euphotic zone depth, and to a lesser degree by the riverine nutrient flux. Bioassays and stoichiometric analyses indicated that phytoplankton growth was limited by nitrogen and/or phosphorus. Both the entrainment of oceanic nutrients and the euphotic zone depth affected the duration and magnitude of blooms. Our findings show that, unlike semi-enclosed bays, seasonal variations in coastal phytoplankton are primarily fueled by the entrainment of oceanic nutrients

and are influenced by both freshwater inflow and coastal conditions (e.g. vertical mixing and wind events).

Iron and fluorescent dissolved organic matter in an estuarine and coastal system in Japan

Terrestrially derived dissolved organic matter (DOM) plays an important role in providing ligands that regulate iron transport to coastal ecosystems. Fluorescent DOM (FDOM) is widely used to evaluate DOM behavior, but the relationship between iron and FDOM distributions in estuarine and coastal systems is poorly understood. In this study, I investigated the distributions of dissolved iron (DFe < 0.7-μm fraction) and FDOM as measured using fluorescence excitation-emission matrices in the Yura River–Tango Bay system. The DFe distribution was not closely correlated with that of the humic-like FDOM, indicating that humic-like FDOM is not the main regulator of the DFe concentration in this system. The relatively low fluorescence intensity of humic-like FDOM demonstrated that colloidal inorganic iron was the major component of riverine DFe. More than 94% of the riverine DFe was removed by the mixing process in brackish waters, but humic-like FDOM likely supported the transport of DFe to the coastal zone.

How organic carbon derived from multiple sources contributes to carbon sequestration processes in a shallow coastal system?

Carbon captured by marine organisms helps sequester atmospheric CO_2, especially in shallow coastal ecosystems, where rates of primary production and burial of organic carbon (C_{org}) from multiple sources are high. However, linkages between the dynamics of C_{org} derived from multiple sources and carbon sequestration are poorly understood. I investigated the origin (terrestrial, phytobenthos-derived, and phytoplankton-derived) of particulate organic carbon (POC) and dissolved organic carbon (DOC) in the water column and sedimentary C_{org} using elemental, isotopic, and optical signatures in Furen Lagoon, Japan. Based on these data analyses,

I explored how C_{org} from multiple sources contributes to sequestration via storage in sediments, water column sequestration, and air–sea CO_2 exchanges, and analyzed how the contributions vary with salinity in a shallow seagrass meadow as well. The relative contribution of terrestrial POC in the water column decreased with increasing salinity, whereas autochthonous POC increased in the salinity range of 10–30. Phytoplankton-derived POC dominated the water column POC (65–95%) within this salinity range; however it was minor in the sediments (3–29%). In contrast, terrestrial and phytobenthos-derived POC were relatively minor contributors in the water column but were major contributors in the sediments (49–78% and 19–36%, respectively), indicating that terrestrial and phytobenthos-derived POC were selectively stored in the sediments. Autochthonous DOC, part of which can contribute to long-term carbon sequestration in the water column, accounted for >25% of the total water column DOC pool in the salinity range of 15–30. Autochthonous C_{org} production decreased the concentration of dissolved inorganic carbon in the water column and thereby contributed to atmospheric CO_2 uptake, except in the low-salinity zone. Our results indicate that shallow coastal ecosystems function not only as transition zones between land and ocean but also as carbon sequestration filters. They function at different timescales, depending on the salinity and C_{org} sources.

Depositional environment change and the subsequent habitat relocation affect organic carbon accumulation rates in vegetated coastal ecosystems

Vegetated coastal ecosystems are hotspots which store large amounts of organic carbon (C_{org}), and the conservation and restoration of these ecosystems are considered as important measures for mitigating the adverse effects of global climate change. Although various geophysical and biogeochemical factors control C_{org} storage in the sediment of these ecosystems, how spatiotemporal variations in the depositional environment (e.g., relative sea-level change, geological settings, habitat type) affect C_{org} accumulation rates are uncertain. In this study, I

showed that depositional environment changed and the subsequent habitat relocation regulated C_{org} accumulation rates and the composition of C_{org} sources in boreal contiguous seagrass-saltmarsh habitats by using the historical depositional records. In particular, C_{org} accumulation rates were enhanced in subtidal zones during times of relative sea-level rise, which were caused by post-seismic land subsidence and climate change. Our findings identify historical analogues for the future impact of relative sea-level rise driven by global climate change on rates of C_{org} sequestration in coastal habitats.

Chapter 1

General introduction

Ecological functions of estuarine and coastal ecosystems

Ecosystems provide a large number of valuable goods and services to humans, which are referred as "ecosystem services" (Costanza et al., 1997). Ecosystem services are defined as the benefits which people obtain from ecosystems by the Millennium Ecosystem Assessment (MEA) (MEA, 2005). Ecosystem services are generated by ecosystem functions and processes. Therefore, spatial and temporal variations in ecosystem functions and processes, which are controlled by the abiotic and biotic structure, regulate ecosystem services (Barbier et al., 2011).

The global value of ecosystem services was estimated to be approximately $ 33 trillion per year in 1995 $US, which is significantly higher than global GDP at that time, by Costanza et al. (1997). This epoch-making global valuation stimulated subsequent studies about ecosystem services, and a number of projects are working for better understanding ecosystem services and natural capital (e.g., MEA, 2005; TEEB, 2010; WBCSD, 2011; Halpern et al., 2012). A recent study has updated the global estimate to be $ 125 trillion per year in 2007 $US, which is higher than the estimate by Costanza et al. (1997) mainly due to additional valuations of some services (Costanza et al., 2014).

Estuarine and coastal ecosystems (ECEs) are the most productive marine ecosystems (Bianchi, 2007), underlying the diverse and valuable functions (Barbier et al., 2011). The global value of ECEs, which include estuaries, seagrass and algae beds, coral reefs, shelf, tidal marsh and mangroves, was estimated to be $ 53 trillion per year in 2007 $US which is almost half of the total global estimate in spite of the narrow area (Costanza et al., 2014). ECEs provide various ecosystem services such as maintenance of fisheries, food production, water purification,

climate regulation, coastal protection, and cultural services (Barbier et al., 2011). These ecosystem services were generated by ecosystem functions and processes like biological productivity, nursery ground provision, nutrient cycling, carbon sequestration (Barbier et al., 2011).

ECEs are recognized as the most 'open' systems strongly connected with both the terrestrial and oceanic environments (Elliott and Whitfield, 2011). The connectivity and interaction across land–ocean gradients affect ecosystem structure, functions and processes (Barbier et al., 2011). However, there remain knowledge gaps concerning the regulating factors of the ecosystem functions in ECEs, which have complex connectivity and interactions (Watanabe et al., 2018). In this thesis, I will focus on two ecosystem functions of ECEs, biological production and carbon sequestration for the following reasons and investigate the regulating factors of these functions in ECEs.

Biological production

Biological production is a fundamental function underlying the key ecosystem services of ECEs, such food production and maintenance of fisheries. In particular, phytoplankton play important roles as a primary producer and support higher trophic levels of marine food webs through a bottom-up effect (Kimmerer, 2002; Cloern and Jassby, 2008; Connolly et al., 2009; Kostecki et al., 2010). Because nutrient availability often limits phytoplankton primary production in ECEs, spatial and temporal variations in phytoplankton primary production are closely linked with nutrient dynamics in ECEs (Cloern and Jassby, 2008). Riverine input, oceanographic conditions, and geomorphological settings indirectly affect phytoplankton primary production as regulators of nutrient dynamics. The connectivity between individual ECEs (e.g., estuaries, open coasts, vegetated habitats) also have important implications for

assessing the regulating factors of biological production function (Barbier et al., 2011; Watanabe et al., 2018). A number of studies has addressed the regulating factors of biological production in individual ECEs; however, the biological production function and its regulators are still poorly assessed through the network among these ecosystems (Itoh et al., 2018; Watanabe et al., 2018).

Carbon sequestration

ECEs have an ecosystem function for sequestering atmospheric carbon dioxide (CO_2) into the ecosystems. Among the most efficient ecosystems that have carbon sequestration function are vegetated coastal ecosystems, which include seagrass meadows, saltmarshes, and mangroves (Nellemann et al., 2009). These ecosystems are known as "blue carbon" ecosystems (McLeod et al., 2011; Duarte et al., 2013), and an increasing number of studies has investigated the mechanism of carbon sequestration and quantified carbon stocks and accumulation rates over the global, regional, and local scales in a recent decade (McLeod et al., 2011; Duarte et al., 2013; Hori and Kuwae, 2017; Macreadie et al., 2017; Kuwae and Hori, 2019). Processes for sequestering atmospheric CO_2 into these ecosystems include air–water CO_2 gas exchange, carbon sequestration in water column, and carbon storage in sediments (Kuwae et al., 2016; Hori and Kuwae, 2017; Kuwae and Hori, 2019). Both organic and inorganic carbon dynamics in these processes should be quantified to evaluate their controlling factors. Because blue carbon ecosystems are located in transition zones between terrestrial systems and the ocean, allochthonous carbon also play substantial role in these processes. However, the roles of carbon derived from multiple sources in coastal carbon dynamics in response to carbon sequestration function are still poorly understood (Bauer et al., 2013).

Nutrient and carbon dynamics, biological production, and carbon sequestration in ECEs

This thesis will focus on the nutrient and carbon dynamics in ECEs, and aim to investigate the regulating factors of the ecosystem functions, both biological production and carbon sequestration, in these ecosystems. I select two types of coastal ecosystems and conduct field surveys and subsequent analyses to answer the following questions.

1) What factors determine biological production in a continuum between a river, an estuary, and an adjacent coastal zone? (Chapters 2, 3, and 4)

In Chapters 2, 3, and 4, I investigated the relationships between seasonal fluctuations in river discharge and the behaviors of nutrients, i.e. nitrogen, phosphorus, silica and iron. And then, I assessed the controlling factors which determined the spatiotemporal changes in biological production in the continuum ecosystem. The model site of these chapters was the Yura River and the Tango Bay coastal zone in Japan. The strong seasonality of the river discharge shapes the temporal and spatial gradients of physical, hydrological, chemical, and biological characteristics (Kasai et al., 2010; Funahashi et al., 2013). This geological feature is suitable for accumulating data to reveal the factors determining biological production in a river–coastal zone continuum. In chapter 2, I investigated how the changes in physicochemical structure due to the fluctuations in river discharge determined the biological production in the downstream of the Yura River estuary. In chapter 3, the influence of riverine input on coastal phytoplankton dynamics was evaluated by quantifying riverine and oceanic nutrient fluxes driven by river water inflow in the Tango Bay coastal zone. Also, the riverine supply of iron to the coastal zone was examined in chapter 4.

2) What factors affect carbon sequestration processes in shallow coastal ecosystems? (Chapters 5 and 6)

In Chapters 5 and 6, I investigated the dynamics of organic and inorganic carbon derived from multiple sources and its implications to carbon sequestration processes in shallow coastal ecosystems. The model sites of these chapters were Furen and Hichirippu lagoons in eastern Hokkaido in Japan. These lagoons have abundant seagrass meadows and are adjacent to surrounding saltmarshes. Because the amount of freshwater input is considerably different between these lagoons, the effect of carbon loads from land could be easily measured. These lagoons are suitable model sites to evaluate the behavior of carbon derived from multiple sources. In chapter 5, the origin and fate of carbon were quantified to detect the factors affecting carbon sequestration processes in a river-influenced seagrass meadow. The source of buried organic carbon and carbon accumulation rate were measured to evaluate the controlling factors of long-term carbon sequestration in chapter 6.

Chapter 2:

Influence of salt-wedge intrusion on ecological processes at lower trophic levels in the Yura River estuary, Japan

Introduction

Estuaries are the most productive areas among marine ecosystems because they receive rich riverine supplies of nutrients. Therefore, estuaries provide important ecosystem services, such as food production and nutrient cycling (Costanza et al., 1997). Moreover, estuaries are interfaces between freshwater and seawater, providing complex physicochemical habitats to plants and animals.

Salt-wedge (highly stratified) estuaries have relatively deep river channels and a micro-tidal environment, leading to the absence of tide-induced turbulence and allowing a strong density stratification to be maintained (Haralambidou et al., 2010). In salt-wedge estuaries, a salt-wedge regime is established during low river flows, whereas during high flows the salt wedge is flushed away and the estuary is occupied by freshwater (a freshwater regime). Under a salt-wedge regime, a sharp halocline is developed, separating the upper low salinity layer from the high salinity bottom layer. The effects of salt-wedge intrusions on biogeochemical parameters have been the focus of many studies. Recently, dam construction and increases in water use due to human activities have been causing declines in river discharge throughout the world (e.g., Sierra et al., 2004). Declines in river discharge encourage stratification and salt-wedge intrusion into estuaries (Sierra et al., 2004; Jang et al., 2012). Changes in precipitation and river discharge owing to climate change (e.g., Bergström et al., 2001; Graham, 2004) can alter the frequency of floods and the intensity of salt-wedge intrusions.

Salt-wedge estuaries present strong and highly variable gradients in biogeochemical environments. Studies on the spatial distributions of nutrients (Falco et al., 2010; Haralambidou et al., 2010) and organic matter (Zutic and Legovic, 1987; Cauwet, 1991; Fuks et al., 1991; Legovic et al., 1994) have suggested that the interface between the upper freshwater and the lower saline water is important for structuring primary production in estuaries.

Vertical variability in physical and chemical properties along a salinity gradient has a decisive influence on phytoplankton community composition and primary production (Muylaert and Sabbe, 1999). Aggregations of phytoplankton have been observed as thin layers at the interface between freshwater and seawater in salt-wedge estuaries (Legovic et al., 1994; González et al., 2007; Kasai et al., 2010). Stratification would be essential for blooms in this type of estuary, but the process of nutrient supply and other limiting factors for blooms have not been studied sufficiently. Although the salinity range is so wide that salt-wedge estuaries can provide habitats for freshwater, brackish, and seawater phytoplankton (Chan and Hamilton, 2001), studies on spatial variation in phytoplankton composition related to physicochemical properties have been limited (e.g., González et al., 2007). Moreover, ecological links among physicochemical structure, primary production, and zooplankton production in salt-wedge estuaries remain unknown.

The lower reach of the Yura River is a salt-wedge estuary that flows into the Sea of Japan. From May to December, the river discharge is generally low, and therefore, the salt wedge frequently extends up to 20 km upstream. Because the Yura River estuary provides important nursery grounds for many fishes, including commercial fish species (Minami, 1982; Fuji et al., 2010), determining the mechanisms affecting ecological processes at lower trophic levels is important. The mechanism of seawater intrusion into the river and the relationship between seawater intrusion and chlorophyll *a* (chl. *a*) dynamics in the Yura River estuary was reported

by Kasai et al. (2010). They showed that water stratification caused by seawater intrusion was an important factor affecting phytoplankton blooms in summer. However, that paper only used chl. *a* as an index of phytoplankton biomass; the species composition and distribution of phytoplankton and changes in nutrient dynamics associated with salt-wedge intrusions have not been examined. In this study, the effects of salt-wedge intrusions on ecological processes at lower trophic levels, from nutrient consumption to zooplankton production, were examined.

The objectives of this study were to determine the sources of nutrients for phytoplankton in the estuary, and to examine the temporal and spatial changes in phytoplankton and zooplankton. The physical conditions of the Yura River estuary can be divided roughly into two regimes: a salt-wedge regime (summer) and a freshwater regime (winter). In this study, I determined the composition of the phytoplankton community in the downstream portion of the Yura River under both of these two distinct regimes, and considered the relationship between salt-wedge intrusions and phytoplankton succession. The seasonal changes in phytoplankton biomass (chl. *a*) and zooplankton density with the seasonal dynamics of saltwater intrusions were compared to investigate the effects of salt-wedge intrusions on biological production. I hypothesized that marine phytoplankton populations would increase by using riverine nutrients under the salt-wedge regime. In addition, I hypothesized that zooplankton population would increase following marine phytoplankton blooms.

Materials and methods

Study area

The Yura River, with a total length of 146 km, is a major river that flows into Tango Bay, Sea of Japan (Fig. 2-1). It has a total catchment area of 1880 km^2 and an annual average river discharge of less than 50 $m^3\ s^{-1}$ (Kasai et al., 2010). Forests cover 81% of the total catchment

area. On the Sea of Japan side, northwesterly monsoons from the Eurasian Continent bring heavy snow in winter. It also has high precipitation during the rainy season from June to July. However, outside of the rainy season, precipitation is generally low from May to December. Therefore, river discharge is high during winter to spring (January–April) and the rainy season (June–July) because of snowmelt and high precipitation, while it is generally low from early summer to autumn (May, August–December). The Yura River estuary is classified as a micro-tidal estuary with a spring tidal range of less than 0.5 m. The river discharge is generally low and the sea level is high from May to December, except during the rainy season; therefore, the salt wedge often extends up to 20 km upstream. In contrast, from January to April, river discharge is high and the salt wedge is rarely observed. These seasonal hydrological changes influence the biogeochemical processes in the estuary.

Field surveys and water sample analyses

Field surveys were conducted in the Yura River estuary, which consists of the downstream portion of the Yura River and the shallow Tango Bay coastal zone connected to the river mouth. Six stations were set between a point 17 km upstream and the mouth of the Yura River, and two stations were located at depths of 5 m (T1) and 10 m (T2) in the coastal zone (Fig. 2-1). Monthly surveys were conducted from January 2007 to March 2008 (except for October 2007 in the river and November 2007 in the coastal zone because of bad weather). Vertical profiles of water temperature, salinity, and chlorophyll fluorescence were measured with a conductivity/temperature/depth (CTD) profiler (Compact-CTD, Alec Electronics, Kobe, Japan) at each station. Dissolved oxygen (O_2) concentrations were measured using an environmental monitoring system (YSI 556 MPS, YSI Incorporated, Yellow Springs, OH, USA) starting in May 2007 at the river stations (Y1, Y2, Y4, and Y6). Water samples were taken from the

surface, middle, and bottom layers by 2- or 5-L Van Dorn water samplers at Stations Y1, Y2, Y4, Y6, T1, and T2. Middle layer samples were taken at the median depth at each station. All water samples were filtered through precombusted GF/F glass fiber filters (Whatman, Maidstone, Kent, UK) to analyze chl. *a* concentrations. The filters were extracted in the dark for 12 h in 90% acetone and chl. *a* concentrations were measured using a calibrated fluorometer (Trilogy, Turner Designs, Sunnyvale, CA, USA). Water samples taken from July 2007 to March 2008 were used for nutrient (NO_3^-, NO_2^-, NH_4^+, PO_4^{3-}) concentration analyses. Samples for nutrient analyses were filtered with 0.45 μM filters (Dismic filter, Advantec, Durham, NC, USA). Nutrient concentrations in filtered samples were measured using an Auto-Analyzer (TRAACS 2000, BL-Tec, Osaka, Japan).

Approach for estimating changes in nutrient concentrations

To evaluate changes in nutrient concentrations, the difference between the observed concentration of an element (X) and its predicted conservative concentration (X_{mix}) was calculated as the biological reduction or addition (ΔX) at the river station, i.e., $\Delta X = X - X_{mix}$. Concentrations were determined for NO_3^-, NO_2^-, NH_4^+, DIN ($NO_3^- + NO_2^- + NH_4^+$), and PO_4^{3-}. Predicted nutrient concentrations (X_{mix}) were estimated using a linear salinity mixing model for each survey with two endmembers (Kasai et al., 2010). The surface concentrations at the most upper station, Y6, were used as the riverine endmember for nutrients, and the bottom concentrations at the coastal station, T2, were used as the marine endmember. As no inputs from large tributaries occur in the survey area, ΔX is mainly determined by biological and/or chemical processes in the downstream portion of the river. ΔX in each layer was related with physicochemical parameters (salinity, O_2, and chl. *a*) using the standard Pearson correlation method.

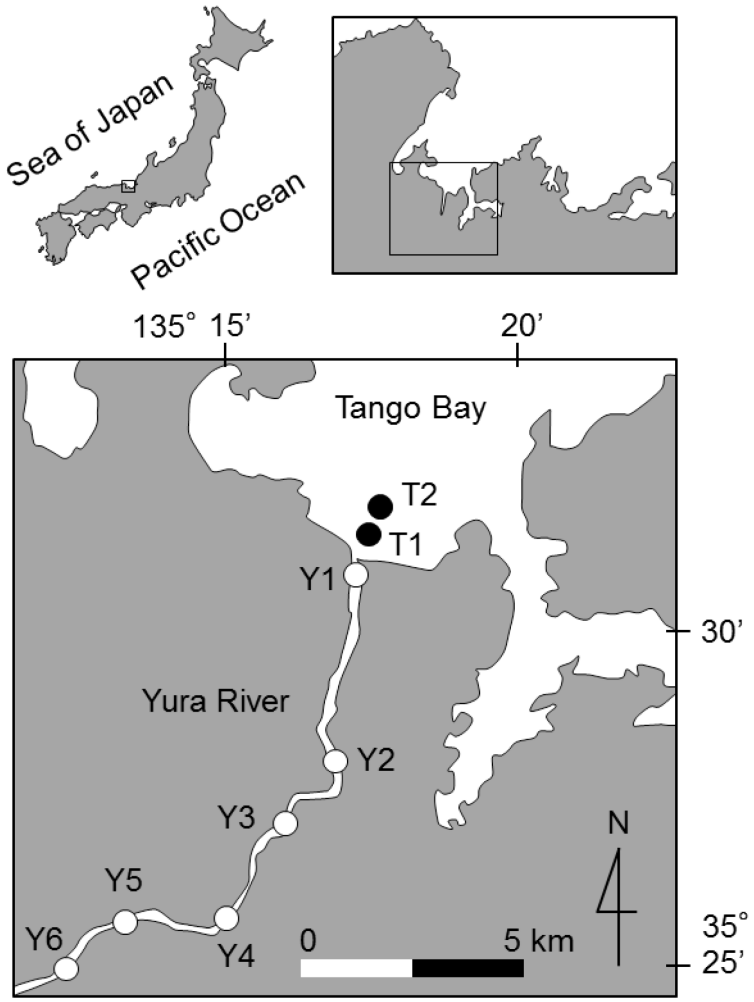

Fig. 2-1. Yura River estuary and study sites, including river stations (○) and coastal stations (●).

Phytoplankton identification and counts

Water samples were taken from the surface, middle, and bottom layers using a 2-L Van Dorn water sampler on 19 August 2010 and 21 January 2011. Using these water samples, phytoplankton genera were identified and the number of cells was counted at river stations Y1, Y2, and Y4 (Fig. 2-1). Vertical profiles of water temperature, salinity, chlorophyll fluorescence (Compact-CTD, Alec Electronics), and photon flux density (MDS MkV-L, Alec Electronics) were measured at each station. Middle layer samples were taken from just below the halocline, which corresponded to the chlorophyll fluorescence maximum layer. All water samples were filtered through precombusted Whatman GF/F glass fiber filters to analyze the chl. *a* concentration with a fluorometer (Trilogy, Turner Designs). The chlorophyll fluorescence obtained by the CTD profiler was calibrated using the measured chl. *a* concentrations. Samples for cell counts were preserved with glutaraldehyde solution at 1%. Phytoplankton were identified to the genus or family level and cells were counted under an optical microscope (BX50, Olympus, Tokyo, Japan).

Zooplankton identification and counts

Zooplankton sampling was performed from January to December 2007 at Y1, Y2, Y4, and T2 (Fig. 2-1). In January (T2), April (Y1), August (Y1), and December (Y1, Y2, and Y4), sampling data were missing because of bad weather or mechanical problems. Samples were collected with a 200-μm mesh net (60 cm diameter) fitted with a flowmeter by parallel hauls in the near bottom and surface layers for 5 min. Net collections were preserved in a 5% formaldehyde–seawater solution. Counts and species identification were performed using inverted microscopes. Counts and identification were carried out using concentrated subsamples to 100 individuals, and then the density of zooplankton was calculated.

Results

Spatial and temporal distributions of biochemical parameters

Bottom salinity data indicated that the salt wedge intruded into the river through the bottom layer from January 2007 to March 2008, with the exception of the periods from June to July 2007 (Fig. 2-2a) and February to March 2008. The salt wedge in the downstream portion of the Yura River retreated when the river discharge was high due to high precipitation in the rainy season or snowmelt in winter. The mean column chl. *a* concentration increased when the salt wedge stagnated in the downstream portion of the river from August to September (Fig. 2-2a).

The salt wedge intruded up to 17 km upstream and salinity in the bottom layer was greater than 30 at all stations on 22–23 August 2007 (Fig. 2-3). The salt-wedge intrusion had a strong effect on the distributions of chemical and biological parameters along the Yura River estuary (Fig. 2-3). O_2 was low in the salt wedge and hypoxic conditions (O_2 < 100 μM) were observed. O_2 concentrations in the bottom layer were lower at the upstream station than at the river mouth. $NO_3^- + NO_2^-$ was clearly supplied by the river and the concentration in the surface layer was 10 times higher than that in the bottom layer when the salt wedge intruded. In contrast, NH_4^+ concentrations were obviously higher in the bottom layer than in the surface layer. PO_4^{3-} was high in the surface freshwater and in the bottom water. The maximum areas of the NH_4^+ and PO_4^{3-} concentrations in the deepest zone were linked with the bottom hypoxic zone in the downstream portion of the river.

When the salt wedge intruded intensively, chl. *a* concentrations were high, particularly in surface waters near the river mouth and in the middle layer in the river (Fig. 2-3). The chlorophyll maximum formed just below the halocline. The highest concentration was 33.8 μg L^{-1} in the middle layer at station Y6, which was near the tip of the salt wedge. In the coastal

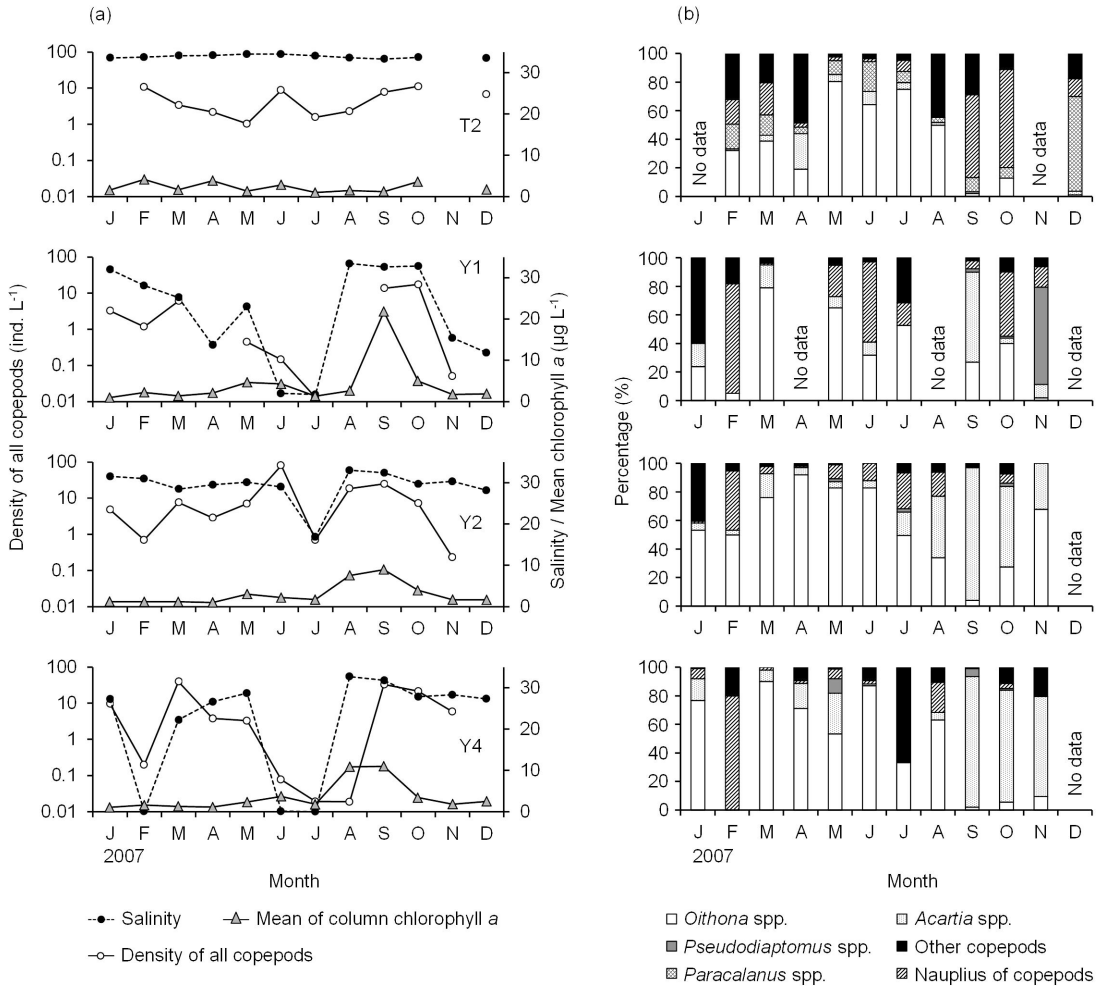

Fig. 2-2. Seasonal variations in (**a**) copepod density and salinity in the bottom layer and mean chlorophyll *a* concentrations in the water column; (**b**) copepod composition in the bottom layer at stations T2, Y1, Y2, and Y4 from January to December 2007.

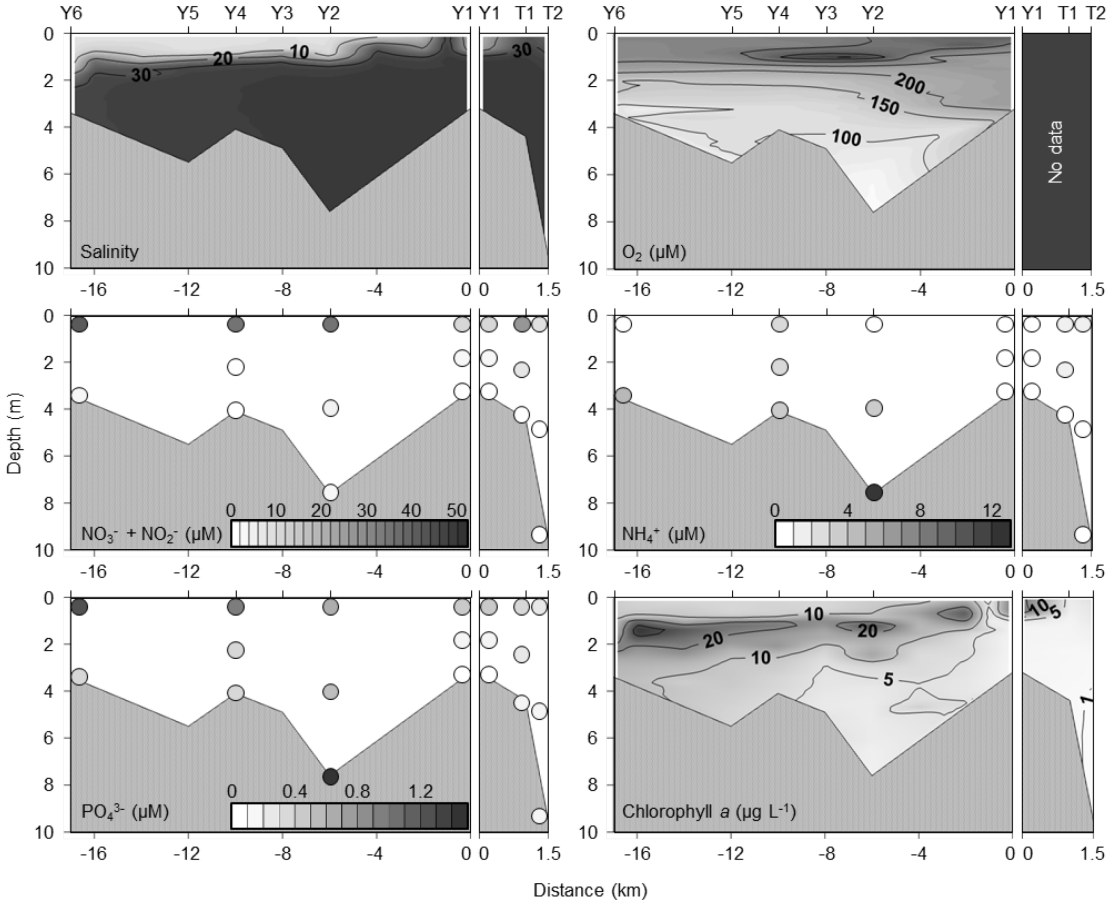

Fig. 2-3. Longitudinal transects of salinity, dissolved oxygen (O_2), NO_3^- + NO_2^-, NH_4^+, PO_4^{3-}, and chlorophyll *a* along the Yura River estuary on 22–23 August 2007.

zone, the chl. *a* concentration (mean value 1.5 μg L^{-1}) was lower than in the river. Nutrient concentrations were also low in the coastal zone, especially in the middle and bottom layers.

The salt wedge intruded slightly on 28–29 January 2008, but salt water only remained at the bottom of station Y2, with almost the entire downstream portion of the river occupied by freshwater (Fig. 2-4). O_2 concentrations were higher than under the salt-wedge regime and a bottom hypoxic zone was not observed (Figs. 2-3 and 2-4). The distribution of $NO_3^- + NO_2^-$ was linked with the presence of freshwater and exceeded 30 μM in the river. NH_4^+ concentrations were less than 4 μM and increased slightly in the lower oxygen zone at station Y2. PO_4^{3-} was high at the river mouth and in the deepest zone (station Y2).

Under the freshwater regime, chl. *a* concentrations were below 3 μg L^{-1} in the river (Fig. 2-4). In contrast, chl. *a* concentrations were above 4 μg L^{-1} in the middle layer of the coastal zone. Nutrient concentrations were also higher in surface and middle layers in winter than in summer in the coastal zone (Figs. 2-3 and 2-4).

Distribution and community composition of phytoplankton in the river

Salt-wedge water intruded up to station Y6 on 19 August 2010 and the halocline was formed at a depth of 1.5–2.0 m (Fig. 2-5). Photon flux density declined to below 1% at a depth of 4.5 m. The distribution of chl. *a* and phytoplankton composition were variable both vertically and horizontally (Fig. 2-5). The chl. *a* concentration and cell density were high in the surface freshwater layer, but low in the saline deep layer at station Y1 (river mouth). In the freshwater layer, phytoplankton blooms were dominated by colonial cyanobacteria, Chlorophyceae, and brackish diatoms (*Cyclotella* spp.), and the cell density reached 16,100 cells mL^{-1}. In the saline layer, although marine and brackish centric diatoms (*Chaetoceros* spp. and *Cyclotella* spp.) were dominant, the cell density was considerably lower than in the surface layer (<2,800 cells

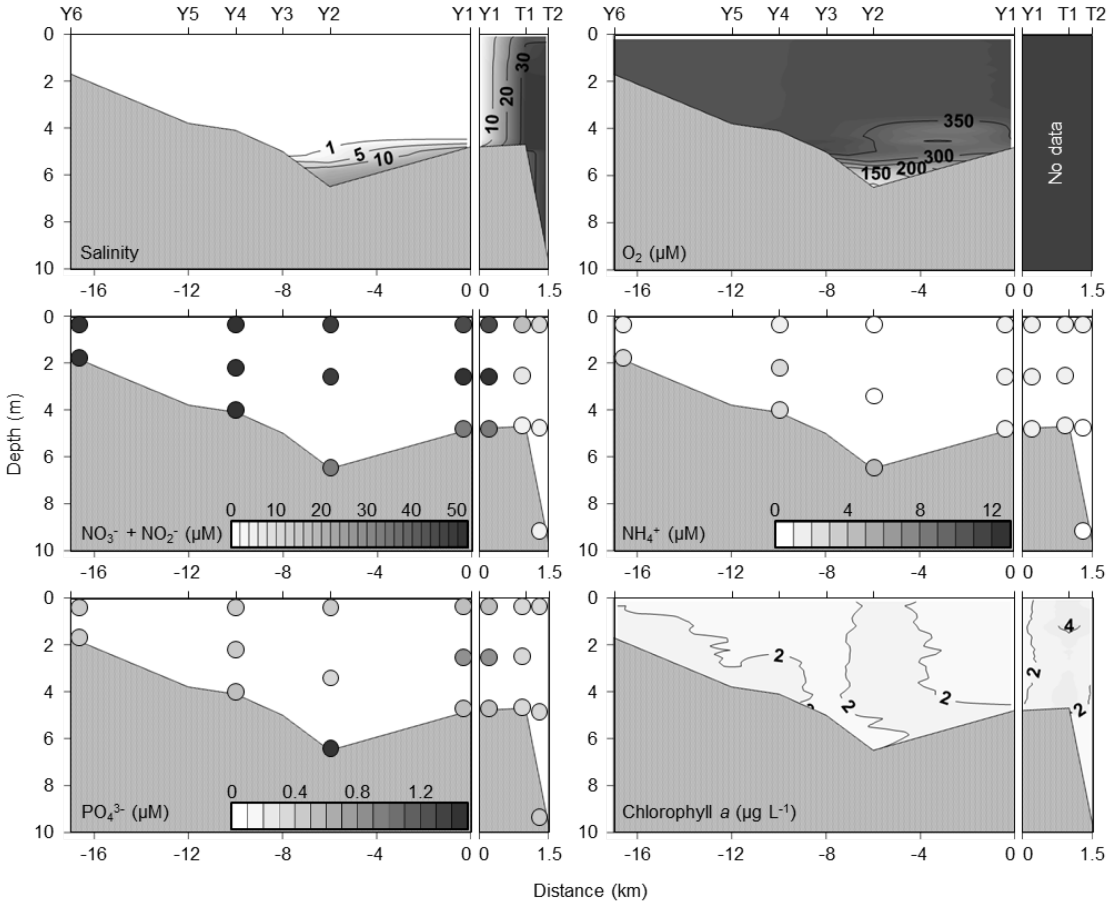

Fig. 2-4. Longitudinal transects of salinity, dissolved oxygen (O_2), NO_3^- + NO_2^-, NH_4^+, PO_4^{3-}, and chlorophyll *a* along the Yura River estuary on 28–29 January 2008.

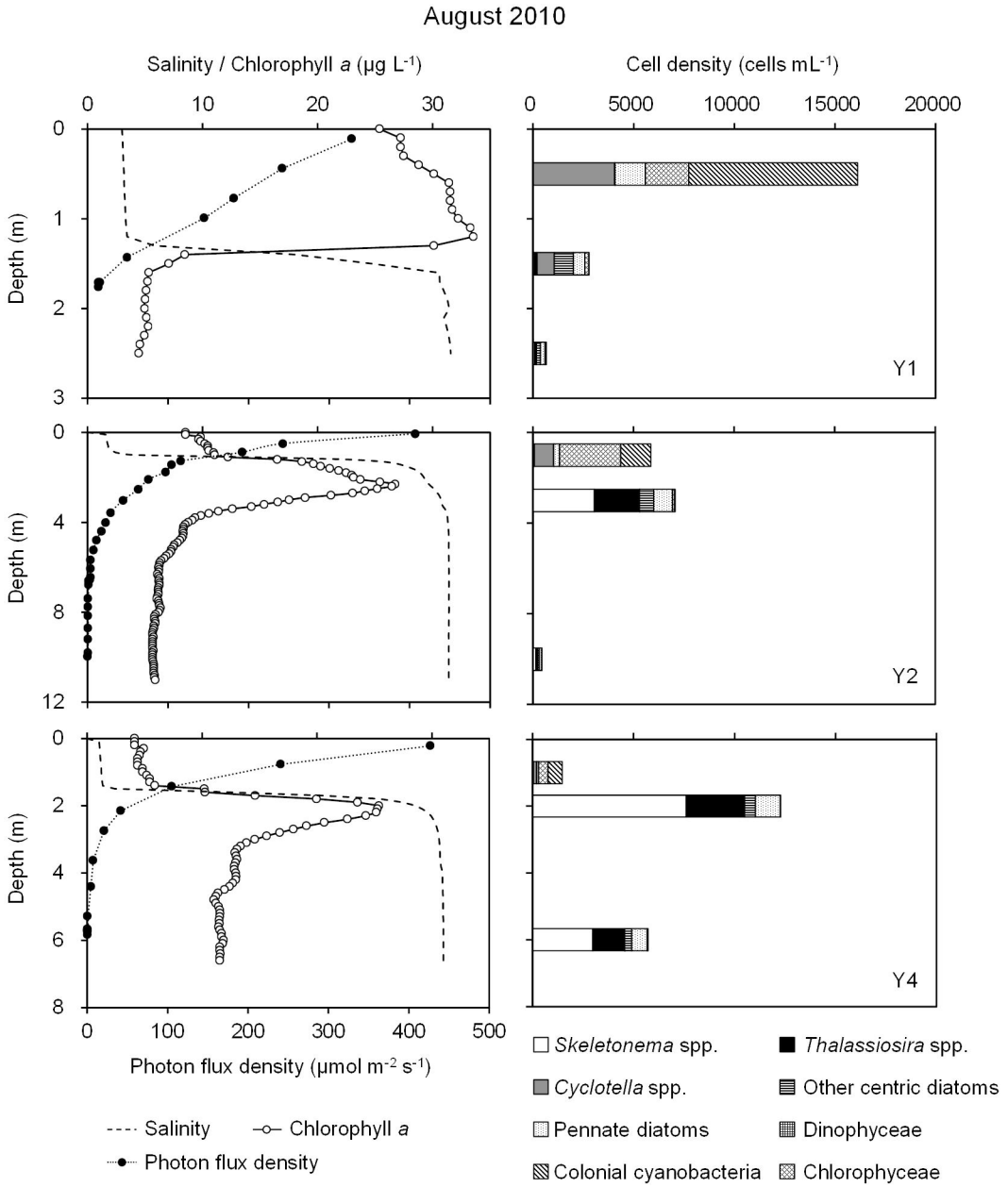

Fig. 2-5. Vertical profiles of salinity, chlorophyll *a*, photon flux density, and the cell density of phytoplankton on 19 August 2010 at stations Y1, Y2, and Y4.

mL^{-1}). At station Y2, Chlorophyceae, colonial cyanobacteria, and *Cyclotella* spp. were mainly observed in the surface layer and the cell density (5,800 cells mL^{-1}) was 26% of the level at the river mouth (station Y1). Just below the halocline, the chlorophyll maximum was observed and marine diatoms (*Skeletonema* spp., *Talassiosira* spp., and *Pseudo-nitzschia* spp.) formed blooms (cell density was 7,000 cells mL^{-1}). Phytoplankton composition in the bottom layer resembled that in the chlorophyll maximum layer, but the cell density was <500 cells mL^{-1}. At the upper station, Y4, the cell density in the freshwater layer (1,400 cells mL^{-1}) was lower than at the downstream stations. Marine diatoms bloomed in the chlorophyll maximum layer and the cell density was 12,200 cells mL^{-1}. Cell density in the bottom layer (5,700 cells mL^{-1}) was higher than at the downstream stations.

Freshwater occupied the downstream portion of the river and seawater only remained in the deep zone (Station Y2) on 21 January 2011 (Fig. 2-6). The euphotic layer, where the photon density was over 1%, was shallower than 10 m. The chl. *a* concentration was less than 1.0 μg L^{-1} in all layers. The highest phytoplankton cell density was 360 cells mL^{-1}, which was only 2% of the maximum cell density in summer (16,100 cells mL^{-1}). The dominant groups in the surface layer were pennate diatoms and colonial cyanobacteria (Fig. 2-6). In contrast, in the saline layer, marine diatoms such as *Skeletonema* spp. rarely appeared at station Y2.

Changes in nutrient concentrations in the river

ΔNO_3^- was generally negative in all three layers of low-salinity water (Fig. 2-7a). The reduction in NO_3^- was particularly notable in the surface and middle layers within a salinity range of 0–15. ΔNO_3^- tended to be negative when the O_2 concentration was above 150 μM, whereas ΔNO_3^- was frequently positive or null when O_2 was below 150 μM (Fig. 2-7b). Additionally, ΔNO_3^- in the surface layer decreased with the chl. *a* concentration ($r = -0.42$, $p <$

0.05; Table 2-1), but the relationships between ΔNO_3^- and chl. *a* concentrations in the middle and bottom layers were not significant (Fig. 2-7c, Table 2-1). ΔNO_2^- and ΔNH_4^+ were high in the middle and bottom layers in high salinity water (Fig. 2-7d, g). ΔNO_2^- and ΔNH_4^+ increased with reductions in O_2 (Fig. 2-7e, h, Table 2-1). ΔNO_2^- and ΔNH_4^+ became near null with high chl. *a* concentrations (Fig. 2-7f, i). ΔDIN was frequently negative under low salinity and high O_2 conditions (Fig. 2-7j, k). In contrast, under high salinity and low O_2 conditions, ΔDIN increased in the middle and bottom layers. ΔDIN decreased with the chl. *a* concentration ($r = -0.46$, $p < 0.01$; Table 2-1). ΔPO_4^{3-} increased when O_2 was below 150 μM with high salinity in the middle and bottom layers (Fig. 2-7m, n), indicating elusion from hypoxic bottom sediments. ΔPO_4^{3-} in the surface layer decreased with the chl. *a* concentration ($r = -0.72$, $p < 0.001$; Table 2-1).

Seasonal changes in the copepod community

The zooplankton community was dominated by copepods in 2007. Copepod density in the downstream portion of the Yura River was variable along the salinity gradient (Fig. 2-8). In the surface layer with low salinity, copepod density was low (0.001–14.2 ind. L^{-1}) and copepod density increased with salinity. In the bottom layer, copepods were more abundant than in the surface layer, and the maximum density was 80.9 ind. L^{-1} with high temperature.

Copepod density in the bottom layer displayed temporal and spatial variability in the estuary. It was significantly affected by salt-wedge dynamics (Fig. 2-2). During the rainy season (June–July) and winter (January–March), high river discharge flushed out the saline water, especially at stations Y1 and Y4, which were shallow and upper sites, respectively. Chl. *a* concentrations in the river were low during this period (0.9–2.2 μg L^{-1}). Copepod density decreased at these stations during high flow seasons. In contrast, at the deeper riverine station, Y2 (>7 m depth), salt water remained at the bottom and copepods were relatively abundant

throughout the year. The maximum density was 80.9 ind. L^{-1} at station Y2 on 19 June 2007. From summer to autumn (August–October), the frequency of flush due to heavy rain was so low that salt water stagnated for long periods in the river. Chl. *a* concentrations from summer to autumn (3.3–21.7 μg L^{-1}) were higher than in winter. Copepod density was high at every river site during this period. Copepod densities were 13.7 ind. L^{-1} at Y1, 24.7 ind. L^{-1} at Y2, and 32.8 ind. L^{-1} at Y4 in September.

In the downstream portion of the Yura River, copepods from three genera, *Oithona* spp., *Acartia* spp., and *Pseudodiaptomus* spp., were dominant and abundant (Fig. 2-2b). *Oithona* spp. (dominated by *O. davisae*) was abundant in salt water and was particularly dominant when temperatures ranged from 10ºC to 20ºC during January–July (Figs. 2-2 and 2-8). In contrast, *Acartia* spp. (dominated by *A. tsuensis*) also appeared in high salinity water and apparently increased under high temperatures (>25ºC) from August to October (Figs. 2-2 and 2-8). *Pseudodiaptomus* spp. were also abundant in salt water (Fig. 2-8).

In the coastal zone (station T2), the density of all copepods showed seasonal variability, being abundant in winter (Fig. 2-2). The density of all copepods increased above 10.0 ind. L^{-1} in February and October 2007. Chl. *a* concentrations were also high in February (4.1 μg L^{-1}) and October (3.6 μg L^{-1}). In contrast, from May to September, chl. *a* concentrations were consistently low (0.9–2.8 μg L^{-1}). During this period, except for June and September, the density of copepods (1.0–2.3 ind. L^{-1}) was slightly lower than during autumn and winter. The copepod community was dominated by *Paracalanus* spp. in winter and by *Oithona* spp. in summer. From autumn to winter, copepod nauplii were abundant in the community.

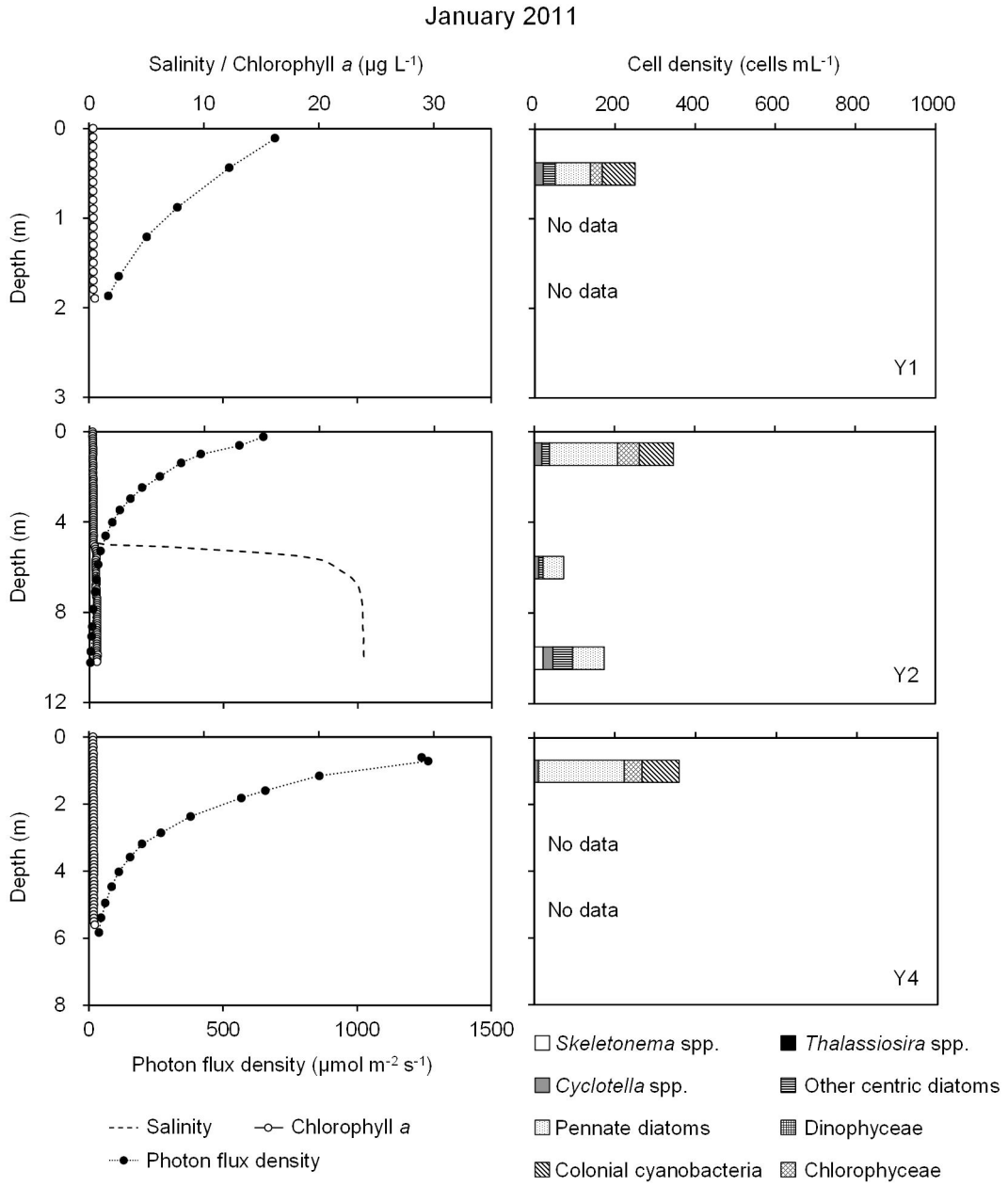

Fig. 2-6. Vertical profiles of salinity, chlorophyll *a*, photon flux density, and cell density of phytoplankton on 21 January 2011 at stations Y1, Y2, and Y4.

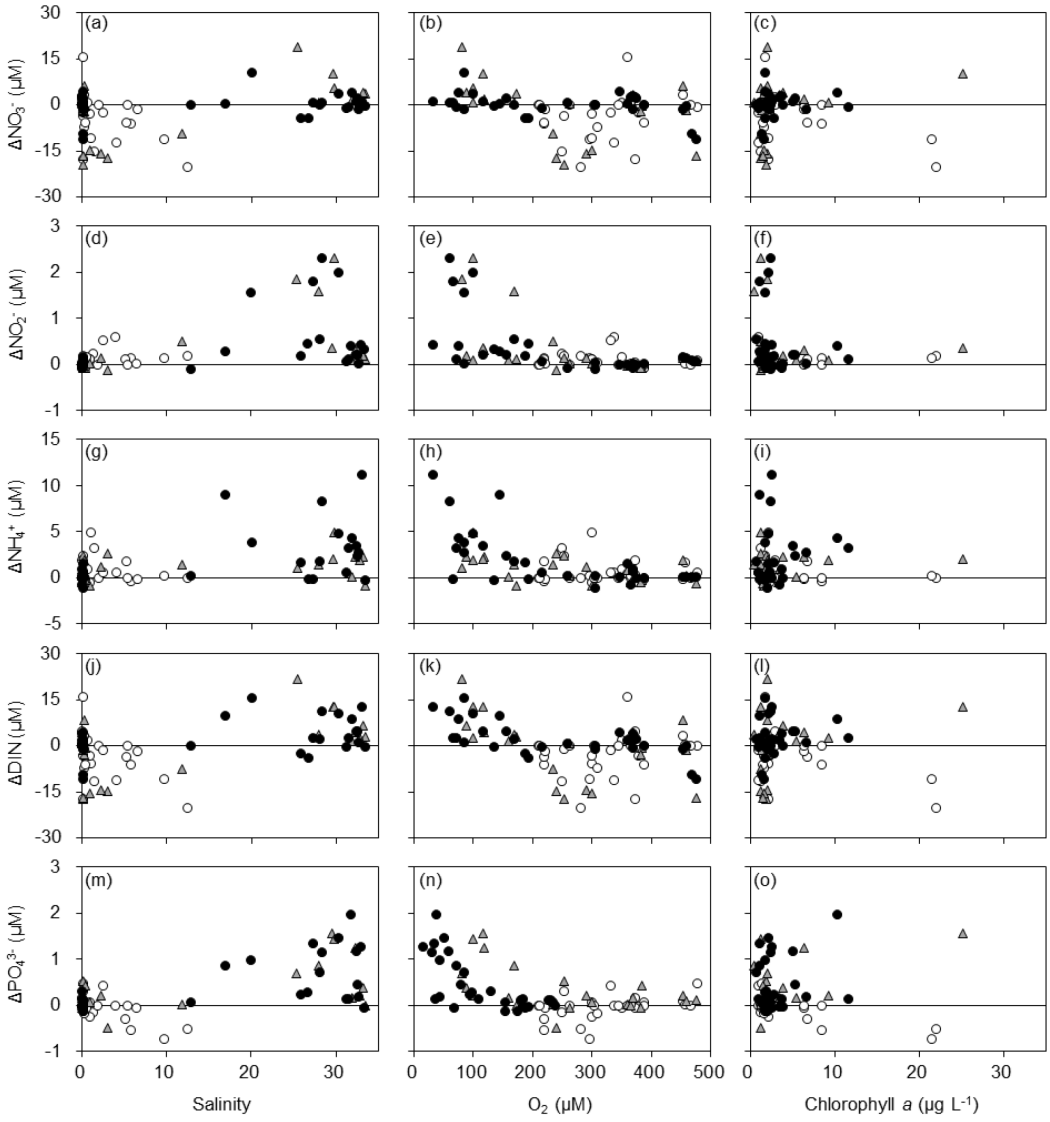

Fig. 2-7. Relationships between ΔX values of nutrients and physicochemical parameters in the downstream portion of the Yura River. Open circle: surface layer. Gray triangle: middle layer. Solid circle: bottom layer.

Table 2-1. Pearson correlation coefficients (*r*) between ΔX values and physicochemical parameters along the downstream portion of the Yura River. Values for *r* are only displayed when the overall regression model was statistically significant. *, $p < 0.05$; **, $p < 0.01$; ***, $p < 0.001$; n.s., not significant.

Parameter	Layer	n	ΔNO_3^-		ΔNO_2^-		ΔNH_4^+		ΔDIN		ΔPO_4^{3-}	
			r	*p*	*r*	*p*	*r*	*p*	*r*	*p*	*r*	*p*
Salinity	Surface	30	-0.50	**	-	n.s.	-	n.s.	-0.53	**	-0.66	***
	Middle	23	0.50	*	0.47	*	-	n.s.	0.55	**	0.56	**
	Bottom	30	-	n.s.	0.44	*	0.51	**	0.41	*	0.60	***
O_2	Surface	30	-	n.s.	-	n.s.	-	n.s.	-	n.s.	0.42	*
	Middle	23	-	n.s.	-0.50	*	-0.51	*	-0.44	*	-0.52	*
	Bottom	30	-0.39	*	-0.56	**	-0.64	***	-0.65	***	-0.71	***
Chlorophyll *a*	Surface	30	-0.42	*	-	n.s.	-	n.s.	-0.46	**	-0.72	***
	Middle	23	-	n.s.	-	n.s.	-	n.s.	-	n.s.	0.52	**
	Bottom	30	-	n.s.	-	n.s.	-	n.s.	-	n.s.	-	n.s.

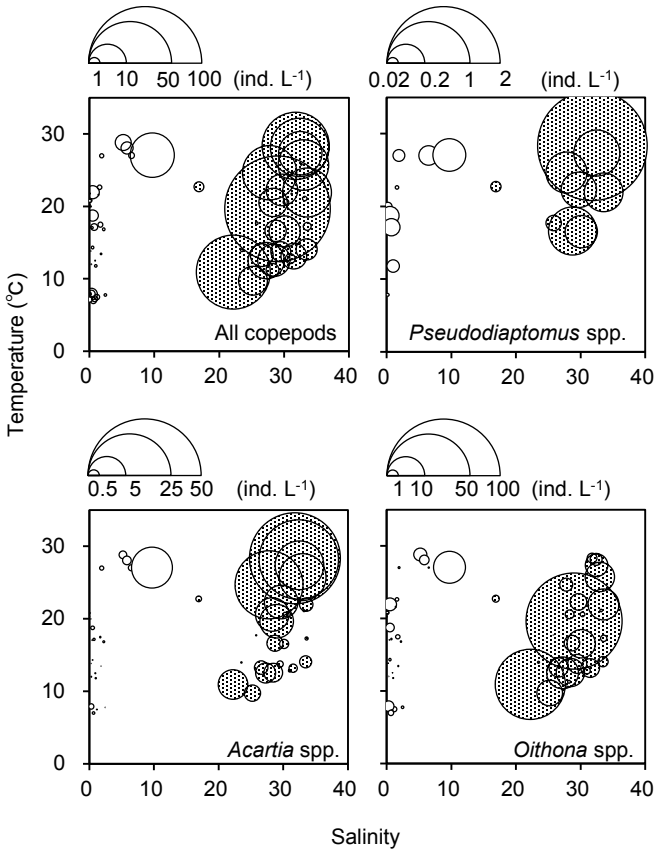

Fig. 2-8. Density of copepods in relation to salinity and temperature observed in the downstream portion of the Yura River (station Y1, Y2, and Y4) from January to November 2007. All copepods and dominant genera are shown. Open circle: surface layer. Shaded circle: bottom layer.

Discussion

Relationship between salt-wedge intrusion and phytoplankton succession

During the low river flow period (from early summer to autumn), phytoplankton blooms occur in the downstream portion of the Yura River. Kasai et al. (2010) proposed two hypotheses for the mechanism of the chlorophyll maximum formation. First, phytoplankton that increase in abundance at the surface at the river mouth may be transported upstream through the middle layer by estuarine circulation. Second, marine phytoplankton would bloom using riverine nutrients at the interface between the upper and lower layers. In this study, I found that two phytoplankton groups were present in blooms in the downstream portion of the river under a significant salt-wedge regime (summer). These two groups, freshwater and brackish species and marine species, were distributed separately along the salinity gradient.

Under the salt-wedge regime, phytoplankton cell density in the surface layer was high at the river mouth (Y1) and colonial cyanobacteria, Chlorophyceae, and brackish diatoms (*Cyclotella* spp.) were dominant (Fig. 2-5). Because Japanese rivers are generally steep and have short residence times, freshwater phytoplankton blooms rarely occur except in dammed lakes (Murakami et al., 1992). However, during low flow periods, increases in the residence time of water in rivers can cause riverine phytoplankton blooms (Murakami et al., 1994). In the Yura River, river discharge was low and residence time would be longer in summer. Additionally, the high sea level could make it hard for freshwater to flow out to the sea in summer. The increase in residence time would stimulate freshwater and brackish phytoplankton blooms in the downstream portion of the Yura River. Colonial cyanobacteria are tolerant of high light intensities (Costa et al., 2009) and prefer high temperature and eutrophic conditions (Gaulke et al., 2010). These conditions would encourage the growth of cyanobacteria in the surface layer in summer.

Marine diatoms (*Skeletonema* spp., *Thalassiosira* spp., and *Chaetoceros* spp.) dominated the chlorophyll maximum layer just below the halocline under the salt-wedge regime (Fig. 2-5). Marine diatom blooms with salt-wedge intrusions have also been reported in other estuaries (Twomey and John, 2001; González et al., 2007). In this study, the dominant phytoplankton groups below the halocline were different from those growing at the surface of the river mouth. Furthermore, marine phytoplankton populations increased as they were transported from the coastal water to upstream areas in the saline layer (Figs. 2-3 and 2-5). These observations support the second hypothesis proposed by Kasai et al. (2010) and showed that marine phytoplankton increased in situ below the halocline and created the chlorophyll maximum. The optimal salinity range for each diatom strain depends on the salinity of its original habitat (Balzano et al., 2011). Since marine diatoms that were found in the salt wedge might have originally been distributed in the coastal zone with higher salinity, they could only increase in abundance below the halocline. Moreover, the supply of nutrients from the freshwater and sufficient light conditions would stimulate the formation of a thin maximum layer just below the halocline (Durham and Stocker, 2012). Under a freshwater regime in the rainy season, the chl. *a* concentration was low (Fig. 2-2) and marine phytoplankton was absent. Even in summer, the high river discharge washed out phytoplankton from the river and reduced the phytoplankton production under this regime.

The residence time of water in the downstream portion of the river is not sufficient for phytoplankton growth due to high river discharge in winter and spring (Fig. 2-6). Marine phytoplankton could not stay in the area because of the high frequency of flushing with saline water. The downstream portion of the Yura River would play a minor role for phytoplankton production in the estuary during high-discharge seasons. In this study, I determined the phytoplankton composition only under two extreme conditions. In future studies, phytoplankton

succession needs to be investigated during the transition period between these regimes.

Linkages between nutrient dynamics and primary production with salt-wedge intrusion

NO_3^- and PO_4^{3-} concentrations were high in riverine freshwater and low in coastal water in the Yura River estuary (Figs. 2-3 and 2-4). This indicates that the main source of NO_3^- and PO_4^{3-} in salt-wedge estuaries is riverine inputs (Sierra et al., 2002; Haralambidou et al., 2010). NO_3^- and PO_4^{3-} were mainly consumed in low-salinity water (0–15; Fig. 2-7). Surface ΔNO_3^- and ΔPO_4^{3-} decreased with chl. *a* concentrations (Fig. 2-7c, o, Table 2-1). Therefore, the main factor affecting NO_3^- and PO_4^{3-} reduction in the low-salinity water would be freshwater and brackish phytoplankton blooms in the low flow period (summer).

In addition to consumption by phytoplankton, the dynamics of DIN and PO_4^{3-} in the salt-wedge water changed with reductions in O_2 (Figs. 2-3 and 2-7). Oxygen consumption during the aerobic decomposition of organic matter would affect the O_2 reduction in the salt wedge. Hypoxic events have been reported in various salt-wedge estuaries. Haralambidou et al. (2010) suggested that an increase in the residence time of saline water promotes sediment decomposition. Weston et al. (2010b) indicated that saltwater intrusions stimulate microbial decomposition and accelerate the mineralization of organic matter. Moreover, in the Ebro River estuary, terrestrial organic matter sedimented from the upper freshwater layer was mineralized in the lower saltwater layer (Sierra et al., 2002; Falco et al., 2010). In the downstream portion of the Yura River, the salt wedge stagnated for a long time in the bottom layer during low flow periods. Phytoplankton blooms would supply large amounts of organic matter to the bottom salt water. Therefore, the promotion of the mineralization by a salt-wedge intrusion would result in hypoxia in the saline layer.

NH_4^+ supplied from mineralization transforms into NO_3^- via NO_2^- by a nitrifier in a salt

wedge. NH_4^+, NO_2^-, and NO_3^- increased in the saline hypoxic layer, suggesting that the efflux of NH_4^+ with mineralization and nitrification occurred (Figs. 2-3 and 2-7). PO_4^{3-} was also released with the reduction in O_2 in the saline layer (Figs. 2-3 and 2-7). Mineralization promoted by the salt-wedge intrusion would be the key factor affecting the supply of DIN and PO_4^{3-}. The release of PO_4^{3-} from anoxic sediments is another known factor (House, 2003). PO_4^{3-} that is attached to terrestrial soil sediments that flow into the estuary is released into the water column with the increase in salinity (Fox et al., 1986; Inoue and Ebise, 1991). Therefore, the salt-wedge intrusion and subsequent hypoxia trigger the supply of PO_4^{3-} from the sediments and suspended solids into the saline layer.

ΔDIN (0–22 μM) and ΔPO_4^{3-} (–0.06 to 1.98) were varies under low O_2 conditions (O_2 < 150 μM), and the relationship between the nutrient increase and O_2 consumption did not balance (Fig. 2-7k and n). Less DIN and PO_4^{3-} were regenerated than predicted based on the Redfield ratio (Redfield, 1963) and the O_2 consumption. This imbalance may occur due to the consumption of regenerated DIN and PO_4^{3-} in salt water. Because sufficient light is available in the saline layer, DIN and PO_4^{3-} regenerated in the salt wedge would be used by marine phytoplankton in the saline water. This idea was supported by the study in the Krka Estuary (Legovic et al., 1994). Weston et al. (2010a) also suggested that salinity-mediated desorption and the flux of NH_4^+ from the sediment is a potentially important source of DIN for primary producers in low flow periods in a salt-wedge estuary. The amplification of marine diatom blooms would be driven not only by riverine nutrients but also by regenerated nutrients in the salt wedge.

The DIN/PO_4^{3-} ratio ranged from 4.9 to 171.2 mol mol^{-1} (mean ± standard error = 58.0 ± 5.0 mol mol^{-1}) at the river stations. The DIN/PO_4^{3-} ratio was mostly higher than the Redfield ratio (N/P = 16; Redfield, 1963), indicating that phosphorus was the potentially limiting nutrient

in the downstream portion of the Yura River. Dissolved silicate (DSi) is another important nutrient for diatoms. In our subsequent surveys from 2010 to 2011, the DSi/DIN ratio was higher (6.8 ± 0.8 mol mol^{-1}; Watanabe et al., 2017) than the Redfield ratio (Si/N = 1; Redfield, 1963), suggesting that the DSi concentration would be sufficient for the growth of diatoms in the downstream portion of the Yura River.

Trophic ecological processes in a seasonal salt-wedge estuary

Copepods increased synchronously with seasonal salt-wedge intrusions and the dominant genus was abundant in the saline layer (Figs. 2-2 and 2-8). Copepods were abundant during May–September when phytoplankton blooms occurred, with the exception of during the rainy season. The dominant genera, *Oithona* spp., *Acartia* spp., and *Pseudodiaptomus* spp., are often observed in estuaries and bays in Japan (Hirota and Hara, 1975; Ueda, 1991; Kawabata and Defaye, 1994; Uye et al., 2000). Copepods transported by the salt-wedge intrusion would increase in the downstream portion of the Yura River, feeding on the plentiful phytoplankton under the salt-wedge regime (summer). In highly mixed estuaries, copepods are often abundant in turbidity maximum zones where they use accumulated organic matter, mainly phytoplankton and detritus (Suzuki et al., 2008; Botto et al., 2011). In salt-wedge estuaries, copepods increase using organic matter that is accumulated at the halocline (Vidjak et al., 2009). In the Yura River, copepods would assemble in the chlorophyll maximum layer and feed on the abundant phytoplankton. However, from June to July, seasonal floods flush copepods out of the river, and they can only replace their biomass after the recovery of stratification and phytoplankton production in the river (Ueda et al., 2004). Considering the frequency of floods in the Yura River, the washout and recovery of the copepod community would be repeated frequently and rapidly.

Antonio et al. (2010a, 2010b, 2012) investigated the spatial and temporal structure of the benthic community in the Yura River estuary and examined their food sources using stable isotopes. They showed that organic matter derived from marine phytoplankton was used by estuarine benthos in the river from spring to summer (Antonio et al., 2012). Marine phytoplankton increasing in the salt wedge would contribute largely to benthic production during spring to summer.

Recent studies have shown that salt-wedge estuaries play important roles as nursery grounds for fish larvae. Salt-wedge intrusion is important for the successful reproduction and survival of black bream *Acanthopagrus butcheri*, white perch *Morone americana*, and striped bass *Morone saxatilis* (North and Houde, 2001, 2006; Jenkins et al., 2010; Williams et al., 2012). Zooplankton abundance was found to increase by using detritus that assembled at the tip of the salt wedge, which provided an environment with plentiful food for fish larvae (North and Houde, 2003; Shoji et al., 2005).

The abundant phytoplankton under the salt-wedge regime could also serve as the base of the food web in the downstream portion of the Yura River. Juvenile temperate seabass *Lateolabrax japonicus* migrate into the river with seawater intrusions and grow well using mysids and copepods in spring and early summer (Fuji et al., 2010, 2011). Furthermore, the abundant copepods support the production of gobies in warm seasons (Aoki et al., 2014). The abundant phytoplankton under the salt-wedge regime would enhance populations of zooplankton and fish, and augment benthic production in the downstream portion of the river during spring and summer.

The residence time of riverine nutrients becomes longer because nutrients are reused in the salt wedge from spring to summer. This mechanism may reduce the nutrient inputs into the Tango Bay coastal zone, which would weaken phytoplankton and zooplankton production there

(Figs. 2-2 and 2-3).

In contrast, during winter to early spring, high river discharge supplies almost all of the nutrients directly into the coastal zone, enhancing primary production in Tango Bay (Figs. 2-2 and 2-4). Some important commercial fishes in this area, such as seabass and flounder, spend their larval period and consume zooplankton in the shallow coastal zone of Tango Bay from winter to spring when zooplankton production is high (Minami, 1982; Fuji et al., 2010; Islam et al., 2010). After this period, juveniles leave the pelagic water column; flounder settle on the shallow bottom (Minami, 1982) and sea bass move to the river or bottom ecosystem in the coastal zone (Fuji et al., 2010), where mysids are abundant in spring and summer (Fuji et al., 2010, 2011). This indicates that these fishes efficiently use the biological production system that changes spatially and temporally in the study area. As I showed in this study, seasonal changes in river discharge and the dynamics of salt-wedge intrusions greatly affect biological production in this shallow coastal ecosystem.

Chapter 3:

Estuarine circulation-driven entrainment of oceanic nutrients fuels coastal phytoplankton in an open coastal system in Japan

Introduction

The global distributions of fishery resources correspond to the distributions of phytoplankton biomass, indicating that phytoplankton production supports fishery production in marine ecosystems (Caddy and Bakun, 1994) through a bottom-up effect (Kimmerer, 2002; Connolly et al., 2009; Kostecki et al., 2010). Because phytoplankton primary production is primarily limited by nutrient and light availability, variations in these factors regulate seasonal and annual fluctuations in phytoplankton primary production (Cloern and Jassby, 2008). The timing of phytoplankton blooms then regulates the timing of increases in secondary production, which affects larval fish survival and annual fish stock recruitment (Cloern and Jassby, 2008).

In estuarine and coastal systems without strong tidal mixing, freshwater flow and upwelling are the major processes supplying nutrients (Caddy and Bakun, 1994). In addition to directly transporting terrestrial nutrients, freshwater inflows also drive estuarine circulation, indirectly regulating the entrainment of oceanic nutrients from the offshore to coastal zones (Smith and Demaster, 1996). Seasonal and interannual variations in freshwater flow can strongly influence variability in coastal phytoplankton production (Cloern, 1996). Previous studies in semi-enclosed coastal systems have suggested that riverine nutrient inputs directly stimulate primary production (Paerl et al., 1990; Scharler and Baird, 2005), and that nutrient loadings that accompany seasonal floods drive phytoplankton blooms (Malone et al., 1988; Mallin et al., 1993; Sugimoto et al., 2004; Murrell et al., 2007). Moreover, the entrainment of recycled nutrients driven by estuarine circulation influences the timing and magnitude of

phytoplankton blooms in semi-enclosed systems (Malone et al., 1988; Sugimoto et al., 2010). Thus, riverine nutrient inputs and the entrainment of oceanic nutrients, which are both driven by freshwater flows, simultaneously regulate phytoplankton primary production (Tseng et al., 2014). However, the contribution of each nutrient source to phytoplankton production in open coastal systems influenced by oceanic water is largely unknown. Changes in the contribution from the fluxes could have complex effects on coastal phytoplankton production because the nutrient concentrations, composition, and volume of these two inputs can vary seasonally.

Tango Bay is an open bay in Japan that receives most of its riverine nutrient inputs from the Yura River (Fig. 3-1). Although the coastal zone of Tango Bay is relatively oligotrophic (Kasai et al., 2010; Watanabe et al., 2014), it provides important nursery grounds for many fish (Takeno et al., 2008; Islam et al., 2010). Although our previous study demonstrated that high river discharge enhanced primary production in Tango Bay (Watanabe et al., 2014), the mechanisms have not been examined quantitatively. Here I examined how freshwater flow affects phytoplankton dynamics in Tango Bay. First, I investigated the spatiotemporal distributions of physical parameters, nutrient concentrations, euphotic zone depth, and phytoplankton biomass (chlorophyll *a*). I then determined which nutrients [nitrogen (N), phosphorus (P), silica (Si) and iron (Fe)] limited phytoplankton growth using bioassays and stoichiometry. I also calculated riverine nutrient fluxes and the oceanic nutrients entrained by estuarine circulation. Finally, I compared seasonal fluctuations in phytoplankton biomass with nutrient fluxes and light availability to evaluate linkages between freshwater flow and coastal phytoplankton in this open bay.

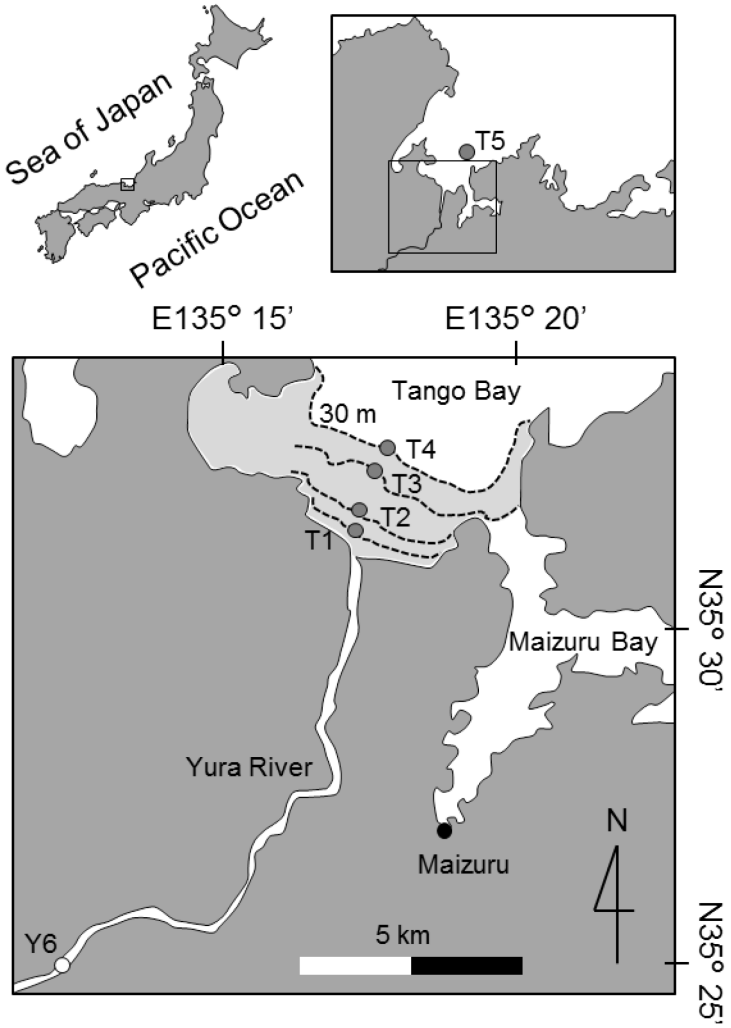

Fig. 3-1. Location of Tango Bay and the Yura River. Gray circles indicate coastal stations and the open circle is the river station. Distance from the river mouth to each coastal station: T1, 0.95 km; T2, 1.35 km; T3, 2.40 km; T4, 3.70 km; T5, 10.0 km. The shaded area depicts the coastal boxes used to calculate the entrained water flux driven by estuarine circulation. The closed circle marks the site where daily mean global solar radiation was monitored by the Japan Meteorological Agency in Maizuru.

Materials and methods

Study area

The Yura River has a total length of 146 km and a total catchment area of 1,880 km^2 (Fig. 3-1). Flow in the Yura River is variable (coefficient of variation [CV] = 1.27), with an annual variation that exceeds the world average (CV = 0.40; Finlayson and McMahon, 1988). Seasonal peaks in flow typically follow spring snowmelt and periods of high precipitation between May and July. Between August and December, precipitation is generally low. Tango Bay is a microtidal estuary with a spring tidal range of less than 0.5 m (Kasai et al., 2010). With an embayment degree of 0.9 (ED = the distance between the mouth and head of a bay/the width of the mouth), Tango Bay is more open than semi-enclosed bays in Japan (Hiroshima Bay: 2.6; Ise Bay: 3.6) and elsewhere (Chesapeake Bay: 16.3; San Francisco Bay: 19.5); accordingly, it is classified as an open bay.

Field surveys and sample analyses

Field surveys were conducted in the coastal zone of Tango Bay and in the downstream Yura River. Surveys in the coastal zone were conducted approximately every 10 days between December 2009 and July 2011 at four sampling stations with varying depths: T1, 5 m; T2, 10 m; T3, 20 m; T4, 30 m (Fig. 3-1). Additionally, three surveys were conducted at station T5 (depth: 50m) on 8 February, 22 March, and 26 April 2011 to assess the conditions of the deep zone in Tango Bay. To estimate riverine nutrient fluxes, surveys were conducted between May 2010 and July 2011 (n = 12) at station Y6, which was 16 km upstream from the river mouth and was not influenced by seawater intrusion (Fig. 3-1 and Table 3-1). All surveys were conducted in the daytime and vertical profiles (every 0.1 m) of salinity, water temperature, chlorophyll fluorescence, and turbidity were measured at each station using a conductivity, temperature, and

depth profiler (CTD; Compact-CTD; Alec Electronics, Kobe, Japan). Water samples for chlorophyll *a* (chl. *a*) and nutrients were taken from the surface (depth: 0.2 m) and bottom (depth: 1.0 m above bottom) layers at each station in the coastal zone (T1–T5) and from the surface water at the river station (Y6). In addition, water samples for chl. *a* and nutrients were taken from the middle layers between February and June 2011 (depth: T1, 2 m; T2, 2 and 5 m; T3, 2, 5 and 10 m; T4, 2, 5 and 15 m; T5, 2, 5, 10, and 25 m). All water samples were filtered through GF/F glass fiber filters (Whatman PLC, Maidstone, Kent, UK) prior to determination of chl. *a* concentrations. The filters were then extracted in the dark in 90% acetone for 12 h, after which chl. *a* concentrations were measured (Strickland and Parsons, 1972) using a calibrated fluorometer (Trilogy; Turner Designs, Sunnyvale, CA, USA). The vertical profile of chlorophyll fluorescence recorded by the CTD profiler was calibrated with the measured chl. *a*. Chl. *a* concentrations every 0.1 m were averaged vertically to calculate chl. *a* concentrations for the entire water column. Water samples taken between March 2010 and July 2011 were used to determine nutrient concentrations [nitrate+nitrite (NO_x), phosphate (PO_4^{3-}), and dissolved silica (DSi)]. Water samples were filtered through a 0.45-μm mesh filter (Dismic filter; Advantec, Durham, NC, USA), after which nutrient concentrations were measured using a nutrient AutoAnalyzer (QuAAtro 2-HR; BL-Tec, Osaka, Japan) (Clesceri et al., 1998).

Potentially limiting nutrients were evaluated by comparing water nutrient ratios with elemental ratios in diatoms, which were the primary contributors to coastal phytoplankton production in Tango Bay during the study period. The elemental ratios in diatoms were estimated using the standard nutrient ratio (Redfield et al., 1963; Brzezinski, 1985) of N:P:Si = 16:1:16.

The daily mean global solar radiation (GSR) was obtained from the Japan Meteorological Agency based on measurements in Maizuru (Fig. 3-1). Daily mean river discharges (measured

Table 3-1. River discharge, temperature, and nutrient concentrations of the surface water at station Y6, 16 km upstream from the river mouth.

Survey	River discharge ($m^3\ s^{-1}$)	Temperature (°C)	NO_x (μM)	PO_4^{3-} (μM)	DSi (μM)
14 May 2010	34	15.2	44	1.0	131
11 Jun 2010	20	23.6	37	0.9	135
17 Jul 2010	143	22.3	38	0.9	181
13 Aug 2010	64	25.6	49	1.4	178
19 Aug 2010	22	29.6	53	1.6	188
18 Nov 2010	20	12.5	49	0.8	87
21 Jan 2011	44	4.8	47	0.6	128
19 Feb 2011	250	6.0	58	0.5	108
19 Mar 2011	95	7.4	40	0.6	166
25 Apr 2011	142	11.7	49	0.7	162
25 Jun 2011	52	24.8	39	0.9	136
26 Jul 2011	25	24.4	54	1.1	178

at Hami Bridge, 25 km upstream from the river mouth) and daily mean surface water temperatures (measured at Shimoamatsu, 31 km upstream from the river mouth) in the Yura River were obtained from the Ministry of Land, Infrastructure, Transport and Tourism and from the Meteorological Agency, respectively.

Bioassays

Bioassays were conducted on four sampling dates to determine the nutrients that potentially limited natural coastal phytoplankton assemblages. Water samples were taken from the chlorophyll maximum layer at station T4 on 23 February (depth: 10 m), 15 March (6 m), 9 May (17 m), and 23 June 2011 (20 m) using an iron-free Van Dorn water sampler. Water samples were collected in surface contamination clean (SCC) bottles (AS ONE, Osaka, Japan). Each sample (100 mL) was gently filtered through a 100-μm mesh net into a new SCC bottle (AS ONE).

To prevent iron contamination, all equipment and containers were immersed in 4 M HCl for at least 24 h and thoroughly rinsed with pure water (Milli-Q Water; Millipore, Billerica, MA, USA). In addition, micropipette tips and bottles of stock solutions were washed in boiling 1 M nitric acid, hydrochloric acid, and Milli-Q water in that order. The following nutrients were added to the bottles individually and in all combinations: +N (nitrate: 200 μM final concentration), +P (phosphate: 10 μM), +Si [silicate: 33 μM] and +Fe (EDTA-chelated Fe: 0.2 μM). Although these concentrations are much higher than natural concentrations, they would not alter evaluation of the limiting nutrient. Controls were established by adding the same amount (1 mL) of pure water (Milli-Q water; Millipore). Three subsamples were dispensed into 10 mL acid-washed polystyrene tubes by acid-washed micropipettes in a clean air bench, which were incubated under a 14:10 light–dark cycle (100–120 μmol photons m^{-2} s^{-1}) at 15°C. The

tubes were shaken once a day. The tubes were then analyzed for in vivo chlorophyll fluorescence (10-AU 005; Turner Designs) every few days over a 7–10-day time course, during which time the chlorophyll fluorescence of all subsamples became saturated. Although a bottle effect could bias the results of this long-term experiment (Hammes et al., 2010), such effects would not alter evaluation of the limiting nutrient. The rate of phytoplankton growth was calculated as the increase in fluorescence per day. Significant differences among treatment means were identified by one-way analysis of variance (ANOVA) followed by Tukey's honestly significant difference (HSD) test at $p < 0.05$ using R 3.3.1 (R Core Team, 2017).

Estimation of riverine nutrient fluxes

Nutrient concentrations used for the estimation were obtained from 12 samplings of the surface water at station Y6 (Fig. 3-1; Kasai et al., 2010). NO_x concentrations did not exhibit seasonal changes and were not significantly correlated with either water temperature or daily river discharge (Table 3-1; Spearman's rank correlation: $p > 0.05$); therefore, the NO_x flux was calculated from the annual average concentration. In contrast, because of the significant linear relationship between PO_4^{3-} and DSi and water temperature (Table 3-1; Spearman's rank correlation: $r_s = 0.90$, $p < 0.01$ and $r_s = 0.65$, $p < 0.05$, respectively) the daily concentrations of PO_4^{3-} and DSi were calculated with linear models as follows:

$$C_P(T) = 0.0319 \times T + 0.381,$$

$$C_{Si}(T) = 2.07 \times T + 112,$$

where T, $C_P(T)$, and $C_{Si}(T)$ indicate the daily mean temperature and the concentrations (μM) of PO_4^{3-} and DSi, respectively. The nutrient flux equations were as follows:

$$NO_x \text{ flux} = C_N \times Q_f, \quad (R^2 = 0.96, n = 12),$$

$$PO_4^{3-} \text{ flux} = C_P(T) \times Q_f, \quad (R^2 = 0.97, n = 12),$$

DSi flux = $C_{Si}(T) \times Q_f$, ($R^2 = 0.94$, $n = 12$),

where Q_f is the daily river discharge and C_N is the annual average concentration of NO_x at station Y6 (46 μM). Values of R^2 above 0.94 indicate that the models account for more than 94% of the fluctuations in the flux as measured in 12 surveys. However, during periods when the river discharge is higher than 250 m^3 s^{-1} there would be model uncertainty associated with estimations of the nutrient fluxes.

Estimation of the entrainment fluxes of nutrients using a box model

In this study, entrainment was defined as the transports of water and nutrients driven only by estuarine circulation. The flux of entrainment water was estimated using a box model (a salinity conservative model) that determined the entrained fluxes of nutrients from the offshore into the coastal zone. The coastal box was defined as the area shallower than 30 m, excluding Maizuru Bay (Fig. 3-1). The offshore box was defined as the zone deeper than 30 m. The halocline, which occurs at levels shallower than 5 m throughout most of the year, defined the coastal zone boxes as the surface layer above 5 m (box-1) and the deeper layer (box-2). The salinity conservative model was defined as:

$$V_1 \frac{dS_1}{dt} = Q\overline{S_2} - (Q + Q_f)\overline{S_1},$$

where Q, Q_f, and V_1 (1.35×10^8 m^3) represent the monthly flux of entrained water, the monthly freshwater flux (river discharge), and the volume of box-1, respectively; S_1 and S_2 are the spatial and vertical mean salinities of box 1 and box 2, and $\overline{S_1}$ and $\overline{S_2}$ are the monthly averages of S_1 and S_2, respectively. The flux of entrained water (Q) was estimated over monthly time steps.

Monthly nutrient fluxes driven by estuarine circulation were calculated by multiplying Q by the monthly mean nutrient concentrations in the bottom water at station T4. This model did not evaluate the impact of nutrient input from Maizuru Bay.

Estimation of the euphotic zone depth

The depth of the euphotic zone was estimated from turbidity data collected in the Tango Bay coastal zone. First, I calculated the actual extinction coefficients (k, m^{-1}) using vertical profiles of the photosynthetic photon flux density (PPFD), measured by a PPFD meter (MDS MkV-L; Alec Electronics, Kobe, Japan). The PPFD was measured 13 times between December 2009 and September 2010 at stations T1–T4. Actual k values were calculated for both the surface layer (0–1 m) and the lower layer (>1 m) on 22 December 2009 and 1 March 2010 when high turbidity river plumes were observed. Actual k values were calculated for the whole water column on the other dates. To estimate the k value from turbidity, I modeled the data using a generalized linear model (GLM) with an identity link. A GLM allows the error distribution to be specified. I used a gamma distribution because the k values were strictly non-negative. The GLM equation was as follows (Appendix Fig. S3-1, Table S3-1):

$$k = 0.1084 \times \text{Turbidity} + 0.1619.$$

The k value was calculated for both the surface layer (k_S; 0–1 m) and the lower layer (k_L; >1 m) on each sampling day. The euphotic zone depth (D_E, m) and the difference between the water depth (D, m) and D_E (ΔD_E) were calculated as follows:

$$D_E = -(\ln(0.01) + k_S - k_L) / k_L,$$

$$\Delta D_E = D - D_E.$$

The pseudo R^2 for the GLM was 0.88, calculated following the method outlined by McFadden (1973). The statistical analyses were conducted with R 3.3.1 (R Core Team, 2017).

Statistical analysis

I used a GLM with a gamma distribution and identity link to examine the effect of the

riverine nutrient flux, nutrient flux driven by estuarine circulation, and D_E on the seasonal fluctuations in chl. *a* as follows:

$$\overline{chl} = \overline{N_R} + \overline{N_O} + \overline{D_E} \text{ (full model)},$$

where $\overline{chl}$, $\overline{N_R}$, $\overline{N_O}$, and $\overline{D_E}$ indicate the monthly mean values of the water column chl. *a* concentration, riverine NO_x flux, NO_x flux driven by estuarine circulation, and D_E, respectively. I selected the best model using downward stepwise model selection according to the Akaike Information Criterion (AIC; Akaike 1974). The statistical analyses were conducted with R 3.3.1 (R Core Team, 2017).

Results

Temporal change in biogeochemical parameters

Sea surface temperature peaked (29.5°C) in August 2010, when water in Tango Bay was stratified (Fig. 3-2a), then declined to ~10°C in February and March, when the water column was vertically mixed. Horizontally-averaged surface salinity ranged from 12.7 to 33.8, and decreased between February and April 2010, June and July 2010, September and October 2010, and February and April 2011 (Fig. 3-2b). Seasonal changes in bottom salinity were small, varying between 32.5 in summer and ~34 from March to June. Surface nutrient concentrations were high during periods of low salinity (March–April, June–July and September–October 2010 and February–April 2011; Fig. 3-2c–e). At salinities <30, NO_x, PO_4^{3-} and DSi concentrations were often above 5, 0.2 and 20 μM, respectively. Bottom nutrient concentrations were relatively high from December to February (Fig. 3-2c–e), with maximum NO_x, PO_4^{3-} and DSi concentrations reaching more than 3, 0.3 and 10 μM, respectively. Surface chl. *a* concentrations were relatively high between August and September (Fig. 3-2f), whereas bottom chl. *a* concentrations were relatively high between February and April in both 2010 and 2011. Column

chl. *a* concentrations were consistent with those in the bottom, and highest (>3 μg L^{-1}) between February and April in both 2010 and 2011 (Fig. 3-2g) and relatively low (~3 μg L^{-1}) between May and January, except November 2010.

There were temporal fluctuations in turbidity (Fig. 3-3a–d) with a maximum value of more than 50 FTU at the surface of station T1 (Fig. 3-3a). Turbidity was higher at the shallower stations (e.g., stations T1 and T2). The value of ΔD_E was generally lower than 0 m at stations T1 and T2 (Fig. 3-3e, f), and was higher than 0 m on 13 April 2010, when the surface turbidity increased drastically because of river runoff; however, ΔD_E was generally controlled by the turbidity of the lower layer and increased close to 0 m from November to January (Fig. 3-3e, f). Values of ΔD_E ranged from −5.7 to 11.1 m and increased from November to January at station T3 (Fig. 3-3g). The value of ΔD_E remained higher than 0 m through the year at station T4 and only fluctuated slightly (Fig. 3-3h).

The chlorophyll maximum occurred at a depth of ~10 m between February and April in 2010 and 2011, although chl. *a* concentrations were higher in 2011 than in 2010 (Fig. 3-4a, b). The vertical and temporal distributions of both temperature and salinity were similar between in 2010 and 2011 (Fig. 3-4c–f). Surface NO_x concentrations were highest with low salinity when river runoffs occurred (Fig. 4g, h). NO_x concentrations in the middle and bottom layers were high in January and February, but decreased from March to April (Fig. 3-4g, h). The first peak in the chl. *a* concentrations coincided with the increase in GSR in late March 2010 and early February 2011 (Fig. 3-4i, j). Values of ΔD_E decreased from December to March in both 2010 and 2011 (Fig. 3-4k, l) but increased to more than 0 m in late March 2010 (Fig. 3-4k).

The chlorophyll maximum was distributed in the shallow zone (~30 m) of Tango Bay between February and April in 2011 (Fig. 3-5a–c). Chl. *a* concentrations were high at depths of 5–20 m. Salinity was low in surface waters (Fig. 3-5d–f). NO_x concentrations were generally

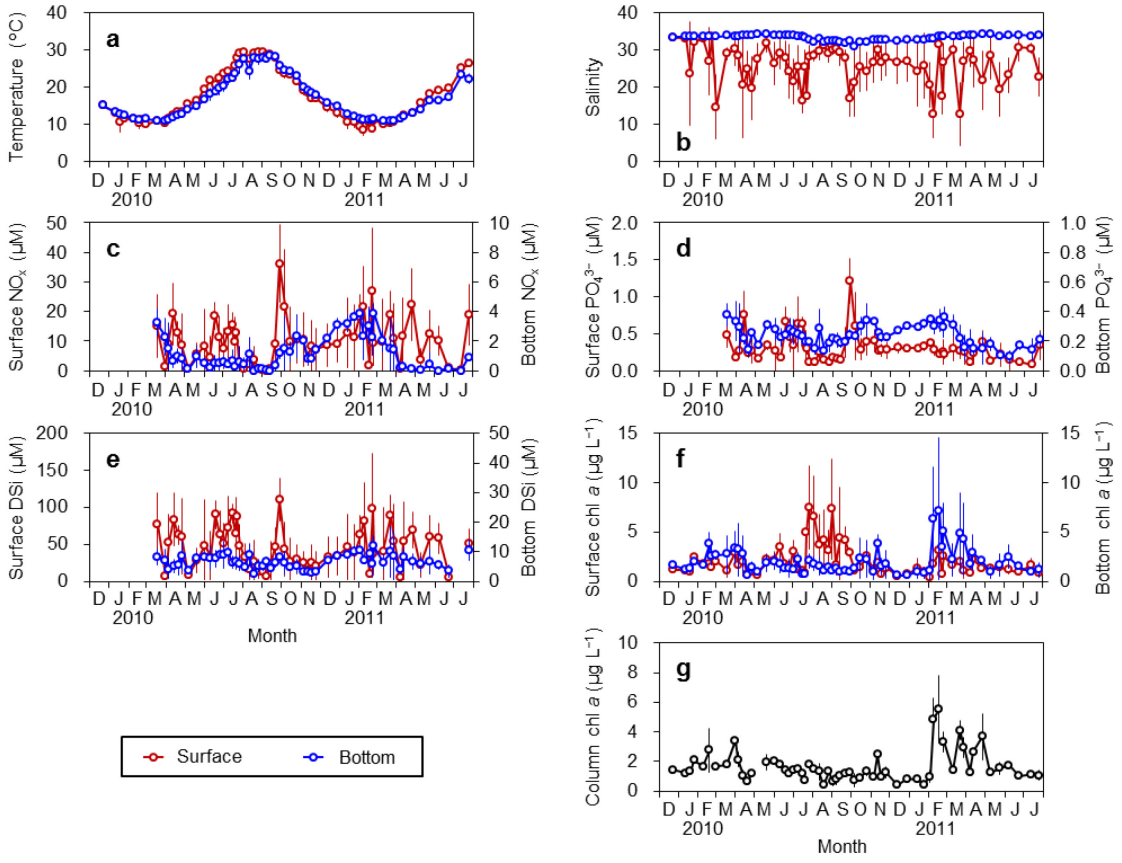

Fig. 3-2. Temporal changes in mean (**a**) temperature (°C), (**b**) salinity, (**c**) NO_x (μM), (**d**) PO_4^{3-} (μM), (**e**) DSi (μM), (**f**) chl *a* (μg L^{-1}) and (**g**) column chl *a* concentration (μg L^{-1}) of stations T1–T4 in Tango Bay. Red and blue circles indicate means of surface and bottom waters, respectively. The scales for the surface and bottom nutrient concentrations are different. Column chl *a* concentrations are water column means. Error bars indicate ±standard deviations of the mean values (n=4).

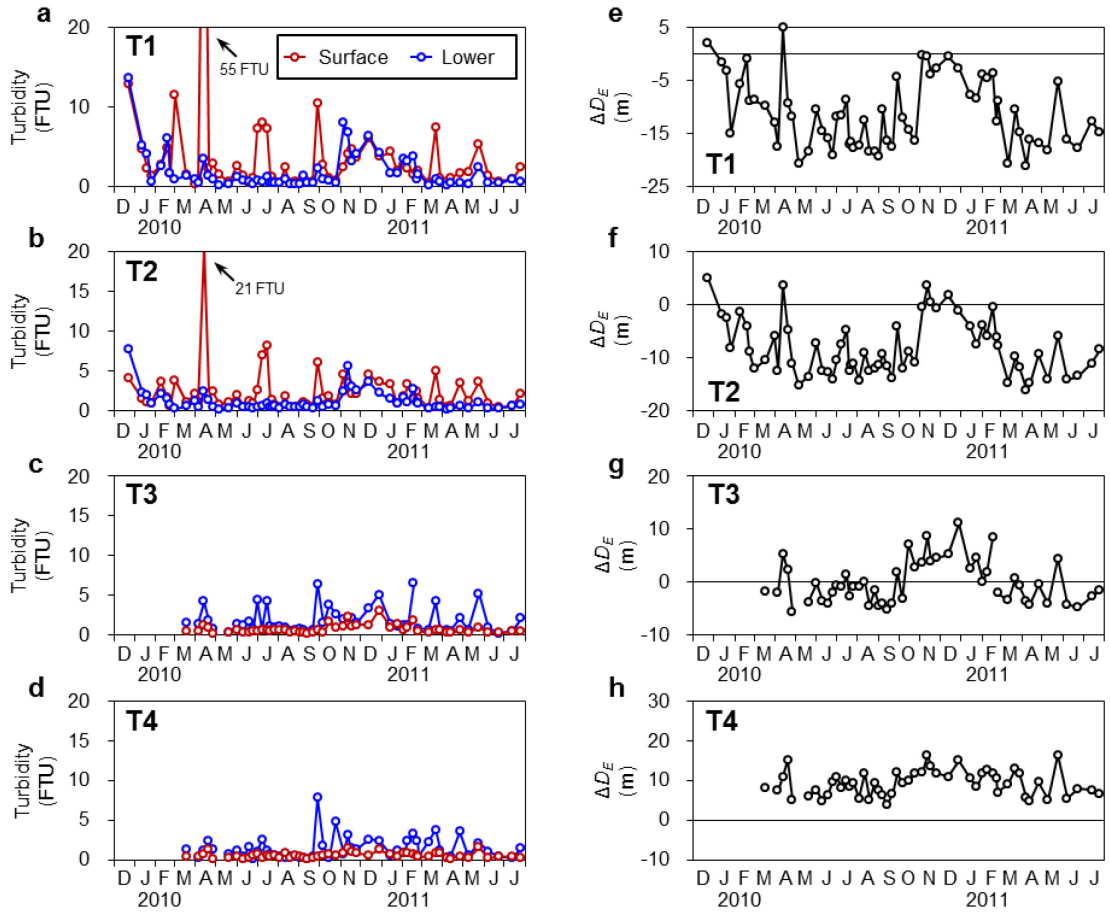

Fig. 3-3. Temporal changes in turbidity (FTU) at stations (**a**) T1, (**b**) T2, (**c**) T3 and (**d**) T4, and in ΔD_E (m) at stations (**e**) T1, (**f**) T2, (**g**) T3 and (**h**) T4. Red and blue circles indicate the surface (0–1 m) and lower layers (>1 m), respectively. ΔD_E is the difference between the water depth and the euphotic water depth, which was estimated with a generalized linear model using turbidity data.

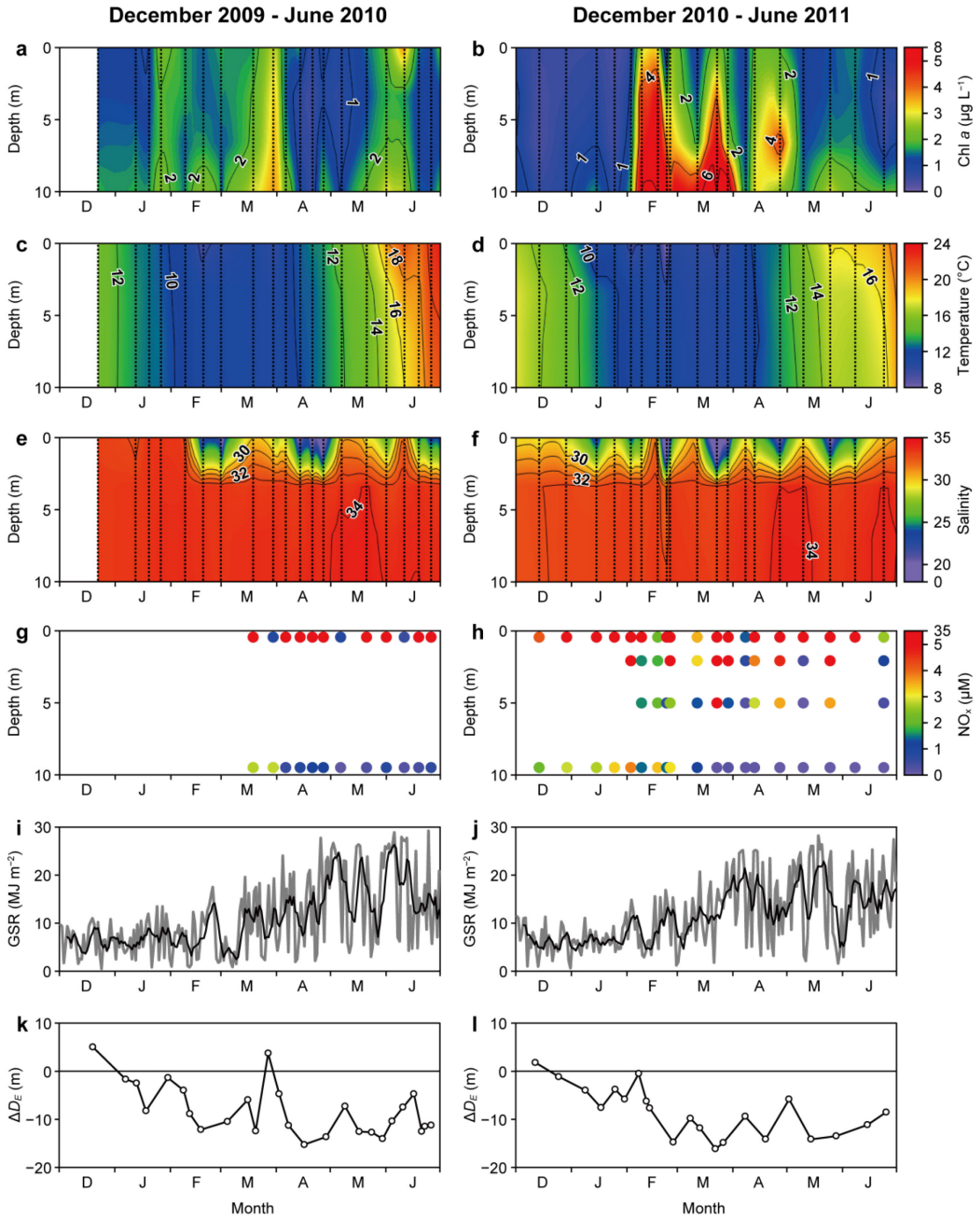

Fig. 3-4. Temporal variability (December–June 2010 and 2011) in (**a**, **b**) the vertical distribution of chl *a* concentration, (**c**, **d**) the vertical distribution of temperature, (**e**, **f**) the vertical distribution of salinity, (**g**, **h**) NO_x concentration (μM), (**i**, **j**) global solar radiation (GSR), and (**k**, **l**) ΔD_E in Tango Bay. The parameters in (**a**–**h**, **k**, **l**) were measured at station T2. The solid gray and black line in (**i**, **j**) are the daily values and the 5-day moving averages of GSR, respectively. ΔD_E is the difference between the water depth and the euphotic water depth, which was estimated from the turbidity data by a generalized linear model.

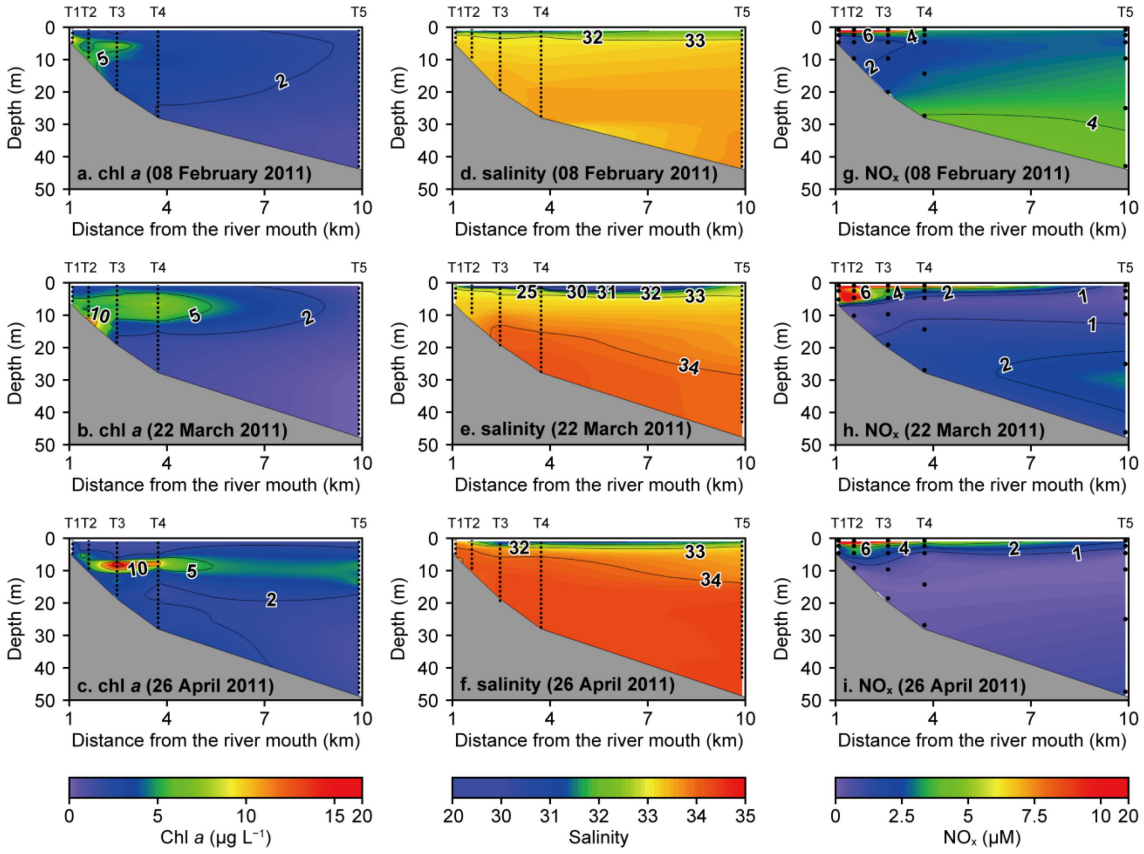

Fig. 3-5. Spatial distributions of (**a**–**c**) chl *a* concentration, (**d**–**f**) salinity, and (**g**–**i**) NO_x concentration on 8 February, 22 March, and 26 April 2011. Closed circles in (**g**–**i**) show each sampling depth for NO_x concentrations.

high in surface waters (Fig. 3-5g–i). Bottom NO_x concentration was relatively high in February 2011 and decreased in March and April 2011.

Coastal water nutrient ratios

Coastal water nutrient ratios (log-scale) are compared with the Redfield ratio in Fig. 3-6. In this study, N was defined as NO_x, P was defined as PO_4^{3-}, and Si was defined as DSi. The lines showing the Redfield ratio (N:P:Si = 16:1:16) delimited three areas, each characterized by potentially limiting nutrients. N/Si ratios were lower than 1 throughout the year in both surface and bottom waters (Fig. 3-6), indicating Si was not the limiting factor. N/P ratios in bottom water were lower than 16 throughout the year, but were often higher than 16 in surface water. N/P ratios were higher than 1 throughout the water column during the pre-blooming period (November–January) (Fig. 3-6a), but were often lower than 1 between February and July in bottom water (Fig. 3-6b, c) and between August and October in surface water (Fig. 3-6d).

Bioassay experiments

The rate of phytoplankton growth was significantly higher in the +P treatment than in the other groups in February, indicating that P was a potentially limiting nutrient (Fig. 3-7a–c). N was potentially limiting in March and May (Fig. 3-7d–i). In June, both N and P caused growth rates to increase significantly, indicating that both were potentially limiting nutrients (Fig. 3-7j, k).

Nutrient fluxes into the coastal zone

The median river discharge was 48 m^3 s^{-1} during the study period (Fig. 3-8a). River discharge was high from February to April because of melting snow. Additionally, sudden floods occurred between May and July, with the highest discharge recorded following two typhoons in

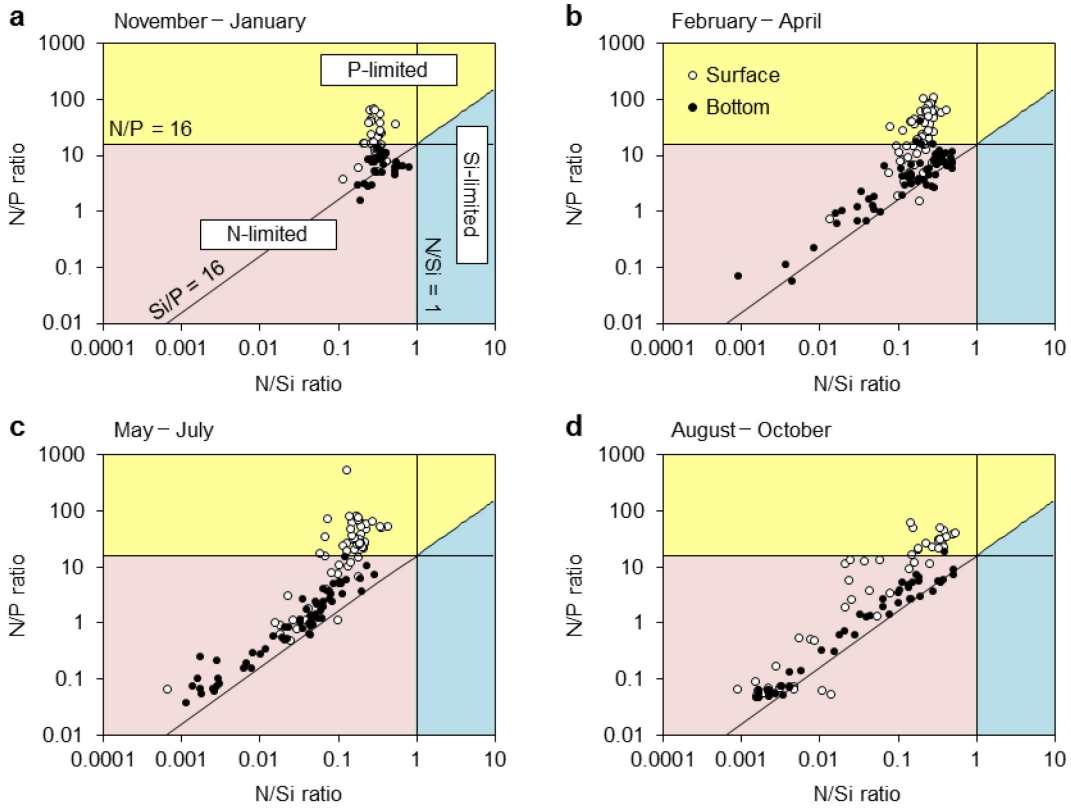

Fig. 3-6. N:P:Si molar ratios (log N/Si ratio vs. log N/P ratio) in the coastal waters of Tango Bay (**a**) from November to January, (**b**) from February to April, (**c**) from May to July, and (**d**) from August to October in 2010 and 2011. N, P and Si indicate NO_x, PO_4^{3-} and DSi, respectively. The potentially limiting nutrients in the three areas delimited by the Redfield ratio (N:P:Si = 16:1:16) are different. Open and closed circles indicate nutrient ratios in the surface and bottom water, respectively.

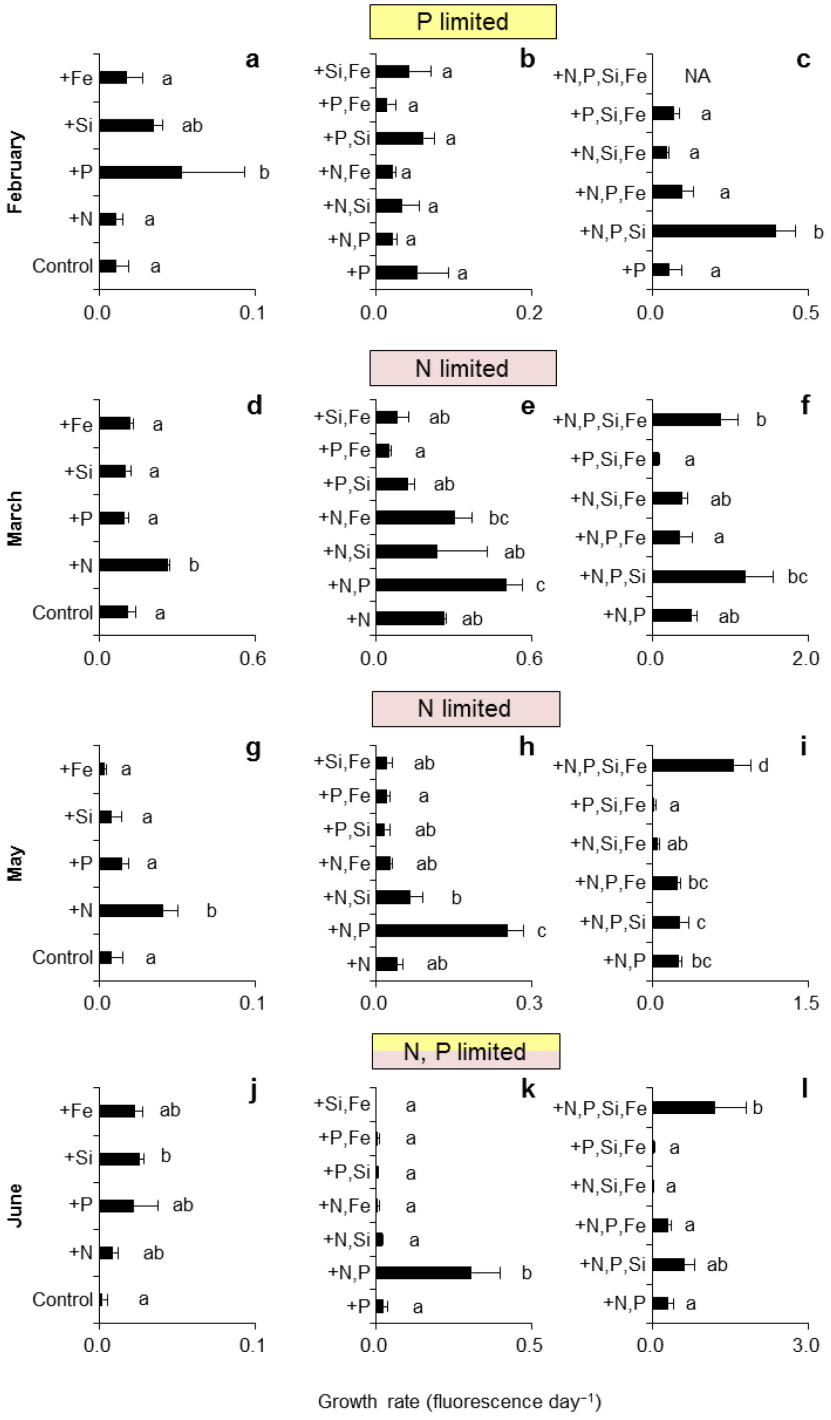

Fig. 3-7. Effects of nutrient addition (N, P, Si, and Fe individually and all combinations) on the rate of phytoplankton growth at station T4 in (**a**–**c**) February, (**d**–**f**) March, (**g**–**i**) May and (**j**–**l**) June 2011. For each month, the potentially limiting nutrients are shown. Error bars indicate ±standard deviations of the mean values (n=3). Mean growth rates among treatments (for each graph) were compared by one-way ANOVA followed by Tukey's HSD multiple comparison test. Significant differences ($p<0.05$) are indicated by different lowercase letters. NA: not analyzed.

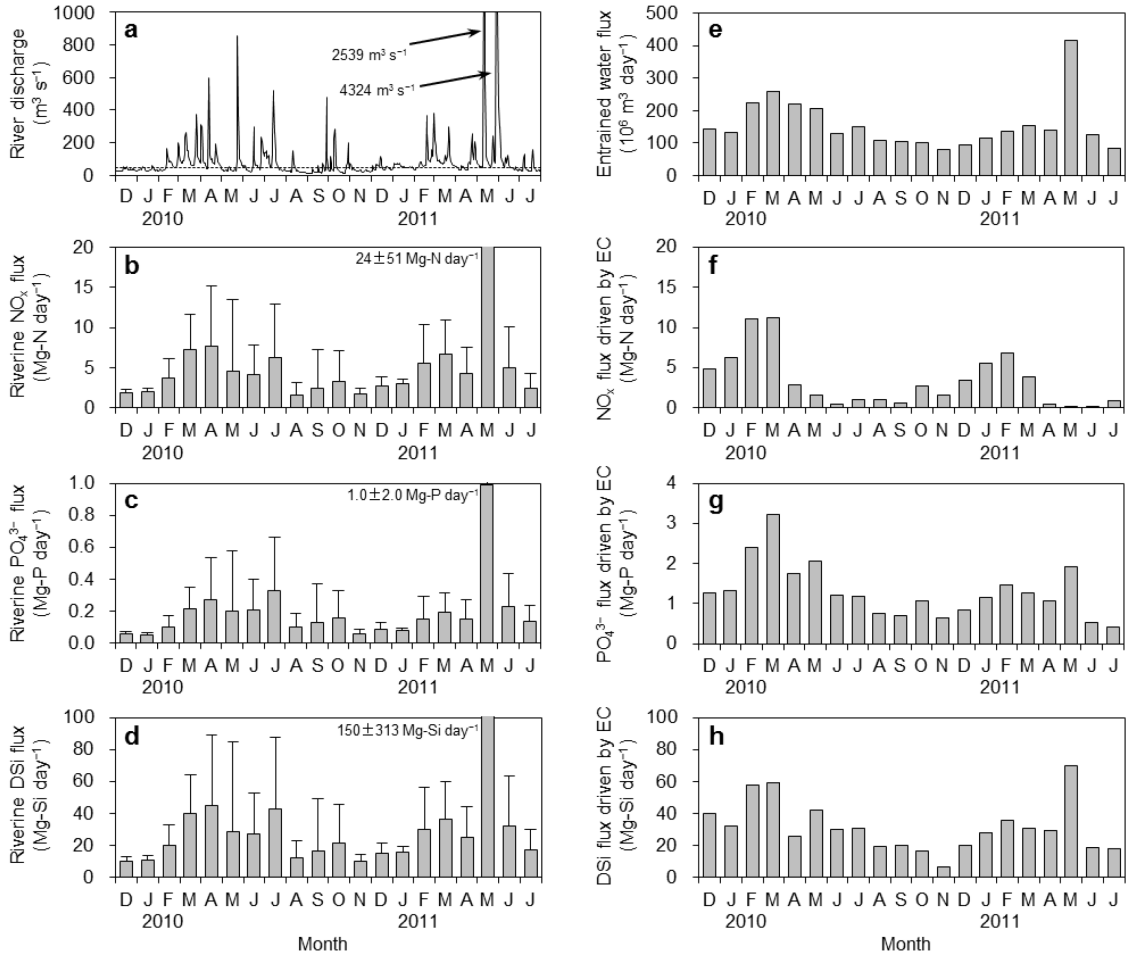

Fig. 3-8. Seasonal variation in (**a**) daily mean river discharge (m^3 s^{-1}), in monthly mean riverine flux of (**b**) NO_x (Mg [mega gram]-N day^{-1}), (**c**) PO_4^{3-} (Mg-P day^{-1}), and (**d**) DSi (Mg-Si day^{-1}), in the (**e**) entrained water flux (10^6 m^3 day^{-1}), (**f**) NO_x flux (Mg [mega gram]-N day^{-1}), (**g**) PO_4^{3-} flux (Mg-P day^{-1}), and (**h**) DSi flux (Mg-Si day^{-1}) driven by estuarine circulation (EC) in the Tango Bay shallow coastal zone. The riverine nutrient fluxes were estimated by the model from river discharge and temperature data. The entrained water flux was calculated with a box model. The nutrient fluxes driven by EC were estimated from the entrained water flux and the monthly mean nutrient concentrations in the bottom water at station T4. Error bars are standard deviations of the estimates. The dashed line in (**a**) shows the median river discharge over the entire study period.

May 2011. River discharge was generally low from summer to autumn, when there was little precipitation.

Following patterns of river discharge, NO_x, PO_4^{3-} and DSi fluxes from the Yura River into the coastal zone were high throughout February–April in both years (Fig. 3-8b–d) and remained high between May and July, with maximum values occurring in May 2011 (NO_x: 24.4 Mg [mega gram]-N day^{-1}; PO_4^{3-}: 0.99 Mg-P day^{-1}; DSi: 150.4 Mg-Si day^{-1}). Nutrient fluxes were low from August to January in 2010 (Fig. 3-8b–d).

The entrained water flux ranged from 81×10^6 to 416×10^6 m^3 day^{-1} (mean value: 157×10^6 m^3 day^{-1}), and the maximum estimated flux occurred in May 2011, when there were large floods (Fig. 3-8e). The entrained water flux was high from February to July, low from August to January and was significantly related to the volume of river discharge (Pearson's correlation coefficient: $r = 0.89$, $p < 0.001$; regression slope = 9.1). The ratio was comparable with previous estimates reported in coastal bays of Japan (Ise Bay: Q/Q_f = 2.5–30, Fujiwara et al., 1996; Hiroshima Bay: mean Q/Q_f = 7, Yamamoto et al., 2000).

The entrained flux of NO_x driven by estuarine circulation was higher from December to April (mean ± SD = 5.3 ± 3.5 Mg-N day^{-1}) than from May to October (1.0 ± 0.8 Mg-N day^{-1}) (Fig. 3-8f). The entrained fluxes of PO_4^{3-} and DSi were also higher from December to April (1.5 ± 0.7 Mg-P day^{-1}, 33.1 ± 15.2 Mg-Si day^{-1}) than from May to October (1.1 ± 0.6 Mg-P day^{-1}, 29.3 ± 17.3 Mg-Si day^{-1}) (Fig. 3-8g, h). Seasonal variations in the fluxes of PO_4^{3-} and DSi were smaller (CVs of 0.52 and 0.51, respectively) than in those of NO_x (CV = 1.02).

Maizuru Bay is another potential source of nutrients to Tango Bay; however, this nutrient input (~0.1 Mg-N day^{-1}; Miwa and Ikeno, 2008) was one order of magnitude lower than the riverine nutrient fluxes from Yura River and the entrained fluxes of nutrients (Fig. 3-8).

The model selection results for seasonal fluctuations in chl. *a* in the water column

supported the effects of the entrained flux of NO_x and D_E with a 1-month time lag (Table 3-2). The model that had the lowest AIC value for the 1-month time lag also included the riverine NO_x flux; however, the Δ_i and ω_i values of the model were similar to those of the $\overline{N_O} + \overline{D_E}$ model. The model with the lowest AIC value for the 0-month time lag also included the entrained flux of NO_x and D_E, but six models (including a null model) had similar values of Δ_i and ω_i (Table 3-2).

Discussion and conclusions

Nutrient limitation of coastal phytoplankton

Spatiotemporal changes in nutrient concentrations show that seasonal patterns in nutrient limitation are affected by both the freshwater inflow and the entrainment of oceanic water in Tango Bay. Between November and January, nutrient concentrations were higher than the average half saturation concentration (K_s) required for phytoplankton uptake (1.0 μM dissolved inorganic N, 0.2 μM PO_4^{3-}, and 2.0 μM DSi) (Dortch and Whitledge, 1992). Nutrient ratios during this time were also similar to the Redfield ratio (Fig. 3-6), indicating that nutrient levels were not potential limits on primary production.

Nutrient consumption by blooming phytoplankton leads to severe nutrient depletion in late spring (Figs. 3-2, 3-4, and 3-5). The nutrient supply from the deeper zone (>50 m) also decreased after April owing to the weakening of vertical mixing (Fig. 3-5g–i; Kim et al., 2012). NO_x and PO_4^{3-} concentrations were below the average K_s in April; thus, phytoplankton growth would have been potentially limited by both nutrients during this period (Fig. 3-2c, d). The increased phytoplankton growth with the simultaneous supply of N and P in bioassays (Fig. 3-7a–f) supported this conclusion.

Both NO_x and PO_4^{3-} in the bottom water decreased below the average K_s between May

Table 3-2. Model selection results for riverine NO_x flux ($\overline{N_R}$), NO_x flux driven by estuarine circulation ($\overline{N_O}$), and the depth of the euphotic zone ($\overline{D_E}$) explaining seasonal change in the monthly mean values of the water column chl *a* concentrations. The estimated coefficient and the standard error (in parentheses) are shown for each explanatory variable. *df*, AIC, Δ_i, and ω_i indicate the degrees of freedom, the Akaike Information Criterion, AIC differences, and AIC weights, respectively. Models with small Δ_i (<2) are represented in this table. The 1-month time lag accounts for a 1-month delay in the chl *a* response to NO_x inputs and D_E changes. **, p<0.01.

GLMs	$\overline{N_R}$	$\overline{N_O}$	$\overline{D_E}$	*df*	AIC	Δ_i	ω_i
1-month time lag							
$\overline{N_R} + \overline{N_O} + \overline{D_E}$	0.028 (0.023)	0.265 (0.074)**	0.082 (0.024)**	5	30.8	0.00	0.408
$\overline{N_O} + \overline{D_E}$		0.241 (0.076)**	0.090 (0.027)**	4	31.0	0.17	0.375
0-month time lag							
$\overline{N_O} + \overline{D_E}$		0.121 (0.081)	0.065 (0.040)	4	38.3	0.00	0.236
Null model				2	38.9	0.60	0.175
$\overline{N_O}$		0.084 (0.075)		3	39.0	0.67	0.169
$\overline{N_R} + \overline{N_O} + \overline{D_E}$	0.016 (0.034)	0.120 (0.085)	0.060 (0.041)	5	40.0	1.68	0.102
$\overline{N_R}$	0.073 (0.059)			3	40.0	1.76	0.098
$\overline{D_E}$			0.043 (0.051)	3	40.1	1.86	0.093

and October (Fig. 3-2c, d), indicating severely nutrient-limited conditions (Figs. 3-6 and 3-7g–l). Chl. *a* concentrations were high in a thin surface layer in summer (Fig. 3-2f); however, this accumulated phytoplankton was occupied by freshwater phytoplankton flowing out of the river (Watanabe et al., 2014), and would not contribute to the coastal phytoplankton production (Fig. 3-2g).

To examine how NH_4^+ affected nutrient limitation, I conducted stoichiometric analysis using the NH_4^+ concentration data from July 2007 to March 2008 (Watanabe et al., 2014). The spatiotemporal changes in potentially limiting nutrients (Appendix Fig. S3-2) were similar to the results in Fig. 3-6; i.e., N and P were potential limits in the bottom and surface waters, respectively. However, the N/P and N/Si ratios became closer to the Redfield ratio, suggesting that the NH_4^+ supply (e.g., riverine inputs and recycling in the coastal zone) might temporarily buffer the N limiting condition.

Effects of nutrient fluxes and light availability on seasonal fluctuations in phytoplankton

Oceanic nutrients entrained via estuarine circulation fuel coastal phytoplankton production in Tango Bay, which has been shown also in other open coastal systems (Davis et al., 2014). Results from the GLMs supported an increase in the water column chl. *a* with increases in both $\overline{N_O}$ and $\overline{D_E}$ with a 1-month time lag, and, in turn, did not support any influence of $\overline{N_R}$, $\overline{N_O}$, and $\overline{D_E}$ with the 0-month time lag (Table 3-2). The 1-month time lag between the observed increases in the NO_x flux and chl. *a* concentrations indicates that phytoplankton blooms start approximately 1 month after increases in the NO_x inflows in estuarine circulation (Figs. 3-2g, 3-4a, b, and 3-8f). This time lag may be caused also by other limiting factors, such as light availability (Figs. 3-3 and 3-4i–l; Shiozaki et al., 2014; Saba et al., 2015).

Seasonal changes in the depth of the euphotic zone also influence coastal phytoplankton

in Tango Bay (Table 3-2). The depth of the euphotic zone decreased from November to January, especially at shallow stations (e.g., station T1 and T2), and these decreases were not related to river runoff. The northwesterly wind induced by the winter monsoon is an important forcing component for the Sea of Japan and Tango Bay (Itoh et al., 2016). The shoaling of the euphotic zone depth with increases in turbidity would be caused by wind events in winter, and have inhibited phytoplankton production during the nutrient-rich period (November–January).

The influence of riverine NO_x fluxes on seasonal changes in chl. *a* concentrations in Tango Bay was poorly supported by the GLM outputs (Table 3-2). Nutrients in the river plume would not be used efficiently by coastal phytoplankton despite the sufficient light availability in the surface waters (Fig. 3-3). Riverine nutrients are efficiently transported offshore because of the microtidal conditions in Tango Bay, resulting in low availability of riverine nutrients to phytoplankton in the shallow coastal zone (<30 m). Davis et al. (2014) also found that terrestrial nutrients played only a minor role in an open coast phytoplankton assemblage.

Our results show that, during late spring and summer, the entrained low-nutrient seawater dilutes nutrient-replete freshwater and reduces primary production in this open bay. This dilution effect is illustrated by the nutrient and phytoplankton dynamics observed after the typhoons in May 2011, i.e., the high river discharge caused by the typhoons supplied large amounts of riverine nutrients (Fig. 3-8a–d) but entrained low-nutrient seawater from offshore (Fig. 3-8e–h), which induced low-nutrient and low-chlorophyll conditions (Fig. 3-2b–g). In turn, in semi-enclosed bays, the entrained water is nutrient-rich and supports phytoplankton growth year round because sedimentary organic matter is mineralized, increasing nutrient concentrations (Yamamoto et al., 2000; Sugimoto et al., 2010; Cloern et al., 2014). Thus, the relationship between freshwater flow and coastal primary production depends on the embayment degree (ED).

Drivers of phytoplankton blooms in winter and spring

Phytoplankton blooms in Tango Bay occurred between February and April in 2010 and 2011 (Figs. 3-2f, g, and 3-4a, b), as well as in other years (Kasai et al., 2010; Watanabe et al., 2014). However, riverine discharge transports surface phytoplankton offshore, resulting in low surface chl. *a* concentrations despite the nutrient-rich conditions and in the maximum chl. *a* values occurring in the middle layers (5–20 m).

The timing of the bloom matched those of increases in GSR and an increase in DE, suggesting that light would limit phytoplankton growth from December to February, despite nutrient-replete conditions (Fig. 3-4). Phytoplankton blooms under nutrient-limited conditions between March and April would be supported by additional nutrient inputs. These increases in phytoplankton biomass coincided with floods (river discharge >100 m^3 s^{-1}), suggesting that the freshwater flow drives oceanic nutrient inflows in spring. Recycled nutrients in Tango Bay could support the bloom during late spring, when the entrained flux of nutrients from the offshore declines because of weakened vertical mixing.

The dilution effect of estuarine circulation (Yamamoto et al., 2000; Harrison et al., 2008; Artigas et al., 2014) would create the nonlinear relationship between freshwater flux and blooms. The magnitude of the phytoplankton bloom was smaller in 2010 than in 2011 (Figs. 3-2f and 3-4a, b), while the entrained water flux was ~1.6 times larger in 2010 than in 2011 (Fig. 3-8e). The occurrence of shoaling of the euphotic zone would also inhibit phytoplankton production in March 2010 (Fig. 3-4k, l). However, other physical and biogeochemical factors (e.g., phytoplankton species composition, top-down effect of herbivores, wind, tide, and oceanic currents) should be assessed in future studies.

Influence of primary production on higher trophic levels in Tango Bay

Phytoplankton blooms from winter to early spring are mainly fueled by the entrainment of oceanic nutrients in Tango Bay. The biomass of secondary producers also increases during the blooms (Watanabe et al., 2014; Akiyama et al., 2015), which may regulate phytoplankton production via top-down control. Moreover, flounder and temperate seabass larvae and juveniles settle in the coastal zone during times of high production of their prey organisms (Takeno et al., 2008; Islam et al., 2010). When coastal phytoplankton production is limited by nutrients from late spring to summer, some juvenile temperate seabass migrate into the river, where the high abundance of prey enhances their growth relative to individuals remaining in the shallow coastal zone (Fuji et al., 2011; Fuji et al., 2014; Watanabe et al., 2014). These fish rely on seasonal fluctuations in both freshwater flow and coastal conditions (e.g. vertical mixing and wind events) that determine the dynamics of their prey.

Chapter 4:

Iron and fluorescent dissolved organic matter in an estuarine and coastal system in Japan

Introduction

Iron regulates primary productivity in large parts of the world's oceans (Martin and Fitzwater, 1988; Martin et al., 1994; Boyd and Ellwood, 2010; Boyd et al., 2010; Tagliabue et al., 2017). Substantial amounts of iron arising from various sources contribute to primary production. Atmospheric dust and upwellings of iron-rich deep waters supply considerable iron to the surface waters of the open ocean (Martin et al., 1989; de Baar et al., 1995; Coale et al., 1996). In coastal waters, sediment and riverine inputs are major iron sources (Elrod et al., 2004; Suzuki et al., 2014), supporting a high level of primary productivity.

The availability of iron to primary producers depends on the quantity and quality of organic ligands present (Maldonado and Price, 1999; Naito et al., 2008), because the solubility of iron(III) in oxic seawater is extremely low (0.08–0.2 nM; Kuma et al., 2000; Liu and Millero, 2002). More than 99% of the dissolved iron (DFe) is bound to organic ligands in coastal waters (Gledhill and van den Berg, 1994; Laglera et al., 2007). Iron-binding organic ligands include dissolved organic matter (DOM), such as humic substances (Laglera and van den Berg, 2009). In estuarine and coastal systems, terrestrial-derived humic substances comprise the largest fraction of organic ligands (Laglera et al., 2007; Laglera and van den Berg, 2009).

The freshwater–seawater mixing process also affects iron–ligand complexation (e.g., Fujii et al., 2008) and controls the iron flux to coastal waters. Freshwater inflows deliver substantial amounts of iron to estuarine and coastal ecosystems; however, much of the incoming iron is rapidly scavenged during the mixing process. Iron and organic ligands are simultaneously

removed from the water column by salt-induced flocculation onto settling particles in DOM-rich estuaries (Boyle et al., 1977; Sholkovitz et al., 1978; Nowostawska et al., 2008). The aggregation of colloidal iron with increasing salinity is an important removal process (Fox and Wofsy, 1983).

The fluorescent characteristics of DOM are widely used to determine the source and fate of DOM in aquatic environments (e.g., Stedmon and Bro, 2008; Yamashita et al., 2008). Measurement of these characteristics provides a relatively simple tool for monitoring DOM behavior with high sample throughput. Previous studies have shown that the distribution of humic-like fluorescent DOM is closely related to that of DFe in the North Pacific Ocean, the Arctic Ocean, the Sea of Okhotsk, and the Sea of Japan (Tani et al., 2003; Takata et al., 2004, 2005; Kitayama et al., 2009; Yamashita et al., 2010; Nakayama et al., 2011), as well as in the Yukon River plume (Nishimura et al., 2012), suggesting that humic-like fluorescent DOM may control the distribution of DFe by providing organic ligands. However, the relationship between the fluorescent characteristics of DOM and DFe in estuarine and coastal systems is unknown.

In this study, I assessed the distribution of DFe and the fluorescent characteristics of DOM, as measured using fluorescence excitation-emission matrices (EEMs), along a salinity gradient from the upper reach of the Yura River estuary to the adjacent coastal zone. I also estimated the DFe removal rate using the relationship between DFe and salinity. Based on the results, I investigated the following questions. Is the correlation between the fluorescent characteristics of DOM and DFe also observed in estuarine and coastal systems? What is the influence of the freshwater–seawater mixing process on this relationship? How much does the mixing process affect the inflow of terrestrially derived DFe to the coastal zone?

Materials and methods

Study area

The Yura River is the largest river flowing into Tango Bay, which is an open bay in Japan (Fig. 4-1). The river has a total length of 146 km and a total catchment area of 1,880 km^2; 81% of its catchment area is covered with forest. The riverbed slope (1/188) is so steep that the retention time of the river water is short, and the water is relatively clear (less humic). The river discharge (annual mean < 50 m^3 s^{-1}; Kasai et al., 2010) is high from winter to spring (February to April) and from May to July because of snowmelt and high precipitation, respectively, whereas it is generally low from August to January (Watanabe et al., 2017). The downstream portion of the Yura River is classified as a salt-wedge estuary, with a spring tidal range < 0.5 m. The salt wedge often extends up to 20 km upstream when the river discharge is low (Kasai et al., 2010; Watanabe et al., 2014).

Field surveys

Field surveys were conducted in the downstream portion of the Yura River and in the coastal zone of Tango Bay. Surveys in the Yura River were conducted on July 17, August 19, and November 18, 2010, and on January 21, February 19, March 19, April 25, June 25, and July 26, 2011, at six sampling stations set between the river mouth and 16 km upstream from the river mouth (Y1–Y6; Fig. 4-1). Surveys in the coastal zone were conducted on July 15, 2010, February 17, April 26, and July 25, 2011, at seven sampling stations (T0–T6; Fig. 4-1). At each station, the vertical distributions of water temperature and salinity were measured using a CTD profiler (Compact-CTD; Alec Electronics, Kobe, Japan) before water sampling. Surface (depth 0.2 m) and bottom (depth 1.0 m above bottom; except for July 15, 2010) waters were collected at each station using an iron-free Van Dorn water sampler composed of a rubber tube, rubber

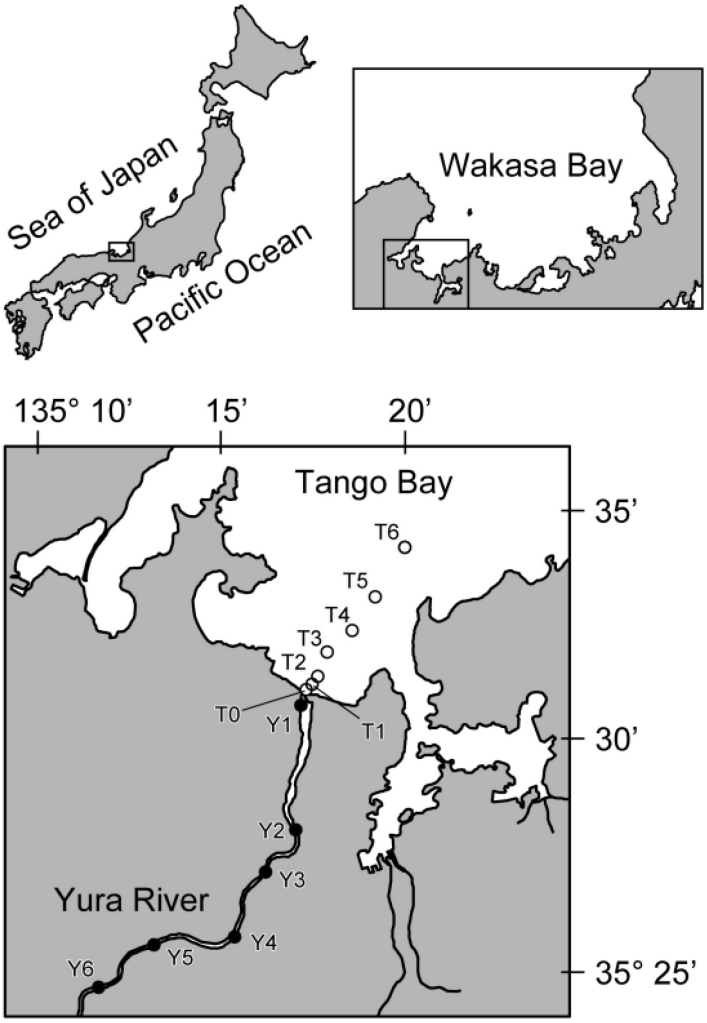

Fig. 4-1. Locations of the Yura River and Tango Bay. Closed and open circles indicate the river (Y1–Y6) and coastal (T0–T6) stations, respectively.

caps, and an acrylic cylinder. Mixed-layer water was also collected at river stations when the CTD profiler detected the halocline. Salinity was measured for each river water sample in situ using an electrical conductivity meter (SC72; Yokogawa Electric, Tokyo, Japan). The river and coastal water samples were stored in acid-washed polyethylene bottles and surface contamination clean (SCC) bottles (AS ONE, Osaka, Japan), respectively, and transported to the laboratory under refrigeration.

The daily mean river discharge (measured at Hami Bridge, 25 km upstream from the river mouth) of the Yura River was obtained from the Ministry of Land, Infrastructure, Transport, and Tourism, and from the Meteorological Agency.

Iron analysis

Water samples were filtered immediately at the laboratory. For DFe (< 0.7-μm fraction) analysis, the water samples were filtered through glass-fiber filters (GF/Fs; Whatman, Maidstone, UK) washed with 2 N HCl into SCC bottles (AS ONE). The filtered samples were adjusted to 0.275 N HNO_3^- by adding concentrated HNO_3^- (Ultrapur-100; Kanto Chemical Co., Inc., Tokyo, Japan) and stored until analysis at room temperature.

The DFe concentrations in river samples were measured using an inductively coupled plasma atomic emission spectrometer (iCAP6000; Thermo Fisher Scientific Inc., Waltham, MA, USA). The detection limit of this method was 7 nM (three times the standard deviation of the blank measurements). Coastal samples were concentrated and desalted by solid-phase extraction with chelating resins (Nobias CHELATE PA1; Hitachi High-Tech Fielding, Tokyo, Japan), which contained ethylenediaminetriacetic acid and iminodiacetic acid functional groups immobilized on hydrophilic methacrylates (Sohrin et al., 2008; Aimoto et al., 2011) to eliminate measurement interference caused by coexistence in the matrix. The concentrated samples were

measured by inductively coupled plasma mass spectrometry (SPQ-9000; SII NanoTechnology, Inc., Chiba, Japan) under cool plasma conditions (RF power; 0.65 kW). The reliability of the sample preparation procedure was confirmed by analyzing seawater certified reference materials (CASS-4 and CASS-5; National Research Council of Canada, Ottawa, Canada). The certified DFe concentrations in CASS-4 and CASS-5 were 12.7 ± 1.0 and 25.7 ± 1.9 nM, respectively, and the measured concentrations were 12.2 ± 0.2 and 25.3 ± 0.2 nM (n = 5). The detection limit of this method was estimated to be 0.09 nM. Filter blanks, prepared by filtering Milli-Q water through acid-washed GF/Fs, were ~ 3 nM.

Dissolved organic matter analysis

For DOM analysis, water samples were filtered through precombusted (450°C for 4 h) GF/Fs (Whatman). The dissolved organic carbon (DOC) concentrations of the filtered samples were determined via high-temperature catalytic oxidation with a total organic carbon (TOC) analyzer (TOC-V CSH; Shimadzu, Kyoto, Japan).

The three-dimensional EEM spectra of the filtered samples were measured using a spectrofluorometer (F-7000; Hitachi High-Technologies, Tokyo, Japan) equipped with a 150-W xenon lamp. Spectral correction was conducted with rhodamine B solution, according to the instrument operation manual and a method described by Yoshioka et al. (2007). The scanning ranges were 250–400 nm for excitation (Ex) and 250–500 nm for emission (Em). Fluorescence intensity (FI) was measured at 5-nm intervals for Ex and 1-nm intervals for Em. The EEM spectrum of ultrapure water (Milli-Q; Millipore, Billerica, MA, USA) was subtracted from each sample EEM spectrum for correction, and daily FI variations were standardized using the area of the Milli-Q water Raman peak at an excitation of 350 nm (Cory and McKnight, 2005).

To assess the characteristics of the DOM components, I applied parallel factor analysis (PARAFAC) to EEMs in water samples. PARAFAC statistically decomposes the complex mixture of DOM fluorophores into individual, quantifiable components, based on an alternating least-squares algorithm (Stedmon et al., 2003; Chen et al., 2010). The PARAFAC model used in this study included EEMs from approximately 500 estuarine and coastal water samples taken during the field survey in this study and 500 stream and river water samples from the Yura River basin. The stream and river water samples were collected bimonthly from 54 stations in the river basin (Appendix Fig. S4-1). The EEMs of the samples were determined using the method described above. For PARAFAC modeling, a matrix of excitation wavelengths of 260–400 nm and emission wavelengths of 250–500 nm was used due to the low precision of the FI values at wavelengths of 225–255 nm (Yamashita and Tanoue, 2003). The analysis was conducted in MATLAB (Mathworks, Natick, MA, USA) with the DOMFluor toolbox (Stedmon and Bro, 2008). Split-half analysis (Stedmon et al., 2003) and random initialization (Stedmon and Bro, 2008) were used to validate the identified components.

Following established protocols in this research field, the humic-type fluorescence intensity (H-flu) (Tani et al., 2003) was determined using excitation at 320 nm and emission at 420 nm.

Other chemical analyses

For the chlorophyll *a* (chl. *a*) analyses, the GF/Fs used for DOM analyses were extracted in the dark for 12 h in 90% acetone, and chl. *a* concentrations were measured using a calibrated fluorometer (Trilogy; Turner Designs, Sunnyvale, CA, USA).

Estimation of the effective zero-salinity endmember of DFe concentration

To quantify iron removal in the freshwater–seawater mixing process, the effective zero-salinity endmember of DFe concentration was estimated for coastal samples obtained on July 15, 2010, and February 17, April 26, and July 25, 2011. The effective zero-salinity endmember, defined as the theoretical riverine DFe concentration entering the coastal zone, was determined by fitting a linear regression to DFe concentrations and salinity over the range where DFe variation was conservative (Boyle et al., 1974; Nishimura et al., 2012; Liu et al., 2014). The conservative area was identified to maximize the correlation coefficient (e.g., Michel et al., 2000; Dabrin et al., 2009).

Results

Changes in dissolved iron and dissolved organic matter characteristics

The DFe concentration decreased exponentially with increasing salinity, and the concentration (mean ± standard deviation of DFe, 10 ± 4 nM) in the high-salinity (> 30) zone was lower than that in freshwater (1280 ± 788 nM) by at least two orders of magnitude (Fig. 4-2a–d). The DFe concentration decreased significantly over the salinity range of 0–10. The change in DOC concentration was more stable than the change in DFe concentration during the mixing process, with concentrations in the range of 48–123 μM (Fig. 4-2e, f). Chl. *a* concentrations were high in high-salinity river water (Fig. 4-2g, h).

Six fluorescent DOM (FDOM) components were identified via PARAFAC analysis of the samples collected from the river, estuary, and coastal zone. The spectral characteristics of the components (Table 4-1 and Appendix Fig. S4-2) identified in the Yura River–Tango Bay system were very similar to those of FDOM in other aquatic environments identified previously by PARAFAC analysis (e.g., Coble et al., 1998; Yamashita et al., 2008). Based on the fluorescence characteristics, the components could be categorized into terrestrial humic-like (C1, C2, C4, and

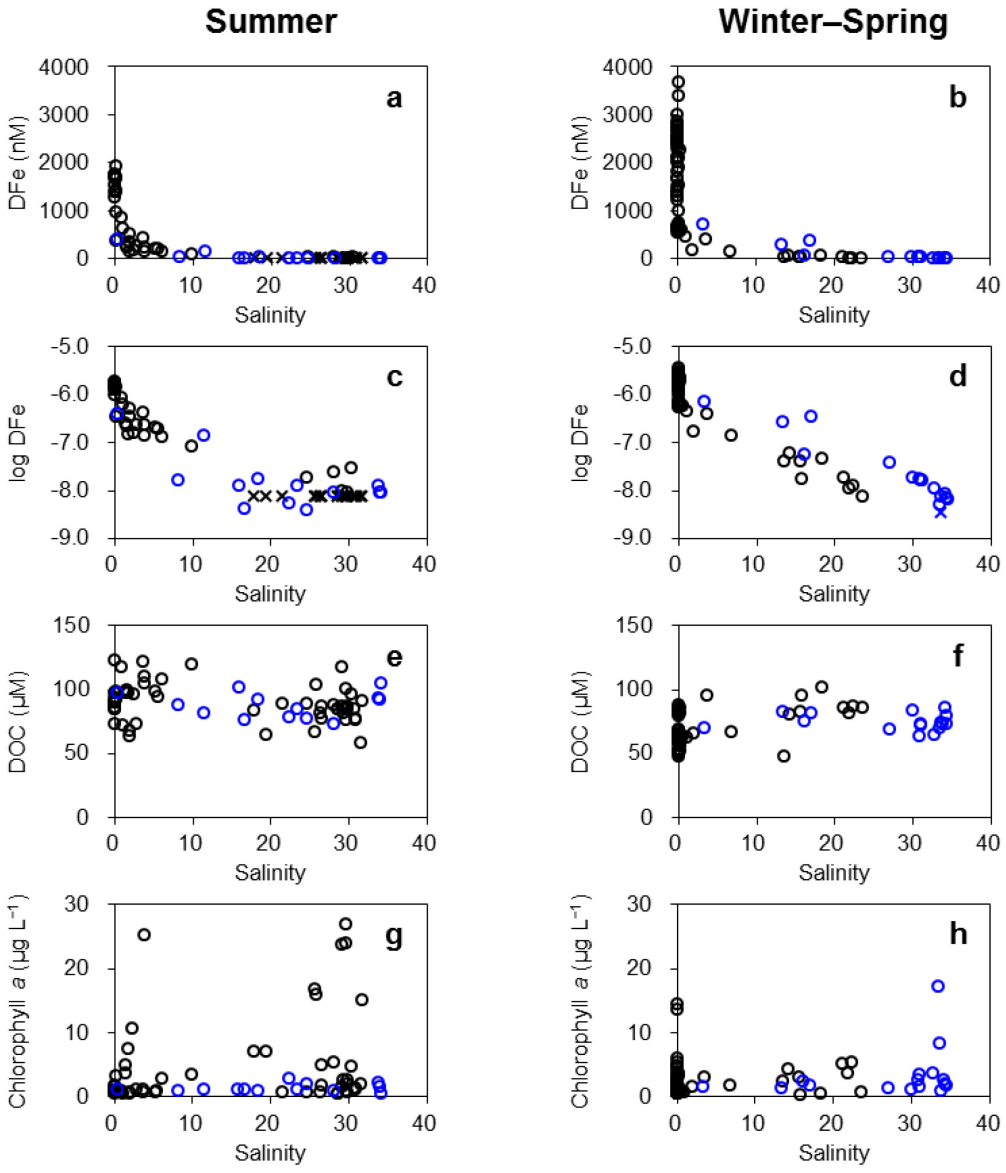

Fig. 4-2. Variations in the (**a**, **b**) dissolved iron (DFe) concentration, (**c**, **d**) logDFe, (**e**, **f**) dissolved organic carbon (DOC) concentration, and (**g**, **h**) chlorophyll *a* concentration along a salinity gradient in the Yura River–Tango Bay system. Black and blue circles indicate the values obtained in the riverine and coastal zones, respectively. DFe values below the detection limit or the filter blank are indicated with cross marks.

Table 4-1. Tentative assignments of parallel factor analysis components detected in water samples from the Yura River–Tango Bay system (n = 1088).

Component	Ex (nm)	Em (nm)	Coble's definition[1]	Tentative source assignment
C1	270, 380	477	—	Terrestrial humic, Allochthonous, Processing of terrestrial OM[2]
C2	260	464	A	Humic-like, Terrestrial origin
C3	310	397	M	Marine humic, Autochthonous, Anthropogenic
C4	345	435	C	Humic-like, Terrestrial origin
C5	275	326	T	Protein-like, Tryptophan like
C6	260	500	A'	Humic-like, Terrestrial origin

[1]Coble et al. 1998, [2]Yamashita et al. 2008.

C6), marine humic-like (C3), and protein-like (C5) components (Table 4-1). Because the peak for C6 was considered to be outside the analytical range, it was not included in further analysis (Appendix Fig. S4-2).

In general, the FI values of all FDOM components were high in riverine freshwater and low in saltwater throughout the system (Fig. 4-3), and they decreased with increasing salinity (Table 4-2); however, C1–C4 varied substantially in high-salinity water of the river stations when the chl. *a* concentration increased (Fig. 4-2). The marine endmembers of each component had temporally stable values (C1, 0.014 ± 0.009 RU; C2, 0.018 ± 0.020 RU; C3, 0.019 ± 0.008 RU; C4, 0.010 ± 0.007 RU; C5, 0.020 ± 0.007 RU). In contrast, the riverine endmembers of each component showed relatively large variations (C1, 0.056 ± 0.027 RU; C2, 0.072 ± 0.048 RU; C3, 0.056 ± 0.028 RU; C4, 0.050 ± 0.025 RU; C5, 0.044 ± 0.030 RU) and tended to be high in summer. H-flu generally decreased along the salinity gradient, but was high in saltwater within the river (Table 4-2, Fig. 4-3k, l).

Salinity was significantly correlated with DFe, DOC, FDOM components, and H-flu (Table 4-2, $p < 0.05$). DFe was positively correlated with C1 and C4, but the correlation coefficients were low ($r = 0.20$ and 0.22, respectively). The correlations among DOC, FDOM components, and H-flu were significantly positive ($p < 0.01$).

Riverine inflow of dissolved iron and dissolved organic matter

DFe concentrations in riverine freshwater at station Y6 displayed temporal variability (356–2640 nM), with the maximum concentration occurring in February 2011 (Table 4-3). DOC concentration and FDOM variables were relatively stable, but were high during summer. The DFe concentration of riverine freshwater was correlated positively with river discharge (Table

4-4). DOC concentration, FDOM components, and H-flu were correlated positively with water temperature (Table 4-4).

Effective zero‐salinity endmember of DFe concentration

The effective zero-salinity endmember of DFe concentration ranged from 17 ± 4 to 101 ± 10 nM (estimated mean ± 95% confidence interval), with relatively high values in February and April 2011 (Fig. 4-4, Table 4-5). The salinity range of the conservative dilution area ranged from 8.2 to 34.4 (Fig. 4-4, Table 4-5). The estimated removal rate of DFe through the mixing process was greater than 94% (Table 4-5).

Discussion

Relationship between iron and humic-like FDOM

The distribution of DFe (< 0.7-μm fraction) was not closely related to that of either humic-like FDOM components or H-flu in the Yura River–Tango Bay system (Table 4-2). Riverine DFe concentration decreased exponentially along the salinity gradient, particularly at the salinity level of ~ 10 (Fig. 4-2a–d and Appendix Fig. S3); however, allochthonous humic-like FDOM components (i.e., C1, C2, and C4) and H-flu decreased conservatively with increasing salinity (Fig. 4-3). This difference in behavior between DFe and humic-like FDOM indicates that humic-like FDOM is not the main regulator of DFe concentration in this estuarine and coastal system.

The DFe distribution is strongly correlated with that of H-flu in the offshore region (Tani et al., 2003; Takata et al., 2004, 2005; Kitayama et al., 2009; Yamashita et al., 2010; Nakayama et al., 2011). In contrast, the DFe concentration in the shelf region is higher than the Fe(III) hydroxide solubility estimated from the correlation with H-flu (Nakayama et al., 2011; Hioki et

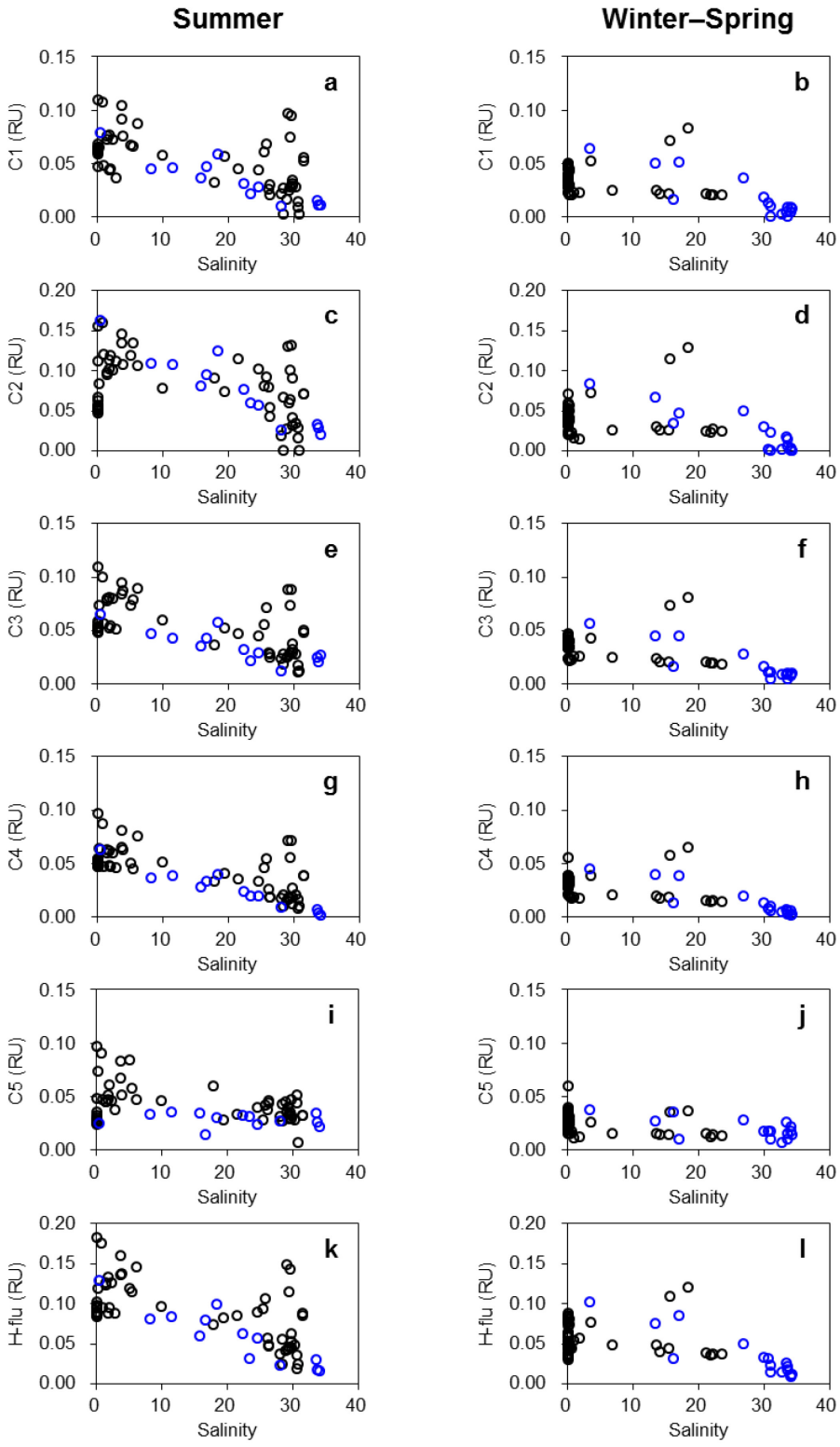

Fig. 4-3. Variations in the five components (C1–C5) that result from PARAFAC analysis and humic-type fluorescence intensity (H-flu) in the Yura River–Tango Bay system. Black and blue circles indicate the values obtained in the river and coastal zones, respectively.

Table 4-2. Pearson's correlation coefficients (*r*) among dissolved iron (DFe), dissolved organic matter variables, and salinity (n = 146, $p < 0.05$). Bold indicates $p < 0.01$.

Parameter	DFe	DOC	C1	C2	C3	C4	C5	H-flu	Salinity
DFe		−0.19	0.20	—	—	**0.22**	—	—	**−0.67**
DOC			**0.57**	**0.54**	**0.56**	**0.49**	**0.42**	**0.59**	0.19
C1				**0.82**	**0.97**	**0.97**	**0.56**	**0.94**	**−0.42**
C2					**0.87**	**0.82**	**0.69**	**0.88**	−0.20
C3						**0.96**	**0.66**	**0.96**	**−0.39**
C4							**0.61**	**0.95**	**−0.51**
C5								**0.64**	−0.17
H-flu									**−0.36**
Salinity									

Table 4-3. River discharge (Q), water temperature, dissolved iron (DFe), dissolved organic carbon (DOC), and FDOM variables of surface water at station Y6, 16 km upstream from the river mouth.

Date	Q (m^3 s^{-1})	Temperature (°C)	DFe (nM)	DOC (μM)	C1 (RU)	C2 (RU)	C3 (RU)	C4 (RU)	C5 (RU)	H-flu (RU)
17 Jul 2010	143	22.3	1400	86	0.060	0.047	0.049	0.047	0.026	0.086
19 Aug 2010	22	29.6	356	92	0.065	0.084	0.073	0.064	0.073	0.119
18 Nov 2010	20	12.5	546	68	0.022	0.020	0.023	0.021	0.019	0.047
21 Jan 2011	44	4.8	739	53	0.030	0.034	0.036	0.034	0.036	0.052
19 Feb 2011	251	6.0	2640	63	0.039	0.038	0.037	0.031	0.020	0.035
19 Mar 2011	95	7.4	1210	58	0.031	0.050	0.034	0.032	0.033	0.058
25 Apr 2011	142	11.7	2430	81	0.050	0.047	0.040	0.036	0.023	0.076
25 Jun 2011	52	24.8	1270	123	0.109	0.155	0.109	0.096	0.096	0.182
26 Jul 2011	25	24.4	965	73	0.047	0.112	0.058	0.052	0.048	0.101

Table 4-4. Pearson's correlation coefficients (*r*) among river discharge (Q), water temperature (WT), dissolved iron (DFe), and dissolved organic matter variables of surface water at station Y6, 16 km upstream of the river mouth (n = 9, $p < 0.05$). Bold indicates $p < 0.01$.

Parameter	Q	WT	DFe	DOC	C1	C2	C3	C4	C5	H-flu
Q		—	**0.90**	—	—	—	—	—	—	—
WT			—	0.76	0.69	0.71	0.74	0.75	0.69	**0.80**
DFe				—	—	—	—	—	—	—
DOC					**0.96**	0.78	**0.90**	**0.90**	0.78	**0.93**
C1						**0.85**	**0.96**	**0.96**	**0.84**	**0.94**
C2							**0.93**	**0.93**	**0.89**	**0.93**
C3								**0.99**	**0.95**	**0.97**
C4									**0.94**	**0.98**
C5										**0.92**
H-flu										

Table 4-5. Linear regression of the conservative dilution line, R^2, number of points used, effective zero salinity end-member of DFe concentrations (DFe_0) with 95% confidence interval, in situ DFe concentrations at station Y6 (DFe_{FW}), and DFe removal rate. Removal rate is represented as a mean value and 95% confidence interval.

Sampling	Linear regression	R^2	n	Salinity range	$DFe_0 \pm CI95\%$ (nM)	DFe_{FW} (nM)	Removal (%)
July 2010	DFe = 56.9 − 2.2 × S	0.92	3	18.4–24.6	57 ± 27	1400	96 (94–98)
February 2011	DFe = 100.7 − 2.8 × S	0.98	7	16.2–33.7	101 ± 10	2640	96 (96–97)
April 2011	DFe = 94.8 − 2.6 × S	0.98	5	29.9–34.4	95 ± 13	2430	96 (96–97)
July 2011	DFe = 17.4 − 0.2 × S	0.67	7	8.2–34.1	17 ± 4	965	98 (98–99)

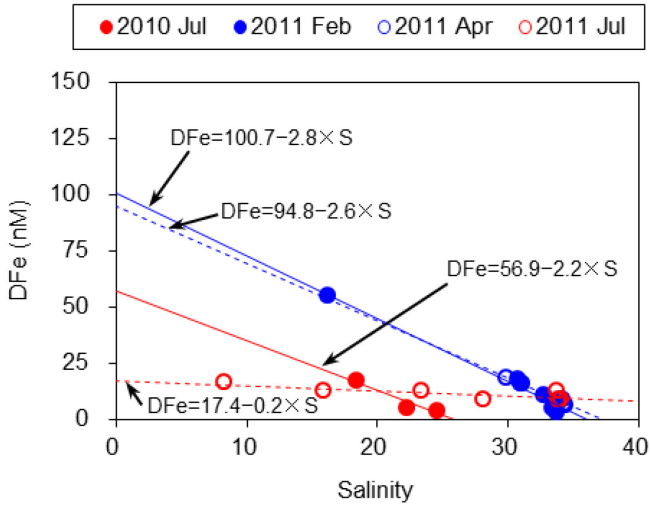

Fig. 4-4. Relationships between salinity and dissolved iron (DFe) at a salinity range in which DFe concentrations change conservatively in the Tango Bay coastal zone. The intercept indicates the effective zero-salinity endmember of DFe concentration.

al., 2014). The supply of colloidal iron from shelf sediments has been suggested as a potential iron source (Kuma et al., 2000; Bergquist et al., 2007; Fujita et al., 2010) that induces the difference in behavior between iron and humic-like FDOM (Hioki et al., 2014).

A linear relationship between DFe and H-flu was observed over the salinity range 26–33 in the Yukon River plume region (Nishimura et al., 2012). The riverine H-flu is ~ 1.5 RU (converted from quinine sulfate units [QSU] using the equation RU = $QSU_{320/420}$ × 0.012; Heller et al., 2013; Hioki et al., 2014), which is approximately 10 times higher than the H-flu (~ 0.18 RU) in the Yura River. The DFe concentration in Tango Bay was higher than that predicted from the relationship between DFe and H-flu in the Yukon River plume region and considerably higher than the Fe(III) hydroxide solubility estimated from H-flu (Fig. 4-5). Rapid DFe supply, including colloidal Fe, from the river may exceed the scavenging DFe removal rate, which probably contributes to the poor correlation between DFe and humic-like FDOM in Tango Bay. The DFe and H-flu measured using 0.7-μm GF/F filters in this study would contain a higher proportion of the colloidal fraction than values obtained in previous studies (< 0.22 μm, Kitayama et al., 2009; Nishimura et al., 2012). Differences in the filtration procedure may be one reason that the DFe concentration in Tango Bay was higher than that predicted from the relationship between DFe and H-flu in previous studies.

Behavior of iron and dissolved organic matter in the estuarine and coastal system

The sharp decrease in DFe concentrations at low salinities shows that a large proportion of the riverine DFe is removed in the mixing zone of the estuarine and coastal system. Iron removal is a common phenomenon in estuaries (e.g., Boyle et al., 1977; Mayer, 1982; Buck et al., 2007). Co-precipitation of iron and organic matter is an important contributor to iron removal in several humic estuaries (Boyle et al., 1977; Sholkovitz et al., 1978). However, DOC

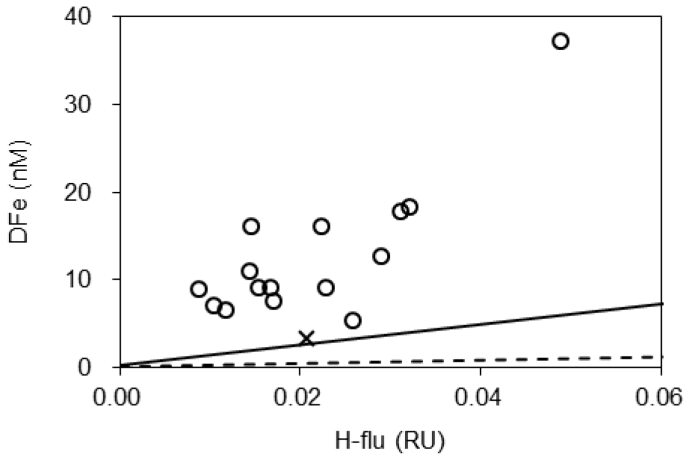

Fig. 4-5. Relationship between DFe and humic-type fluorescence intensity (H-flu) over a salinity range of 26–35 in the coastal zone. DFe values below the detection limit or the filter blank are indicated with cross marks. The solid line shows the linear relationship between DFe and H-flu in the Yukon River plume (DFe [nM] = 116.5 × H-flu [RU] + 0.249, Nishimura et al. 2012). The dashed line represents the linear relationship between Fe(III) hydroxide solubility (Fe(III)sol) and H-flu in the central North Pacific Ocean (Fe(III)sol [nM] = 18.87 × H-flu [RU] − 0.045, Kitayama et al. 2009). Fluorescence intensity values from previous works were converted from quinine sulfate units (QSU) using the equation RU = $QSU_{320/420}$ × 0.012 (Heller et al. 2013; Hioki et al. 2014).

and humic-like FDOM exhibit relatively conservative behavior, suggesting that co-precipitation of iron with organic ligands is not the major factor, but that instead the aggregation of colloidal inorganic iron (Fox and Wofsy, 1983; Stolpe and Hassellöv, 2007) is likely the key mechanism of iron removal in the Yura River–Tango Bay system.

Recent studies have shown that humic substances can act as the dominant iron-binding ligands in shallow coastal waters (Laglera et al., 2007; Laglera and van den Berg, 2009; Bundy et al., 2015; Krachler et al., 2015). The spectral characteristics of C4 in the Yura River–Tango Bay system are similar to those of humic substances (HS) (peak at excitation 355 nm and emission 440 nm, Determann et al., 1994). Based on the reported specific FI for 1 mg-HS L^{-1} in seawater of 0.06–0.11 RU (Determann et al., 1994), the marine and riverine endmembers of HS are estimated to be approximately 0.08–0.16 and 0.42–0.81 mg-HS L^{-1}, respectively. Using the reported binding capacity of HS (32 nmol-Fe mg-HS^{-1}, Laglera and van den Berg, 2009), the potential concentrations of HS-binding iron in this study are approximately 2.7–5.1 and 13–25 nM for the marine and riverine endmembers, respectively. The DFe concentration of the riverine water is much higher than this estimate, suggesting that a large portion of the riverine DFe (< 0.7-μm fraction) is probably colloidal inorganic iron. In contrast, the DFe concentration in coastal water is similar to its estimated value, demonstrating that colloidal inorganic iron would be precipitated in the mixing process, and iron–HS complexes would be transported to the coastal zone. In spite of the fact that HS estimates based on FDOM characteristics remain uncertain, the tentative quantification method could be useful.

The conservative dilution of terrestrial FDOM components, such as C1, C2, and C4, is a common phenomenon in rivers (e.g., Koyama et al., 2007; Yamashita et al., 2008). C3 and C5 fluorophores dominated in coastal waters (Fig. 4-3 and Appendix Fig. S4-4), but intensities were greater in the riverine water (Fig. 4-3). These results indicate that conventional marine

humic- and protein-like components may also be produced by freshwater microbes in the upper region of the river and transported to the coastal zone. Furthermore, every component increased when the chl. *a* concentration was high in the salt-wedge, implying that autochthonous production and the subsequent degradation of organic matter supply these humic- and protein-like components (Fukuzaki et al., 2014). These components may also act as organic ligands (Vraspir and Butler, 2009; Fukuzaki et al., 2014).

A number of previous studies have used DOC concentration to investigate the relationship between iron and terrestrially derived DOM. However, DOC concentration is not a suitable indicator of terrestrial-derived DOM in less-humic mountainous basins, such as the Yura River, where riverine DOC concentrations are similar to those in coastal waters (Fig. 4-2e, f). FDOM properties can be used as powerful indicators of terrestrial-derived DOM, especially in mountainous basins.

Riverine supply of dissolved iron and iron removal in the estuary

The positive correlation between DFe concentration and river discharge indicated that seasonal floods transported DFe to the estuary effectively (Table 4-4). The increase in DFe, which corresponded to flooding, was induced mainly by the outflow of colloidal inorganic iron because DOC and FDOM components did not increase during flooding (Table 4-3). A positive correlation between the DFe concentration and river discharge has been reported in humic basins (Cossa et al., 1990; Knorr, 2013; Nagao et al., 2014; Guan et al., 2015). The increase in DFe was accompanied by an increase in DOC in these basins, indicating that the supply of Fe–ligand complexes was the main controlling factor (Knorr, 2013; Nagao et al., 2014), unlike the mechanism in the Yura River. In these humic basins, wetlands are assumed to be an important source of Fe–ligand complexes during flooding (e.g., Nagao et al., 2014). Mountainous basins,

such as the Yura River, may have less capacity to transport Fe–ligand complexes than do humic basins.

The effective zero-salinity endmember of DFe concentration was at least 10 times lower than the riverine DFe concentration (Fig. 4-4, Table 4-5; 17–101 nM), indicating that more than 94% of the riverine DFe was removed in the low-salinity zone (salinity < 8). This removal rate falls into the highest range of values estimated for other estuaries (54–96%, Boyle et al., 1977; Sholkovitz et al., 1978; Nagao et al., 2010; Yang et al., 2017). This estimation shows that iron removal in the mixing process is an important regulator of riverine DFe supply in the Yura River–Tango Bay system, even though our filtration procedure may overestimate the value when compared with other studies that use filters with a pore size smaller than 0.7-μm GF/F.

The riverine concentration of HS-binding iron (13–25 nM) estimated from C4 is comparable to the effective zero-salinity endmember of DFe concentration. This result is consistent with the implication that a large proportion of colloidal inorganic iron is removed, and that iron–HS complexes make a substantial contribution to iron transport toward the coast.

Conclusion

This study illustrates the relationship between the behavior of DFe and FDOM variables in the estuarine and coastal system, suggesting the utility of FDOM measurements for evaluating riverine iron supply. The distribution of DFe (< 0.7-μm fraction) is not closely correlated to that of humic-like FDOM variables in the Yura River–Tango Bay system, in contrast to previous studies in offshore regions. Colloidal inorganic iron accounts for a large portion of the riverine DFe, and this form is removed in the mixing zone. In contrast, estimation of HS-binding iron from the FI of humic-like FDOM demonstrates that HS is likely an important iron transporter in this estuarine and coastal system. The iron removal process and the

behavior of humic-like FDOM have substantial effects on riverine DFe supply to the coast. Furthermore, FDOM properties are more sensitive indicators of terrestrial-derived DOM than is DOC concentration in low-humic mountainous basins. Accurate quantitative evaluation of the relationships between humic-like FDOM and ligands should be incorporated into future studies.

Chapter 5:

How organic carbon derived from multiple sources contributes to carbon sequestration processes in a shallow coastal system?

Introduction

The ocean functions as an important carbon sink by absorbing atmospheric CO_2 at a rate (2.3 ± 0.7 Pg-C yr^{-1}) comparable to the rate of CO_2 uptake by terrestrial ecosystems (2.6 ± 1.2 Pg-C yr^{-1}) (IPCC, 2013). One of the contributors to the ocean carbon sink is "blue carbon," which is carbon captured by marine organisms (Nellemann et al., 2009; Duarte et al., 2010; Duarte et al., 2013; Macreadie et al., 2014). Processes involved in carbon sequestration include carbon storage in sediments, carbon sequestration in the water column, and air–sea CO_2 exchange.

Blue carbon stored in sediment can be sequestered from atmospheric CO_2 for geological timescales (Mateo et al., 1997; McLeod et al., 2011; Fourqurean et al., 2012; Macreadie et al., 2012). The burial rate of organic carbon (C_{org}) is estimated to be higher in shallow coastal ecosystems (238 Tg-C yr^{-1}), such as estuaries and seagrass meadows, than in the open ocean (6 Tg-C yr^{-1}) (Nellemann et al., 2009). Furthermore, because shallow coastal ecosystems receive a substantial input of terrestrial carbon (0.9 Pg-C yr^{-1}), they store allochthonous carbon captured on land (Regnier et al., 2013). The most productive marine ecosystems are shallow coastal ecosystems (Bianchi, 2007) in which abundant C_{org} is produced via active photosynthesis by aquatic primary producers such as microalgae, macroalgae, and seagrass. Part of the produced C_{org} is stored in the sediments. For example, seagrass-derived C_{org} is estimated to contribute about 50% of sedimentary C_{org} (Kennedy et al., 2010). However, the variability of the origin of the C_{org} stored in sediments and the mechanisms mediating the composition of stored C_{org} are

largely unknown (Macreadie et al., 2012).

Although sequestration of C_{org} in the water column has the potential to sequester atmospheric CO_2, a mechanism for sequestering CO_2 in the water column of shallow coastal ecosystems has not been identified. In the open ocean, water column sequestration is considered to be an important carbon sink, because refractory dissolved organic carbon (DOC) can be sequestered from atmospheric CO_2 for geological timescales (Nagata, 2008; Jiao et al., 2010; Jiao et al., 2014). In shallow coastal ecosystems, aquatic primary producers, benefitting from the high nutrient concentrations and sufficient light conditions, generate a substantial amount of autochthonous DOC (Carlson, 2002; Wada et al., 2008; Agustí and Duarte, 2013). Thus, one can expect that refractory DOC may be sequestered in the water columns of shallow coastal ecosystems.

Air–sea CO_2 exchange is the process that directly determines whether a habitat is a sink or source of atmospheric CO_2. Shallow coastal ecosystems are considered to be a net source of atmospheric CO_2 due to their high rate of mineralization of terrestrial C_{org} (Borges, 2005; Borges et al., 2005; Cai et al., 2006; Chen and Borges, 2009; Cai, 2011; Regnier et al., 2013). However, recent studies have demonstrated that shallow coastal seagrass meadows in estuaries can be sinks for atmospheric CO_2 (Maher and Eyre, 2012; Tokoro et al., 2014). Whether the net ecosystem production (NEP) of seagrass meadows is positive or negative is a key determinant of whether they are sinks or sources, respectively, of atmospheric CO_2 (Maher and Eyre, 2012; Tokoro et al., 2014), but the linkages between the gas exchange process and C_{org} dynamics such as inflow/outflow and production/consumption remain unclear.

There is increasing interest in understanding the role of C_{org} derived from multiple sources in coastal carbon dynamics in response to global change (Bauer et al., 2013). Unlike sequestration in terrestrial ecosystems, water column C_{org} dynamics intervene and mediate the

above-mentioned key carbon sequestration processes in shallow coastal ecosystems. Furthermore, assessment of the dynamics should take into consideration the salinity gradient, because both freshwater and open ocean water affect shallow coastal ecosystems. In this study, I evaluated how C_{org} derived from multiple sources contributed to the processes of carbon sequestration and how the contribution changed along a salinity gradient in a shallow seagrass meadow. I quantified the origin and composition of the C_{org} (particulate organic carbon [POC], DOC, and sedimentary C_{org}) using elemental, isotopic, and optical signatures. I hypothesized that the composition of sedimentary C_{org} might be related to that of the POC in the water column (e.g., diffusion of terrestrial C_{org} in the water column would occur along the salinity gradient, whereas autochthonous C_{org} would be dominant in the productive zone of the estuary), and differences in the lability of the C_{org} sources could also modify the composition of the sedimentary C_{org}. In addition, I hypothesized that autochthonous C_{org} production decreased the concentration of dissolved inorganic carbon (DIC) in the water column and thereby contributed to air–sea CO_2 uptake, except in the low-salinity zone, where CO_2 dynamics were dominated by mineralization of terrestrial C_{org}.

Materials and methods

Study area

The Furen Lagoon in Japan is located at the boreal zone (43°19′46.5″N, 145°15′27.8″E), and has a surface area of 57.4 km^2 (Fig. 5-1). The lagoon is characterized by an average depth of about 1.0 m, and the lagoon mouth (depth: 13 m) connects the lagoon to the Sea of Okhotsk. The lagoon is brackish (salinity range: ~31), and the northern part of the lagoon receives freshwater from the Furen, Yausubetsu, and Pon-Yausubetsu Rivers. In the catchment, there are numerous pastures where livestock and fodder crops are grown, and wastes from the livestock

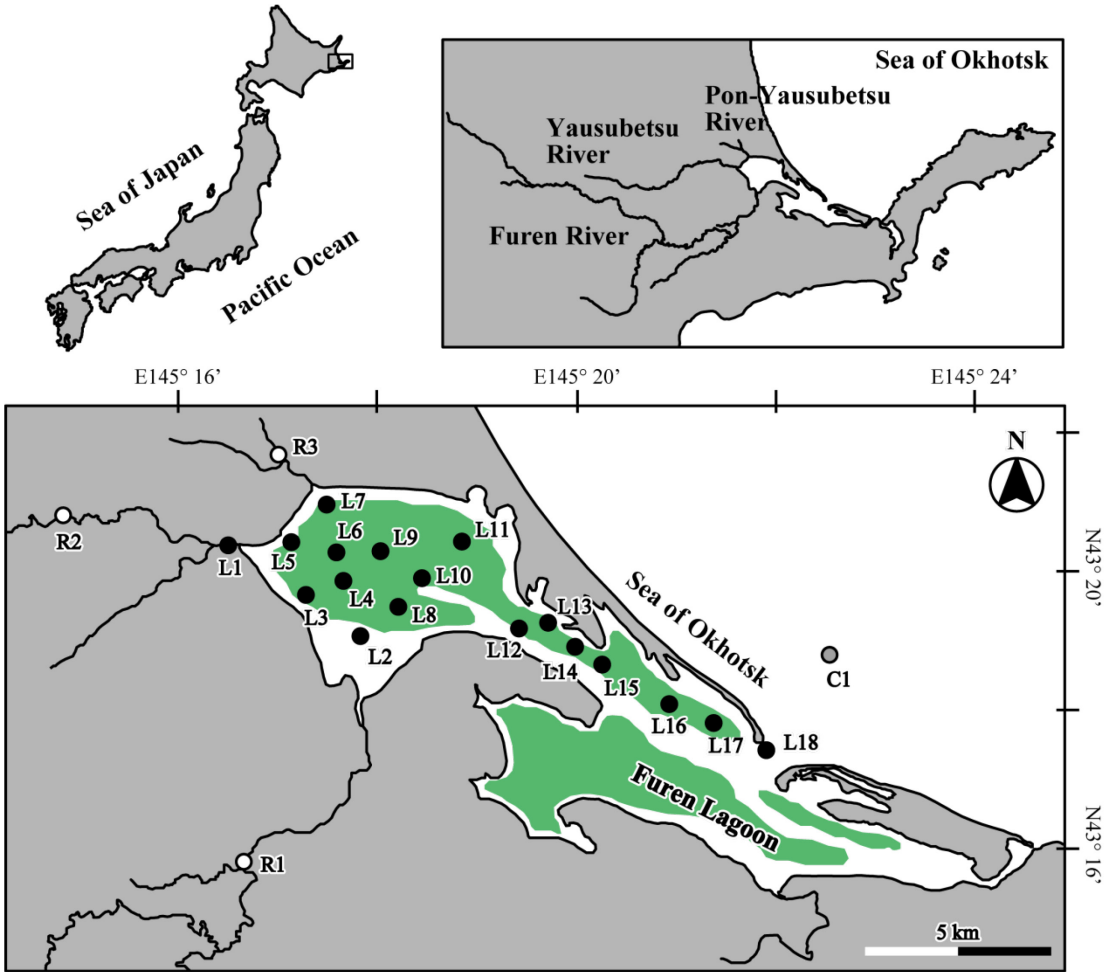

Fig. 5-1. Location of the Furen Lagoon and the catchment. Closed, gray-shaded, and open circles show lagoon stations, a coastal station, and river stations, respectively. The green-shaded area indicates the seagrass meadow area.

cause eutrophication (Montani et al., 2011). Seagrass meadows (dominant species: *Zostera marina*) occupy 67% of the total area of the lagoon. The aboveground biomass of seagrass ranges from 129 to 2440 g wet weight m^{-2} (Tokoro et al., 2014).

The Furen Lagoon is an ideal model site to evaluate the linkage between carbon dynamics and complicated environmental factors because the lagoon is highly enclosed and the C_{org} is derived from multiple sources. Furthermore, the lagoon includes habitats such as estuaries and seagrass meadows, which are hotspots of C_{org} accumulation (Kennedy et al., 2010).

Sample collection

Field surveys were conducted in August and October 2012 and June 2013 at 22 locations from the river mouths to the coastal zone (Fig. 5-1). Surface water samples for analysis of DIC, nutrients, and organic matter (OM) in the water column were collected in August 2012 at 18 stations (L1–L18) in the lagoon from a research vessel and at stations at each of the three river mouths (R1–R3). Samples of bottom water were collected from the mouth of the lagoon (station L18). An evaluation of temporal variations of the carbon sequestration processes was impossible from this single survey. However, our goal was to understand processes by relating the spatial pattern to salinity.

At each station, the salinity of the water was recorded by using a conductivity-temperature sensor (COMPACT-CT, JFE Advantech, Nishinomiya, Japan). Samples for DIC and the fugacity of CO_2 (fCO_2) were dispensed into 250-mL Schott Duran bottles, which were poisoned with mercuric chloride (200 μL per bottle) to prevent DIC changed due to biological activity. Water samples for the other analyses were collected in acid-washed polyethylene bottles. Samples for nutrients (NH_4^+, NO_2^-, and NO_3^-), total dissolved nitrogen (TDN), DOC, and optical analyses of chromophoric dissolved organic matter (CDOM)

were filtered through 0.2-μm polytetrafluoroethylene filters (DISMIC–25HP; Advantec, Durham, NC, USA) into precombusted (450°C for 2 h) 50-mL or 100-mL glass vials and frozen at –20°C until analysis. Samples for chlorophyll *a* (chl. *a*) concentrations and analyses of POC, particulate nitrogen (PN), and stable isotope analysis ($\delta^{13}C_{POC}$, and $\delta^{15}N_{PN}$) were obtained by filtration (~1 L) onto precombusted (450°C for 2 h) glass-fiber filters (GF/F, Whatman, Maidstone, Kent, UK) and stored in the dark at –20°C until analyses.

Sediment cores were collected in October 2012 at stations L7, L8, and L17 and in June 2013 at station C1 along a salinity gradient. The surface sediments (depth: 0–20 mm) of triplicate sediment cores (8.6-cm inner diameter) were used for analysis of total organic carbon (TOC) and total nitrogen (TN) concentrations and stable isotope signatures ($\delta^{13}C$ and $\delta^{15}N$).

To evaluate the contribution of phytobenthos to particulate organic matter (POM) in the water column and sedimentary OM, the stable isotope signatures and C/N ratio of the phytobenthos were measured. The dominant seagrass (*Z. marina*) and periphyton of the seagrass were collected in August 2012 at stations L6, L8, L13, and L17. Samples were kept at –20°C prior to analysis.

Analytical methods

DIC concentrations and fCO_2 values were determined on a batch-sample analyzer (ATT-05; Kimoto Electric, Osaka, Japan). DOC was determined via high-temperature catalytic oxidation with a TOC analyzer (TOC5000A; Shimadzu, Kyoto, Japan). Nutrient concentrations in sample filtrates were measured using an AutoAnalyzer (TRAACS 800; Bran+Luebbe, Norderstedt, Germany). TDN was measured via wet oxidation with persulfate (SWAAT; BL-Tec, Osaka, Japan). Concentrations of dissolved organic nitrogen (DON) were calculated as the differences between TDN and total DIN ($NH_4^+ + NO_2^- + NO_3^-$).

For the chl. *a* analyses, the GF/F filters were extracted in the dark for 12 h in 90% acetone, and chl. *a* concentrations were measured by using a UV-visible spectrometer (UV-2450; Shimadzu, Kyoto, Japan) (Lorenzen, 1967).

CDOM absorbance spectra were recorded from 250 to 700 nm at 1-nm increments using a UV-visible spectrometer (UV-2450; Shimadzu, Kyoto, Japan) fitted with a 1-cm quartz flow cell and referenced to ultrapure water (Milli-Q water; Millipore, Billerica, MA, USA). The absorbance values at each wavelength (λ) were transformed into absorption coefficients (a_{CDOM}) using:

$$a_{CDOM(\lambda)} = 2.303 \times A_{CDOM(\lambda)} \ (m^{-1})$$

where A_{CDOM} is the absorbance value per meter. The absorption value at 375 nm, $a_{CDOM(375)}$, was chosen to quantify CDOM because this wavelength has been commonly used as a metric of DOC absorbance in previous studies (e.g., Bricaud et al., 1981; Astoreca et al., 2009; Para et al., 2013). I also measured $a_{CDOM(254)}$ as a metric of the aromaticity of the DOM (e.g., Weishaar et al., 2003; Zurbrügg et al., 2013). I calculated specific UV absorption at 254 nm (SUVA254) using:

$$\text{SUVA254} = A_{CDOM(254)} / [\text{DOC}] \ (L\ mg^{-1}\ m^{-1})$$

where [DOC] is a DOC concentration. Spectral slopes for the interval of 275–295 nm ($S_{275–295}$) were calculated using linear regression of the log-transformed a_{CDOM} spectra. Slopes are reported as positive numbers to follow the mathematical convention of fitting to an exponential decay. Thus, higher (or steeper) slopes indicate a more rapid decrease in absorption with increasing wavelength (Helms et al., 2008).

Samples for analyses of TOC and TN content and stable isotope signatures ($\delta^{13}C$ and $\delta^{15}N$) were dried in an oven at 60°C or with a freeze dryer. To remove inorganic carbon, I acidified the samples with 1N HCl and dried them again at 60°C. TOC and TN concentrations and stable isotope signatures ($\delta^{13}C$ and $\delta^{15}N$) were measured with an isotope-ratio mass

spectrometer (Delta Plus Advantage, Thermo Electron, Bremen, Germany) coupled with an elemental analyzer (Flash EA 1112; Thermo Electron, Bremen, Germany). Stable isotope ratios are expressed in δ notation as the deviation from standards in parts per thousand (‰) according to the following equation:

$$\delta^{13}C,\ \delta^{15}N = [R_{sample} / R_{standard} - 1] \times 10^3$$

where R is $^{13}C/^{12}C$ or $^{15}N/^{14}N$. PeeDee Belemnite and atmospheric nitrogen were used as the isotope standards of carbon and nitrogen, respectively. The analytical precision of the Delta Plus Advantage mass spectrometer system, based on the standard deviation of the internal reference replicates, was <0.2‰ for both $\delta^{13}C$ and $\delta^{15}N$.

Data analyses

To estimate biological and/or physicochemical reduction or addition of carbon in the water column, I calculated the difference between the observed concentration of an element (X) and its concentration predicted by conservative mixing (X_{mix}) as ΔX at each lagoon station: $\Delta X = X - X_{mix}$. The ΔX concentrations were determined for DIC, DOC, POC, and total carbon (TC = DIC + DOC + POC). Predicted conservative concentrations (X_{mix}) were estimated using a linear salinity mixing model with two end members. The terrestrial end member was defined as the average concentration in the three rivers weighted by the discharge of the rivers (Furen River: 21.0 $m^3\ s^{-1}$; Yausubetsu River: 21.0 $m^3\ s^{-1}$; Pon-Yausubetsu River: 0.7 $m^3\ s^{-1}$). The concentrations in the bottom water at the lagoon mouth, station L18 with the highest salinity, were used as the marine end member.

The Bayesian isotopic modeling package, Stable Isotope Analysis in R (SIAR) (Parnell et al., 2010), was used to partition the proportional contributions of potential OM sources to the bulk POM and sedimentary OM based on their N/C, $\delta^{13}C$, and $\delta^{15}N$ signatures. I chose N/C

rather than C/N ratios in the model because the former were statistically more robust; the higher number (TOC concentration) is the denominator and behaves linearly in end-member mixtures (Goñi et al., 2003; Perdue and Koprivnjak, 2007). The SIAR model works by determining probability distributions of the sources that contribute to the observed mixed signal while accounting for the uncertainty in the signatures of the sources and isotopic fractionation. I assumed an isotopic fractionation of 0 and ran the model through 1×10^6 iterations. For each potential source, I report the median and the 95% credible interval (CI) of the estimate of the proportional contribution of each source to the observed value.

I defined four sources (terrestrial OM, coastal OM, lagoon OM, and phytobenthos-derived OM) as end members for the isotopic and elemental mixing model. To estimate the OM components in sediments, I pooled coastal OM and lagoon OM as phytoplankton-derived OM (PhytoOM). The signature values of terrestrial OM (TerrOM) were determined as the average values of samples taken at the three river mouths (salinity = 0). The values in the bottom layer at the lagoon mouth station (L18) with the highest salinity were used as the signature values of coastal OM (CoastOM). Lagoon OM (LagOM) was defined as autochthonous phytoplankton growing in the brackish area of the lagoon. Because the C/N ratio of fresh phytoplankton is close to 7.0 on a molar basis (Redfield et al., 1963) and a low POC/chl. *a* ratio (<100 on a mass basis) is characteristic of living microalgae (Zeitzschel, 1970; Maksymowska et al., 2000), LagOM from samples collected in the brackish area (salinity range: 5–25), which was characterized by a low POC/chl. *a* ratio (<50) and low C/N ratio (<7.0), was considered to be representative of phytoplankton. Phytobenthos-derived OM (BenthOM) was defined as a mixture of the dominant seagrass (*Z. marina*) and the epiphyte. The signature values for BenthOM were calculated using a linear interpolation between the values characteristic of seagrass (seagrass; 100%) and of epiphytes (seagrass; 0%). The total range of

the calculated signature values revealed that the mixing ratio had only about a 5% effect on the estimation. I therefore determined the BenthOM to be a mixture of 50% seagrass and 50% epiphyte. Because the N/C ratio generally declines while OM is decomposing (Van Mooy et al., 2002), it should be noted that the contribution of OM with a high N/C ratio (i.e., LagOM and CoastOM; Appendix Table S5-1) to POM and sedimentary OM was probably underestimated. In contrast, isotopic fractionation does not occur during the decomposition of organic compounds with a high molecular weight (Fry, 2006).

Results

Characteristics of organic matter in the water column

Concentrations of POM (POC, PN) were higher than predicted by conservative mixing, with the highest values around a salinity of 20 in the lagoon (Fig. 5-2a,b). The distribution of POM concentrations corresponded approximately to the distribution of chl. *a* concentration (Fig. 5-2f). The POC/PN ratio was lower than predicted by the conservative mixing, and there were several high values in the river mouths (Fig. 5-2c). $\delta^{13}C_{POC}$ plotted along the predicted conservative mixing line, but the $\delta^{15}N_{PN}$ values were above the predicted line at many stations (Fig. 5-2d,e).

DOC and DON concentrations were higher than predicted by the conservative mixing, and the differences were large in the salinity range 5–25 (Fig. 5-3a,b). The DOC/DON ratios were lower than predicted by the conservative mixing (Fig. 5-3c). Although $a_{CDOM(375)}$ values plotted along the conservative mixing line, $a_{CDOM(254)}$ values were higher than predicted by the conservative mixing (Fig. 5-3d,e). SUVA254 values plotted along the conservative mixing line (Fig. 5-3f). $S_{275–295}$ values were higher than predicted by the conservative mixing, and the highest vales occurred at high salinity (Fig. 5-3g).

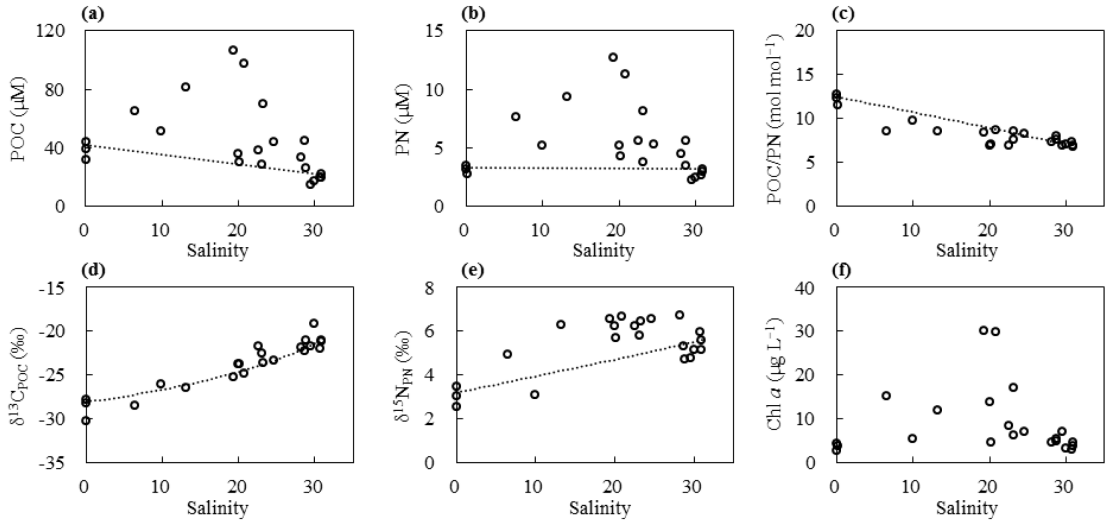

Fig. 5-2. Variations in concentrations of (**a**) POC and (**b**) PN, (**c**) molar POC/PN ratio, (**d**) $\delta^{13}C_{POC}$, (**e**) $\delta^{15}N_{PN}$, and (**f**) chl *a* concentration along the salinity gradient in the Furen Lagoon. Dashed lines indicate the predicted conservative mixing relationships.

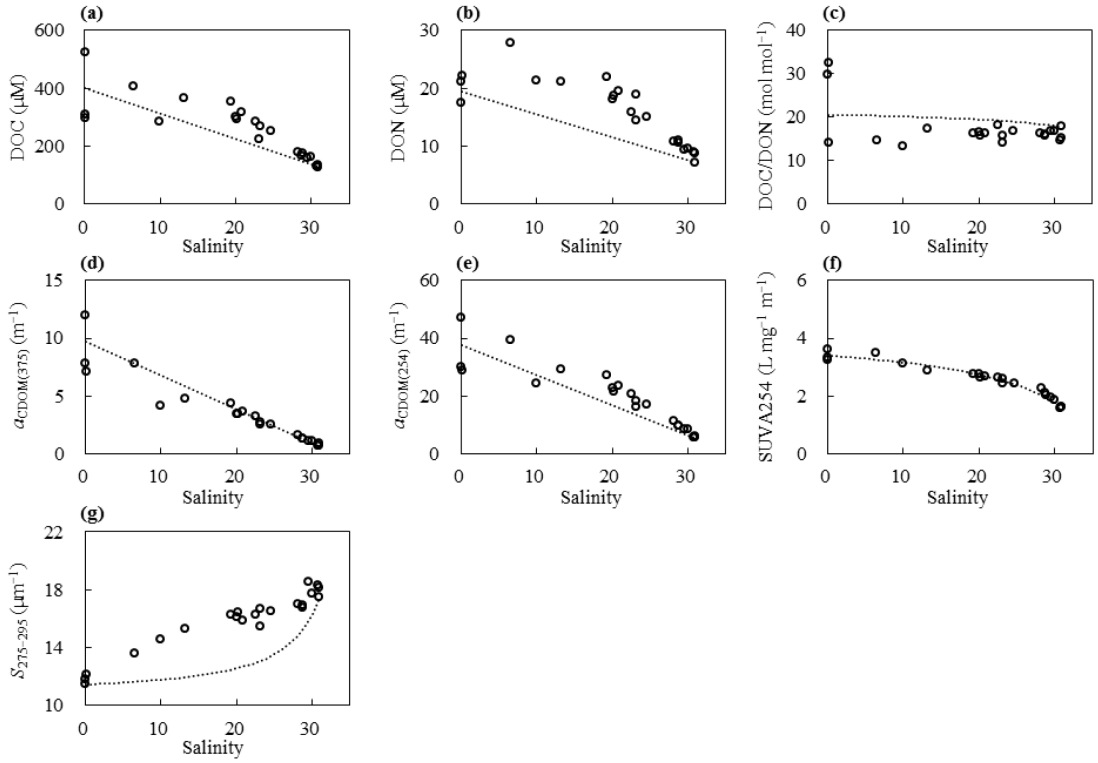

Fig. 5-3. Variations in concentrations of (**a**) DOC and (**b**) DON, (c) molar DOC/DON ratio, (**d**) $a_{CDOM(375)}$, (**e**) $a_{CDOM(254)}$, (**f**), SUVA254 and (**g**) $S_{275–295}$ along the salinity gradient in the Furen Lagoon. Dashed lines indicate the predicted conservative mixing relationships.

Composition of particulate organic matter

The isotopic and elemental mixing model (Fig. 5-4a,b, Appendix Table S5-1) showed that each OM source made a different contribution to water column POM along the salinity gradient (Fig. 5-5a–d). The relative contribution of TerrOM to POM was high (median value: 89%) at the river mouths and low (<10%) around the lagoon mouth (Fig. 5-5a). LagOM was the largest source of POM in the lagoon (~83%) in the salinity range 15–25 (Fig. 5-5b). The relative contribution of CoastOM to POM was high (~92%) around the lagoon mouth and low (<5%) in low-salinity areas (Fig. 5-5c). The relative contribution of BenthOM was low (~19%) in the lagoon, with the highest contribution (~20%) around a salinity of 20 (Fig. 5-5d).

I calculated the concentrations of water column POC derived from each source along the salinity gradient (Fig. 5-6a–d) by multiplying the relative contribution of each source (Fig. 5-5a–d) by the bulk POC concentration (Fig. 5-2a). The terrestrial POC (TerrPOC) concentration was relatively high (median value: 39.1 μmol-C L^{-1}) at the river mouths and low (0.2 μmol-C L^{-1}) around the lagoon mouth (Fig. 5-6a). The lagoon POC (LagPOC) concentration was high in the salinity range 15–25, and the maximum median concentration was 69.6 μmol-C L^{-1} at station L5 (Fig. 5-6b). The ranges of salinity associated with the highest concentrations were similar for chl. *a* and LagPOC (Figs. 5-6b and 5-2f). Coastal POC (CoastPOC) and Phytobenthos-derived POC (BenthPOC) concentrations were relatively low in the lagoon (Fig. 5-6c,d). The maximum median concentration of CoastPOC was 18.5 μmol-C L^{-1} at station L18. The BenthPOC concentration was the highest (median value: 17.3 μmol-C L^{-1}) at station L5.

Composition of sedimentary organic matter

The isotopic and elemental mixing model (Fig. 5-4a,b, Appendix Table S5-1) showed that

each OM source made a different contribution to sedimentary OM along the salinity gradient (Fig. 5-7a–c). TerrOM made the greatest contribution to OM (49–78%) in the lagoon sediments but contributed only 10% to the sedimentary OM at the coastal station (Fig. 5-7a). The relative contribution of TerrOM was high near the river mouths, where the annual mean salinity at station L7, for example, was 15. PhytoOM was a minor component (3–29%) of the OM in the lagoon sediments (Fig. 5-7b). The relative contributions of PhytoOM were high at the lagoon mouth (station L17) and the coastal station. BenthOM was the second largest OM pool in the lagoon sediments (19–36%; Fig. 5-7c). The relative contribution of BenthOM was the lowest (17%) at the coastal station and highest in low-salinity areas, where the annual mean salinity at station L8, for example, was 13.

Carbon budget in the water column

ΔTC, ΔDIC, ΔDOC, and ΔPOC values were positive at salinities less than 15 (Fig. 5-8a,b). At salinities greater than 15, a decrease in DIC corresponded to an increase of C_{org} (e.g., ΔTC near 0; Fig. 5-8a,b). The surface-water fCO_2 values were high (~7332 μatm) at salinities less than 15 and were close to atmospheric values at salinities >20 (Fig. 5-8c). Surface water fCO_2 values at several stations, where salinity was >15, were actually lower than the atmosphere value of 397 μatm (Fig. 5-8c).

Discussion

Selective carbon storage in sediments

To our best knowledge, this study first revealed that the efficiency of C_{org} storage in sediments is dependent on C_{org} derived from multiple sources (Fig. 5-9c,d). The fact that terrestrial C_{org} and phytobenthos-derived C_{org} were more efficiently stored than

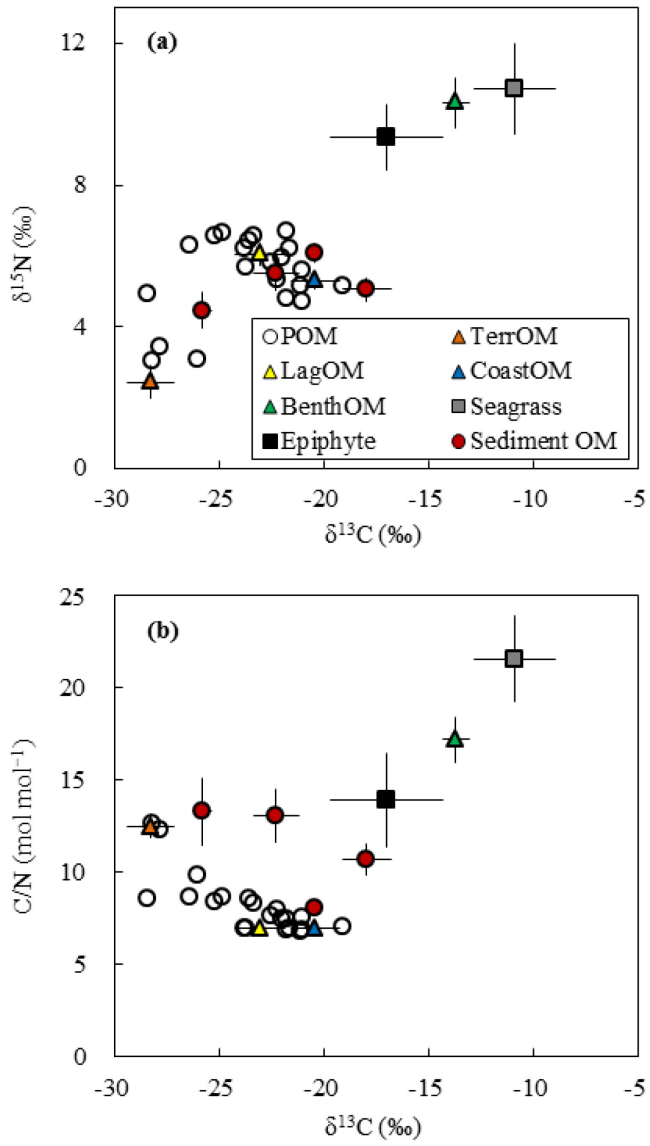

Fig. 5-4. Isotopic and elemental signatures of OM sources, POM, and sedimentary OM sampled in the Furen Lagoon. Error bars show standard deviations of each source.

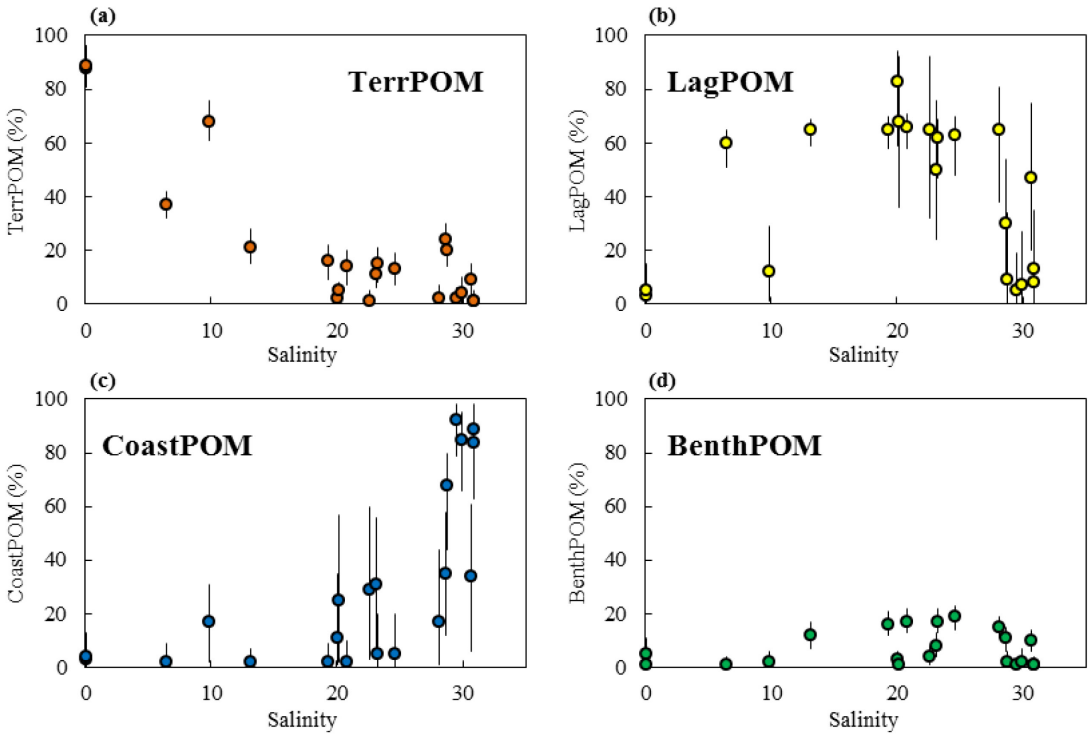

Fig. 5-5. Variations in the relative contributions of different POM sources to water column POM along the salinity gradient. Each plot indicates the median estimated value; error bars show the 95% CIs of the estimated values.

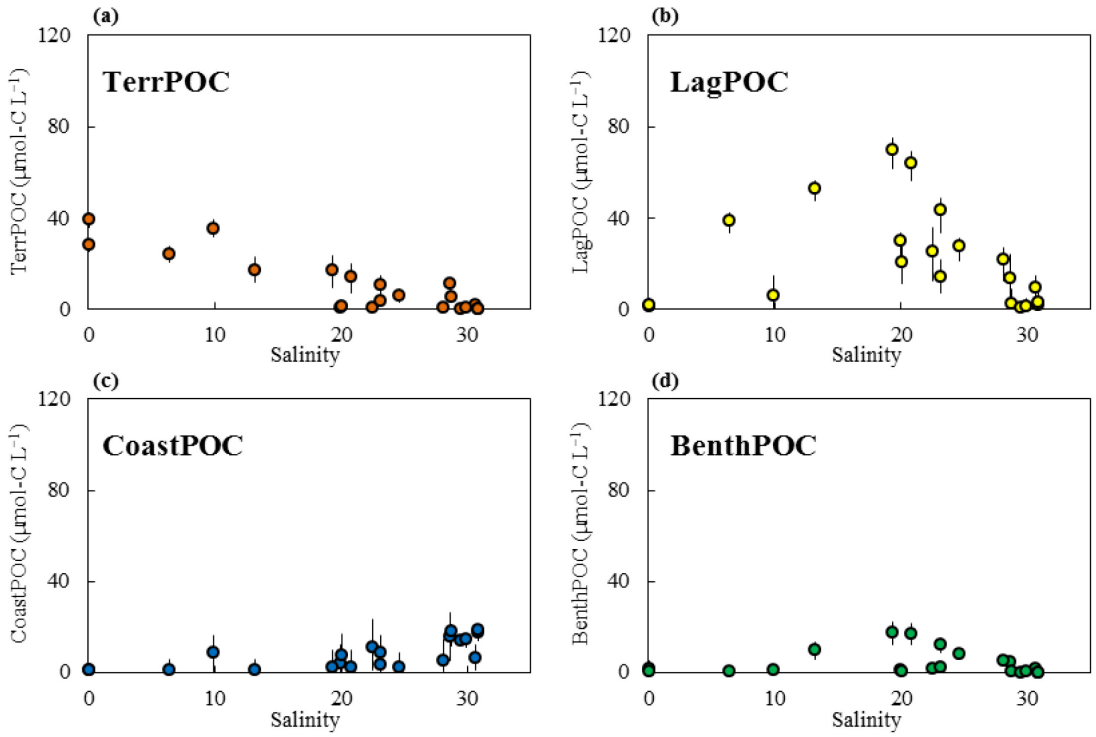

Fig. 5-6. Variations in the calculated carbon concentrations of POC sources along the salinity gradient. The concentrations were calculated by multiplying the relative contribution of each source by the bulk POC concentration. Each plot indicates the median estimated value; error bars show the 95% CIs of the estimated values.

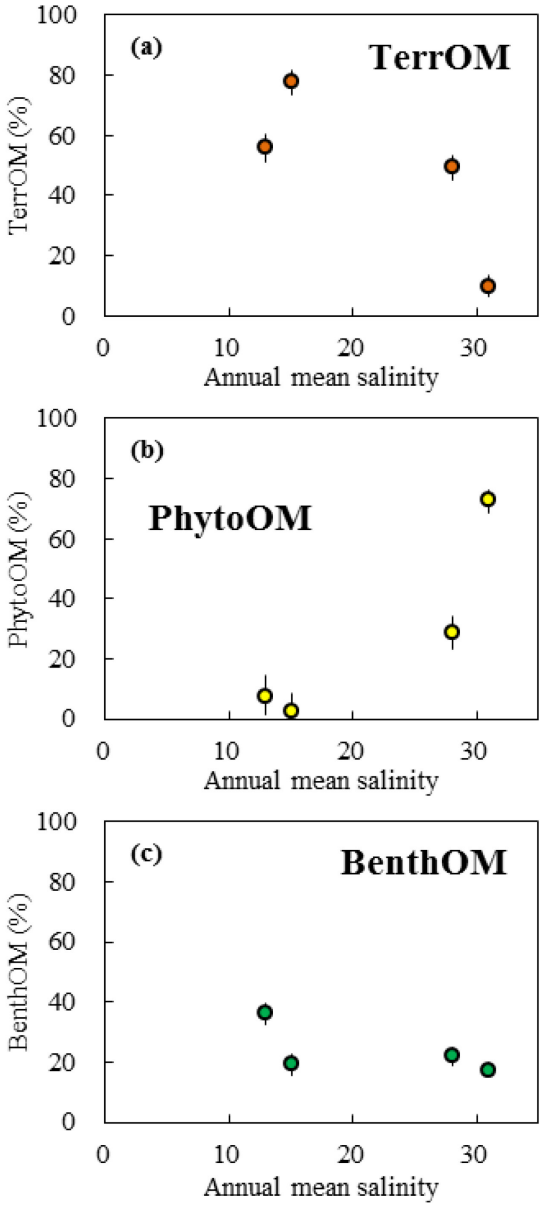

Fig. 5-7. Variations in the relative contributions of different OM sources to sedimentary OM along the salinity gradient. Each plot indicates the median estimated value; error bars show the 95% CIs of the estimated values.

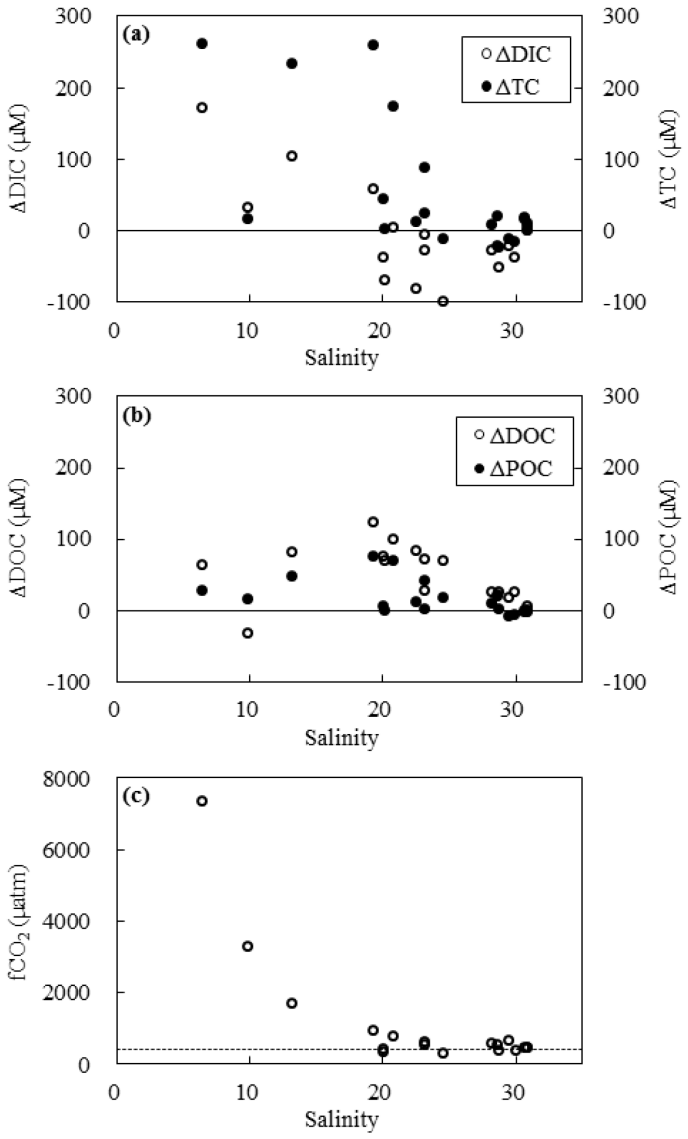

Fig. 5-8. Variations of (a) ΔDIC, ΔTC, (b) ΔDOC, ΔPOC, and (c) fCO_2, along the salinity gradient in the Furen Lagoon. Dashed lines indicate the fCO_2 of the atmosphere (Tokoro *et al.*, 2014).

phytoplankton-derived C_{org} in seagrass meadow sediments suggests that the variability of the composition of C_{org} affects the carbon burial rate.

PhytoOM, derived mainly from autochthonous production, was dominant in the water column POM pool (~95%; Figs. 5-5b,c and 5-9b,c), as has been found in other shallow coastal systems worldwide (Sato et al., 2006; Harmelin-Vivien et al., 2010; Dubois et al., 2012; Savoye et al., 2012; Guerra et al., 2013). Because the composition of POM in the water column fluctuates seasonally, our estimation from a single survey is subject to considerable uncertainty. However, I believe that PhytoOM is the primary component of the water column POM throughout the year, because the chl. *a* concentration during this study (mean value: 10 μg L^{-1}; Fig. 5-2f) was lower than the annual mean value (14 μg L^{-1}; Montani et al., 2011). In addition, the POC/PN ratio in this study (mean value: 7.7 mol mol^{-1}; Fig. 5-2c) was lower than TerrOM (12.5 mol mol^{-1}; Appendix Table S5-1) and similar to the annual mean value (7.7 mol mol^{-1}; Montani et al., unpublished data). Thus, our assessment that PhytoOM accounted for ~95% of the POM in the water column is basically conservative. Although differences in sinking rates of POM sources affect carbon accumulation rates in sediments, such differences may be of minor importance in very shallow systems like Furen Lagoon. I thus hypothesize that the carbon accumulation rate reflects the composition (concentration) of water column POM and that PhytoOM accounts for the largest flux of POM into the sediments. However, PhytoOM was a relatively minor component (3–29%), and TerrOM and BenthOM were major components (49–78% and 19–36%, respectively) of the sedimentary OM (Figs. 5-7a–c and 5-9d), that is, TerrOM and BenthOM were more efficiently preserved than PhytoOM in the sediments. The ratios of TerrOM to PhytoOM in the sediments were at least 10 times the analogous ratios in the water column of the lagoon (Fig. 5-9c,d). Because TerrOM is derived from terrestrial plants with hard cell walls, it contains refractory OM such as aliphatic (cutan, cutin, suberan, and suberin) and

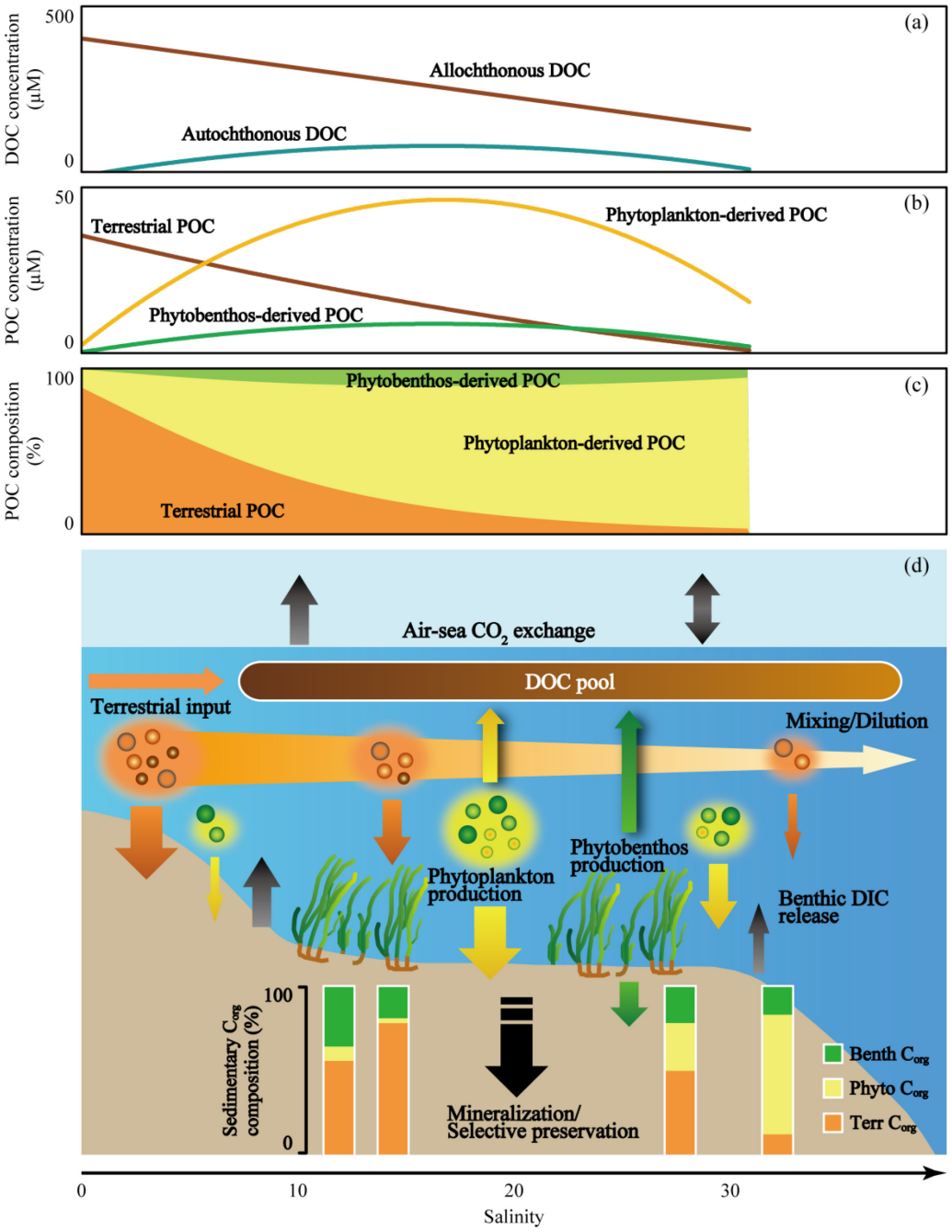

Fig. 5-9. Carbon flow and carbon sequestration processes in shallow coastal ecosystems. Burial of POM into sediments is a major carbon sequestration process. (**b**,**c**) Phytoplankton-derived POM is a more dominant component than terrestrial POM in the water column at moderate salinities (>10; Fig. 5-5), indicating that abundant phytoplankton-derived OM is potentially a major source of sedimentary C_{org}. (**d**) However, terrestrial OM and phytobenthos-derived OM are actually major components of OM in the sediments (Fig. 5-7), indicating that these

components are more refractory than phytoplankton-derived OM and selectively preserved in seagrass meadows. (**a**) Refractory DOM production is another important process. A large fraction of the DOM pool is allochthonous DOM that includes terrestrial and marine origins (Fig. 5-3). Autochthonous DOM is produced by phytoplankton and phytobenthos in seagrass meadows (Fig. 5-3), part of which would have a long residence time in the ocean. (**d**) Autochthonous production also affects air–water CO_2 exchanges (Fig. 5-8). DIC is released from a benthic system especially in the low-salinity zone (~15); thus, this zone would function as a source for atmospheric CO_2. In contrast, active primary production (mainly phytoplankton) converts DIC to C_{org} and reduces the DIC concentration in the high-salinity zone (>15). Because this uptake of DIC exceeds the benthic DIC release, this zone can function as a sink for atmospheric CO_2. Aquatic primary production can contribute a great deal to atmospheric CO_2 uptake on biological timescales. Phytobenthos (mainly seagrass) produces relatively refractory OM, which can be preserved in the ocean on geological timescales. Terrestrial OM is also preserved efficiently in sediments, where it is sequestrated from the atmosphere.

aromatic (lignin, sporopollenin, and dinosporin) cell-wall biopolymers (Zonneveld et al., 2010). In addition, the terrestrial C_{org} transported to the ocean has been reported to be relatively refractory and selectively preserved in marine sediments, because much terrestrial C_{org} is highly degraded during the process of being transported through soils (Hedges et al., 1994; Zonneveld et al., 2010).

The contributions of BenthOM in the lagoon sediments were 0.8–6 times higher than those of PhytoOM (Fig. 5-9d). The efficient storage of BenthOM may be partly explained by the fact that seagrass detritus contains a high proportion of refractory OM such as a lignin, especially detritus derived from rhizomes and roots (Kennedy and Björk, 2009; Kennedy et al., 2010). Like other OM, the flux of BenthOM from the water column to the surface sediment is accounted for by fine particles (<1 mm) derived from plant thalli, because these fine particles are readily resuspended in the water column at our site due to the very shallow, windy conditions. However, it is noteworthy that BenthOM is also supplied from belowground biomass; thus the actual total flux of BenthOM to the sediments may have been underestimated.

Carbon sequestration in the water column

The dynamics of DOC tend to be overlooked, but they can play a key role in the sequestration of carbon in the water columns of shallow coastal ecosystems, because DOC is generally the dominant fraction of the water column C_{org} pool and includes a large proportion of refractory DOC (Nagata, 2008; Jiao et al., 2014). However, the production rates and distribution of refractory DOC in shallow coastal ecosystems are largely unknown (e.g., Wada et al., 2008; Lønborg and Søndergaard, 2009). The release of DOC from seagrass meadows have been reported (Opsahl and Benner, 1993; Barrón and Duarte, 2009); however, using optical analysis, I first showed the possibility of DOC released from seagrass is indeed remained within the

whole system.

The production of autochthonous DOC and the dilution of terrestrial DOC regulate the dynamics of DOC in the water column (Figs. 5-3a and 5-9a). To date, $a_{CDOM(254)}$ values have been used as a metric of the concentration of terrestrial aromatic compounds (Weishaar et al., 2003; Zurbrügg et al., 2013) and as a proxy for potential refractory OM (Saadi et al., 2006; Hur et al., 2009). This study revealed that aromatic compounds have an autochthonous origin at our site (Fig. 5-3e), that is, relatively refractory compounds are produced *in situ* in shallow coastal ecosystems. In a mangrove-dominated estuary located within the Everglades, aromatic DOM is exuded from the mangroves (Bergamaschi et al., 2012). In seagrass meadows, the potential sources of aromatic DOM would be microalgae and seagrasses. Phytoplankton release CDOM with a protein-like fluorescence (Romera-Castillo et al., 2010) that is related to freshly produced aromatic amino acids, such as tyrosine, tryptophan, and phenylalanine (Yamashita et al., 2008). The decrease of DOC/DON ratios and the increase of $S_{275–295}$ values in the lagoon (Fig. 5-3c,g) supports the hypothesis that phytoplankton release labile, protein-rich DOM (Biddanda and Benner, 1997; Fichot and Benner, 2012). In contrast, aquatic vascular plants such as seagrasses contain lignin, which is a refractory biopolymer. The subtropical seagrass *Halodule wrightii* exudes dissolved, lignin-derived phenols as it decomposes (Opsahl and Benner, 1993). Barrón and Duarte (2009) reported that meadows of the Mediterranean seagrass *Posidonia oceanica* release DOC that represents ~71% of the net community production. These findings suggest that seagrasses directly produce refractory DOM that may be preserved in the water column.

The linear decrease with salinity of $a_{CDOM(375)}$, which is also a proxy of potentially terrestrial OM (Astoreca et al., 2009; Para et al., 2013), suggests that conservative mixing of terrestrial DOC with seawater accounted for much of the variability of DOC concentrations in Furen Lagoon (Fig. 5-9a), as has been observed in other estuaries (Chen et al., 2007; Astoreca et

al., 2009).

Air–sea CO_2 exchange

The uptake of DIC in the surface water column by aquatic primary producers stimulates an influx of atmospheric CO_2, although mixing of high-fCO_2 water from land runoff with low-fCO_2 ocean water is the major process that mediates air–sea CO_2 exchange in shallow coastal ecosystems. The low ΔTC values in the high-salinity zone of Furen Lagoon suggest that the benthic release/adsorption of carbon and biological metabolism (photosynthesis and mineralization) were more or less in balance in the water column. Relevant to this point is the fact that C_{org} increases coincided with DIC decreases (Fig. 5-8a,b), indicating that the aquatic primary producers were converting DIC to C_{org} and thereby decreasing the fCO_2 of the water column (Figs. 5-8c and 5-9d). Biological metabolism determines whether a body of water is a sink or a source of atmospheric CO_2 (Maher and Eyre, 2012; Tokoro et al., 2014). Our results show that C_{org} sequestration by aquatic primary producers was directly linked to atmospheric CO_2 uptake in the high-salinity zone of Furen Lagoon, as expected by previous studies (Maher and Eyre, 2012; Tokoro et al., 2014).

In contrast, the positive values of ΔTC in the low-salinity zone suggest that DIC and/or C_{org} were being released from the benthic system (Fig. 5-8a,b). This fact, combined with the general high-fCO_2 of inflowing freshwater (Chen et al., 2012), caused the low-salinity zone to be a source of atmospheric CO_2 (Figs. 5-8c and 5-9d).

How does organic carbon derived from multiple sources contribute to carbon sequestration?

Shallow coastal ecosystems function not only as transition zones between the land and ocean but also as carbon sequestration filters that mitigate atmospheric CO_2 increases, where

planktonic and benthic primary producers sequester C_{org} from atmospheric CO_2 and thereby mitigate atmospheric CO_2 increases (Fig. 5-9d). I found that (1) phytobenthos-derived and terrestrial C_{org} are stored more efficiently than phytoplankton-derived C_{org} in sediments, (2) DOC production by aquatic primary producers sequesters carbon in the water column, and (3) C_{org} sequestration in the water column contributes to the influx of atmospheric CO_2 at biological timescales. These three findings are dependent on the salinity gradient. Our findings reveal that the dynamics of C_{org} derived from multiple sources link with carbon sequestration processes at multiple timescales. This discovery suggests that criteria for evaluating the effectiveness of processes for sequestering carbon should be related to the salinity and C_{org} sources. Finally, our methodology inferring the multiple sources and fates of carbon and the results provide a step toward better understanding coastal carbon dynamics in response to global change, in particular, continued human pressures (Bauer et al., 2013).

Chapter 6:

Depositional environment change and the subsequent habitat relocation affect organic carbon accumulation rates in vegetated coastal ecosystems

Introduction

Vegetated coastal ecosystems (seagrass meadows, saltmarshes, and mangroves) play important roles in global and local carbon budgets (Nellemann et al., 2009). The storage of organic carbon (C_{org}) and the absorption of carbon dioxide are found value in as the functions of these ecosystems in the context of mitigating global climate change, which is called "blue carbon strategies" (Nellemann et al., 2009; McLeod et al., 2011; Pendleton et al., 2012; Duarte et al., 2013; Kelleway et al., 2017b). An increasing number of studies have examined the factors controlling the C_{org} storage function in vegetated coastal habitats (Macreadie et al., 2017). Habitat and species difference (Lavery et al., 2013; Kelleway et al., 2017a), primary productivity and biomass (Serrano et al., 2014; Ferguson et al., 2017; Gullström et al., 2018; Tanaya et al., 2018), habitat scale (Ricart et al., 2015; Miyajima et al., 2017; Oreska et al., 2017; Gullström et al., 2018), and trophic effect (Atwood et al., 2015) affect the efficiency of C_{org} storage into sediment as biological factors. C_{org} storage is also mediated by physicochemical and geological features like the composition of C_{org} source (i.e., the recalcitrance of C_{org}; Trevathan-Tackett et al., 2015; Watanabe and Kuwae, 2015a; Trevathan-Tackett et al., 2017), mineral characteristics (Kelleway et al., 2016; Serrano et al., 2016; Miyajima et al., 2017), oxygen exposure time (Rontani et al., 2014), decomposition time (Maher et al., 2017), hydrodynamic energy (Samper-Villarreal et al., 2016), physical disturbance (Macreadie et al., 2013, 2015; Marbà et al., 2015), nutrient enrichment (Armitage and Fourqurean, 2016; Liu et al., 2017), and sediment loading (Macreadie et al., 2012).

Global, regional, and local changes in the environment (e.g., sea-level rise, climate, anthropogenic disturbance) impact vegetated coastal habitats (Short et al., 2016). In particular, future sea-level rise are predicted to affect the geophysical and biogeochemical characteristics of these ecosystems (Orth et al., 2006; Craft et al., 2009; Lovelock et al., 2015) and to change its C_{org} storage function (McLeod et al., 2011). Sea-level rise would have both positive and negative effects (sediment elevation and erosion) on C_{org} storage in mangroves and saltmarshes (Cahoon et al., 2003; McKee et al., 2007; Mudd et al., 2009). Also, encroachment of mangroves into saltmarshes, which would be partly driven by sea-level rise, increases carbon stocks in the sediment in recent decades (Kelleway et al., 2017a; Pérez et al., 2017). However, its impact on the C_{org} accumulation rates is largely uncertain especially in subtidal habitats.

Historical depositional records can contribute to our understanding of the regulating factors of C_{org} accumulation rates in vegetated coastal ecosystems. In eastern Hokkaido, Japan, analyses of tsunami deposits have revealed recurrent seismic land-level changes that have affected the depositional environment in coastal lagoons (Nanayama et al., 2003; Kelsey et al., 2006; Sawai et al., 2009). Dense seagrass meadows cover the subtidal zones of these lagoons, and saltmarshes surround their shores (Tokoro et al., 2014; Watanabe and Kuwae, 2015a). The sediment cores of these coastal lagoons may thus preserve the history of changes in depositional environments, habitats, and C_{org} accumulation rates on millennial timescales.

Here, I examined the sediment profiles of geological and biogeochemical features in two coastal lagoons in eastern Hokkaido, aiming to investigate how the changes in relative sea-level (RSL), depositional environment, and habitats affect C_{org} accumulation rates in vegetated coastal ecosystems. Age-depth modelling at multiple timescales and geological and biogeochemical approaches were used to reconstruct changes of the depositional environments

over decadal and millennial timeframes. To study habitat relocations, I used isotopic and elemental signatures to infer historical changes in the sources of sedimentary C_{org}.

Materials and methods

Study sites and sample collection

This study was conducted at Furen Lagoon (43°19′46.5″N, 145°15′27.8″E; surface area, 57.4 km^2) and Hichirippu Lagoon (43°2′44.3″N, 145°0′43.2″E; surface area, 3.56 km^2) in eastern Hokkaido, Japan (Fig. 6-1). Both of these lagoons are semi-enclosed systems in the boreal climate region. Silicate and aluminosilicate are the dominant minerals in the sediment of these sites. They have abundant seagrass meadows and are adjacent to surrounding saltmarshes. Because the amount of freshwater input is considerably different between these lagoons, the effect of carbon loads from land could be easily measured.

Furen Lagoon is brackish (salinity, 1–30; Tokoro et al., 2014; Tsuji and Montani, 2017), and the northern part of the lagoon receives freshwater input from the Furen, Yausubetsu, and Pon-Yausubetsu rivers (Fig. 6-1). The lagoon is connected to the Sea of Okhotsk. Most of the area is shallow (about 1-m depth), and *Zostera marina* meadows cover approximately 70% of the total area (Tokoro et al., 2014; Watanabe and Kuwae, 2015a; Magni et al., 2017). Three sampling sites (F8, F41, and F25) were chosen inside the *Z. marina* meadow. The topographic features of F8, F41, and F25 are the inner lagoon, the river mouth, and the lagoon mouth, respectively (Fig. 6-1).

The salinity of Hichirippu Lagoon is relatively high (salinity, 27.5–34.1; Komorita et al., 2014) and the lagoon is connected via a narrow channel to the northwestern Pacific Ocean (Fig. 6-1). The lagoon is shallow (about 0.7-m depth), and thick seagrass meadows (mainly *Z. japonica*) cover the bottom. Three sampling sites (H7, H12, and H15) were chosen in the

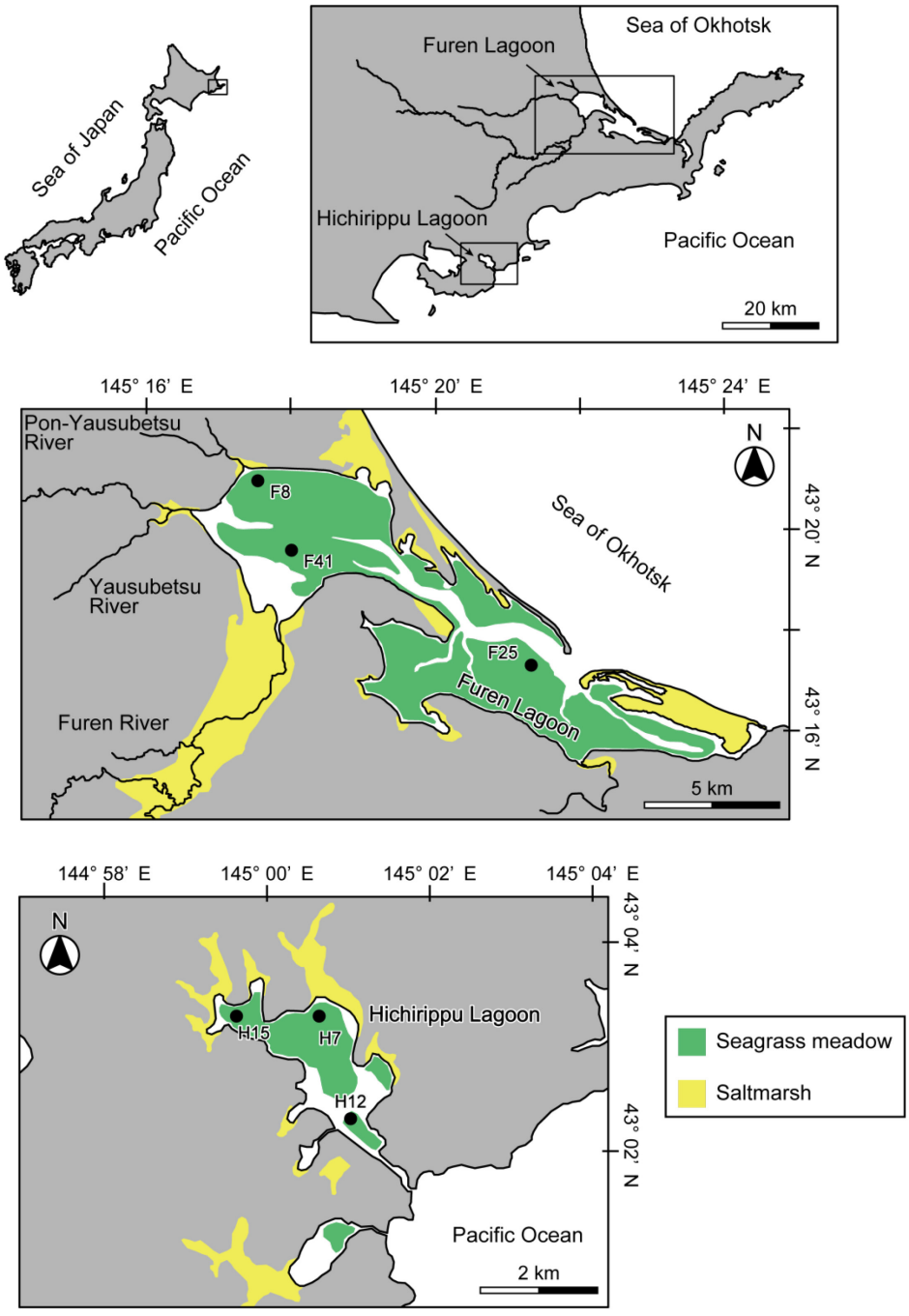

Fig. 6-1. Maps of Furen and Hichirippu lagoons showing the locations of sampling sites. Green and yellow colors represent areas that were occupied by seagrass meadows and saltmarshes, respectively.

subtidal zone within the *Zostera* meadow. H15 and H7 were located in the inner lagoon, and H12 was located close to the tidal channel.

Six long sediment cores (2-m length) were collected in October 2012 from seagrass meadows in Furen Lagoon (3 sites) and Hichirippu Lagoon (3 sites) using a hand-operated knocking corer equipped with a PVC pipe (Adachi et al., 2010) or a hand-operated piston corer. All long cores were sealed at both ends and transported to the laboratory, where they were immediately processed. The compression of cores (defined as the sampled core length divided by the sub-seafloor penetration of the tube) was usually ≥80%, except for the 0–1 m intervals of F8 (79%), F41 (77%), and F25 (69%), and the 1–2 m interval of H15 (78%). I corrected the thickness of each sectioned sample by assuming a linear sediment compression along the core depth during sampling.

Surface sediment cores (in triplicate per site) were also collected using an acrylic piston corer from the same sites. The top 2-mm sections of the collected surface cores were immediately cut and used to estimate the reservoir effect. The top section was packed into a polyethylene bag and transported to the laboratory at −20°C.

Sample procedures and analyses

After transport to the laboratory, magnetic susceptibility was measured using a Multisensor Core Logger (MSCL-S, GeoTek Ltd., Daventry, UK) to determine the magnetic mineral concentration of long cores. The core samples were sliced into 1-cm (the 0–1 m interval) or 2-cm sections (the 1–2 m interval). Each sliced sample was kept frozen at −20°C before further analyses.

The sediment grain size of bulk samples was analyzed using a laser-diffraction/scattering particle size analyzer (LA-960, HORIBA Ltd., Kyoto, Japan). The sediment samples taken from

peaty layers were pretreated with 10% hydrogen peroxide to remove organic matter. Sediments were classified as gravel and coarse sand (>500 μm), medium and fine sand (<500 and >63μm), and mud (silt and clay, <63μm).

Samples were prepared by drying sediments (60°C for 24 hours) and measured for net water loss (i.e., water content). The dried sediments were homogenized and stored for analyses of the concentration and stable isotope ratio of organic carbon (C_{org}) and nitrogen (TN), dating, and estimation of the dry bulk density (DBD).

Before measurements of the concentrations of C_{org} and TN and the stable carbon isotope ratio, the dried sediment was washed with a 1 N HCl solution and dried again at 60°C to remove inorganic carbon. C_{org} and TN concentrations and stable carbon isotope ratios were simultaneously measured with an elemental analyzer-isotope ratio mass spectrometer (Flash EA 1112/Conflo III/DELTA Plus Advantage, ThermoFisher Scientific, Inc., Bremen, Germany). The stable isotope ratio was expressed in conventional δ notation ($\delta^{13}C$) as the deviation from reference materials in parts per thousand (‰). PeeDee Belemnite was used as the reference materials of carbon. The analytical precision of the system, based on the standard deviation of multiple reference replicates (L-Histidine [δ^{13}C-PDB = −10.18‰; Shoko Co., Ltd., Minato-ku, Tokyo]; L-Alanine [δ^{13}C-VPDB = −19.6‰; Shoko Science Co., Ltd., Yokohama, Kanagawa]), was normally within ±2% for the concentrations of Corg and TN and ±0.2‰ for $\delta^{13}C$.

^{210}Pb and ^{14}C dating

Sediment accretion rates (SARs) were determined from ^{210}Pb profiles for recent sediments (<100 yr BP) and with radiocarbon (^{14}C) dating for older sediments. Total ^{210}Pb concentrations of dried sediments were analyzed by gamma spectrometry using high-purity germanium well detectors (GCW3523, Canberra, Connecticut, USA) with a low-background-noise lead chamber

(777B, Canberra). The concentrations were determined from the 46.5 keV peak by counting for more than 24 hours. Detector efficiencies for this geometry were calculated using a natural sediment standard (IAEA-375). Supported ^{210}Pb ($^{210}Pb_{sup}$) at each core was estimated as the average ^{210}Pb concentration of the deeper sections where ^{210}Pb reached constant concentrations. Excess ^{210}Pb ($^{210}Pb_{ex}$) concentrations were calculated by subtracting the $^{210}Pb_{sup}$ from the total ^{210}Pb. The date of each section was determined from a constant-rate-of-supply (CSR) model based on the $^{210}Pb_{ex}$ inventory (Appleby and Oldfield, 1978).

For ^{14}C dating, more than 12 sections from each long sediment core and the top 2-mm sections of the surface cores were analyzed. The bulk dried sediments were treated to remove inorganic carbon (i.e., acid washed) and plant debris, and the remaining C_{org} was combusted in an elemental analyzer (either a Euro EA3000, EuroVector, Milan, Italy; or a Flash 2000, Thermo Fisher Scientific, Inc., Waltham, Massachusetts, USA). The evolved CO_2 was collected cryogenically, purified in a vacuum line, and reduced to graphite using hydrogen and an iron catalyst at 650°C for 10 h. Then, the ^{13}C and ^{14}C abundances were determined using accelerator mass spectrometry (AMS). The conventional radiocarbon age was converted into a calendar date in years before present (Cal yr BP; present taken as AD 2012) using the OxCal 4.3 (IntCal13 dataset, Reimer et al., 2013). I estimated the marine reservoir effect (ΔR) as the average date of the top 2-mm sections of each site because the composition of C_{org} sources differed among the sites.

Age–depth models for all cores were constructed using the Bayesian age–depth modelling software "Bacon" (Blaauw and Christen, 2011), with ^{210}Pb (CRS model) and ^{14}C dates. The mean age of each sediment slice was estimated from the age–depth models.

C_{org} stock and accumulation rate estimation

C_{org} stocks were determined from the C_{org} concentrations and DBDs. The DBD of a sediment sample was calculated using the water content (w, g g^{-1}) of each sample and the average grain density (d, g cm^{-3}) determined for some representative samples in each core. The value of d was determined using pycnometers with pure water. The average d was 2.48–2.66 g cm^{-3}. The DBDs of the sediment samples were calculated as follows:

$$\text{DBD (g cm}^{-3}) = (1 - 1.023w)/[w + (1 - 1.023w)/d],$$

where the pore water density was assumed to be 1.023 g cm^{-3} (salinity 35 at 25°C). C_{org} density (g C_{org} cm^{-3}) was calculated by using C_{org} concentration and DBD for each sediment slice. The C_{org} stocks (g C_{org} m^{-2}) were estimated by calculating the cumulative mass of C_{org} accumulated over multiple timescales.

Averaged C_{org} accumulation rates for the decadal (<100 years) timescales were calculated from linear regression of the cumulative C_{org} stocks versus the ^{210}Pb dates. Averaged C_{org} accumulation rates for millennial (>1000 years) timescales were calculated from linear regression of the cumulative C_{org} stocks versus the ^{14}C dates (Cal yr BP). C_{org} accumulation rates for each sediment slice were also estimated as the slope of the linear regression between the cumulative C_{org} stocks and the dates of the age–depth model using the three peripheral slices.

C_{org} source mixing model

The Bayesian isotopic modeling package, SIAR (Parnell et al., 2010), was used to partition the contributions of potential sources to the sedimentary C_{org} based on their N/C and δ^{13}C signatures. I chose N/C rather than C/N ratios in the model because the former was statistically more robust (Perdue and Koprivnjak, 2007; Watanabe and Kuwae, 2015a). For each

potential source, I report the median and the 95% confidence interval of the estimate of the proportional contribution of each source.

For the Furen Lagoon model, I defined five potential C_{org} sources, i.e., seagrass, phytoplankton, microphytobenthos (MPB), saltmarsh plants, and riverine particulate organic matter (riverine OM) as endmembers. To suppress the divergence of the estimation results, I pooled phytoplankton and MPB as microalgae, and I also pooled saltmarsh plants and riverine OM as terrestrial organic matter (TerrOM) (Fig. 6-2). For the Hichirippu Lagoon model, seagrass, microalgae, and TerrOM (saltmarsh plants + riparian soil) were considered as potential C_{org} sources (Fig. 6-2).

Seagrass was collected seasonally from several sites located along the salinity gradient in Furen Lagoon (in 2014) and Hichirippu Lagoon (from 2004 to 2008). The individual plant values were determined as the average values of aboveground and belowground parts. Particulate organic carbon samples collected in Furen Lagoon (in 2014) and Hichirippu Lagoon (from 2005 to 2007), which were characterized by low POC/chlorophyll *a* ratios (<100) and low C/N ratios (<8.0), were considered to be representative of phytoplankton (Watanabe and Kuwae, 2015a). Because previous studies have reported that the N/C ratios of terrestrial plants with extremely low N/C ratios changed during decomposition (Krüger et al., 2015), saltmarsh detritus was sampled directly from the peat layers in cores H7 and H15, and then the average value was determined. Riparian soil (top 5 mm) was collected using a 2.9-cm diameter corer in the Hichirippu Lagoon watershed. N/C and $\delta^{13}C$ for sources were analyzed following the method described above.

Riverine OM was determined as the average value of samples taken at the three river mouths (salinity = 0) in Furen Lagoon in 2014 (Watanabe and Kuwae, 2015b). The values of N/C and $\delta^{13}C$ for MPB were taken from values in the literature for Furen Lagoon (Kuwae et al.,

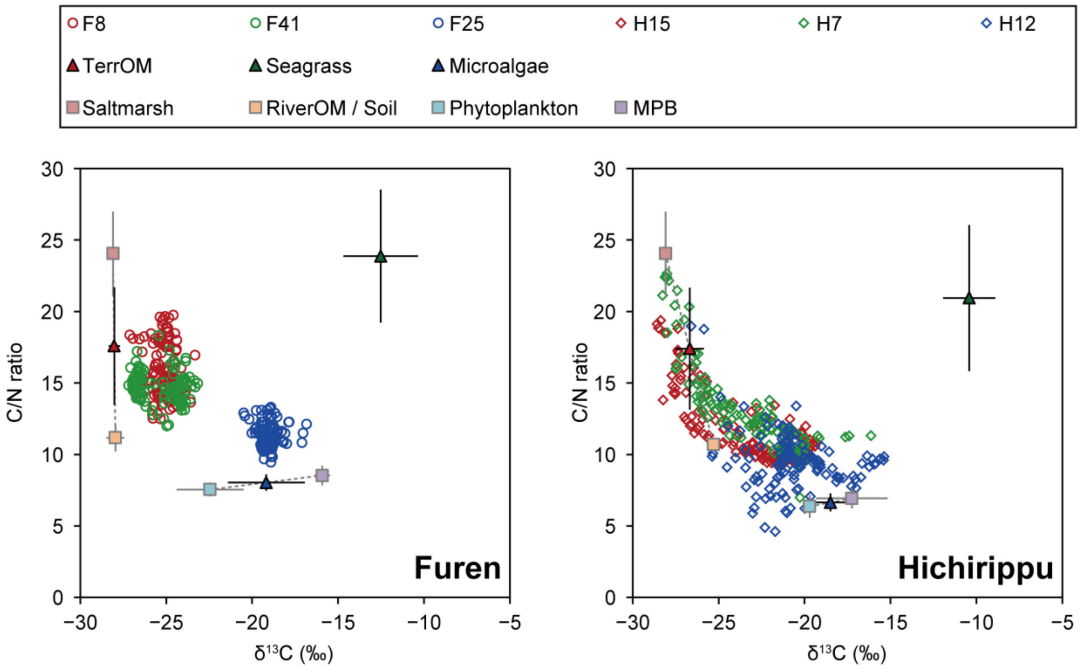

Fig. 6-2. Isotopic and elemental signatures of C_{org} sources and sediment samples in Furen and Hichirippu lagoons. Error bars represent standard deviations of each source.

2012) and Hichirippu Lagoon (Kajihara et al., 2010). Microalgae was defined as a mixture of phytoplankton and MPB, and TerrOM was likewise defined as a mixture of saltmarsh plants and riverine OM/riparian soil. The signature values were computed using a linear interpolation and a mixing ratio that ranged from 0 to 100%.

Because the N/C ratio generally declines while OM is decomposing (Krüger et al., 2015), the contribution from the source with a high-N/C (i.e., microalgae) to sedimentary C_{org} was probably underestimated. In contrast, there is little change of $\delta^{13}C$ during decomposition (Fry, 2006).

Statistical analyses

Statistical analyses were performed using R statistical packages (R Core Team, 2017). I used a generalized linear model with a gamma distribution and identity link to examine the effects of mineral mass accumulation rate (MAR), mud content, and sediment type (peat/subtidal) on C_{org} accumulation rate. The best model was selected according to the Akaike Information Criterion. Mineral density in each sediment sample was calculated with the following equations:

$$\text{Mineral density (g cm}^{-3}) = \text{DBD} \times (1 - \text{organic matter content})$$

Organic matter content was defined as loss on ignition (LOI), the fractional weight loss of dry sediment samples after combustion at 500–550°C. In this study, LOI was estimated from C_{org} concentration using the linear regressions between these parameters (Fourqurean et al., 2012) as follows:

$$\text{LOI (\%)} = [C_{org}\ (\%) + 0.21]/0.4 \qquad (\text{LOI} < 20\%)$$

$$\text{LOI (\%)} = [C_{org}\ (\%) + 0.33]/0.43 \qquad (\text{LOI} \geq 20\%)$$

MAR was estimated as the slope of the linear regression between the cumulative mineral mass and the dates of the age–depth model using the three peripheral slices.

Change point analysis (Killick and Eckley, 2014) was applied to the vertical profiles of the C_{org} accumulation rates to identify the time periods of rapid C_{org} accumulation. Hierarchical clustering analysis was used to classify the depositional environment of the time periods of rapid C_{org} accumulation. I carried out the clustering analysis based on the Euclidean distance and Ward criterion using the C_{org} concentrations, grain-size composition, and C_{org} source composition of the sediment samples identified by the change point analysis. This dataset was also used for principal component analysis.

Results

Age–depth chronology

The $^{210}Pb_{ex}$ concentrations declined from the surface to the horizon of $^{210}Pb_{sup}$ (Fig. 6-3). The SARs at the decadal scale were estimated to be 0.6–4.9 mm yr^{-1} and 0.2–1.9 mm yr^{-1} in Furen Lagoon and Hichirippu Lagoon, respectively (Table 6-1). Based on the ^{14}C dates (Cal yr BP), the averaged SARs at the millennial scale were estimated to be 0.2–1.2 mm yr^{-1} and 0.4–0.6 mm yr^{-1} in Furen Lagoon and Hichirippu Lagoon, respectively (Table 6-1). The decadal-scale SARs were significantly higher than those at the millennial scale except for the cores F41 and H7 (*t* test, $p < 0.01$).

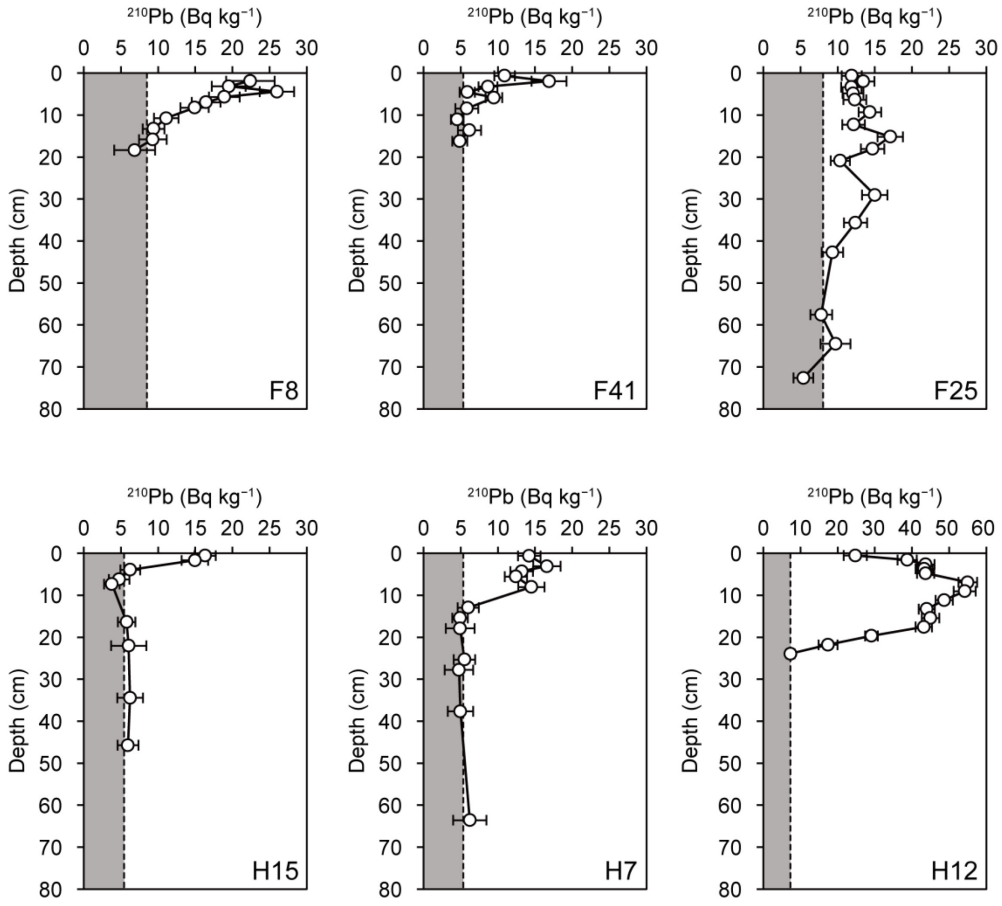

Fig. 6-3. Measured depth profiles of ^{210}Pb concentration (±1σ). The grey shaded area indicates the supported ^{210}Pb ($^{210}Pb_{sup}$) in each core.

Table 6-1 Average sediment accretion rates (SARs) and C_{org} accumulation rates in each site (mean ± 95% confidence interval). Decadal (derived from ^{210}Pb dating) and millennial (derived from ^{14}C dating) rates are estimated.

Site	Contemporary habitat and geomorphological setting	Decadal scale (^{210}Pb)			Millennial scale (^{14}C)		
		Thickness (cm)	SAR (mm yr^{-1})	C_{org} acc. rate (g C_{org} m^{-2} yr^{-1})	Thickness (cm)	SAR (mm yr^{-1})	C_{org} acc. rate (g C_{org} m^{-2} yr^{-1})
Furen Lagoon							
F8	*Zostera marina* Inner lagoon	8	1.0 ± 0.2	11.7 ± 3.5	200	0.2 ± 0.0	2.0 ± 0.4
F41	*Z. marina* River mouth	6	0.6 ± 0.2	7.5 ± 3.1	200	0.6 ± 0.1	5.1 ± 1.0
F25	*Z. marina* Lagoon mouth	30	4.9 ± 1.0	41.6 ± 7.7	200	1.2 ± 0.5	11.8 ± 4.5
Hichirippu Lagoon							
H15	*Z. japonica* Inner lagoon	20	1.9 ± 0.4	31.0 ± 7.0	200	0.6 ± 0.1	14.8 ± 3.8
H7	*Z. japonica* Inner lagoon	2	0.2 ± 0.1	5.1 ± 5.6	200	0.5 ± 0.1	9.2 ± 3.2
H12	*Z. japonica* Edge of tidal channel	6	1.5 ± 0.1	11.7 ± 4.0	200	0.4 ± 0.1	2.7 ± 0.6

Geological and biogeochemical features of sediment cores

The sediment of Furen Lagoon was mainly composed of muddy-sand and sand (Fig. 6-4). In contrast, muddy sediment was dominant in Hichirippu Lagoon except for core H12 located close to the tidal channel (Fig. 6-5). The magnetic susceptibility was considerably higher in Furen Lagoon than Hichirippu Lagoon (Figs. 6-4 and 6-5).

The millennial-scale SAR was the slowest (>8000 Cal yrBP at 200-cm depth) in the core F8 (Fig. 6-4, Table 6-1). Fine sand and mud dominated the sediment but coarse sand layer was found at 10–20 cm depth. C_{org} concentration was more than 2% at the sediment surface, and decreased <1% to the deeper sediments. C/N ratio was ranging from 12 to 20. $\delta^{13}C$ was relatively stable but slightly fluctuated in a range of −23.3‰ to −27.1‰.

The core F41 represented the moderate millennial-scale SAR (4000 Cal yrBP at 200-cm depth) (Fig. 6-4, Table 6-1). C_{org} concentrations were lower than 1.5% almost through the profile, and especially low at coarse sand layer. C/N ratio and $\delta^{13}C$ were in ranges of 12–18 and −23.1‰ to −27.2‰.

Both the decadal- and millennial scale SARs were highest in the core F25 (Fig. 6-4, Table 6-1). The sediment was dominated by fine and medium sand. C_{org} concentration was stable and almost lower than 1%. C/N ratio (9–14) was lower than the other sites in Furen Lagoon. $\delta^{13}C$ ranged from −20.5‰ to −16.8‰, which was the most ^{13}C-enriched sediment in Furen Lagoon sites.

In the core H15, the millennial-scale SAR was moderate (3000 Cal yrBP at 200-cm depth) and the decadal-scale SAR was relatively rapid (Fig. 6-5, Table 6-1). SAR dynamically changed, which was linked with the changes in other biogeochemical signatures. The peaty sediment layer was distributed at 140–175-cm depth (around 2400 Cal yr BP), which represented high C_{org} concentration (~20.3%), high C/N ratio (~20), and ^{13}C-depleted signature (~−28.6‰). The

section at 75–140 cm depth showed the rapid SAR with the increase in $\delta^{13}C$. From 25 cm to 75 cm depth, $\delta^{13}C$ decreased with the slow SAR. The contemporary deposit (~25-cm depth) was accumulated rapidly with the increase in $\delta^{13}C$.

The core H7 represented the moderate millennial-scale SAR (4000 Cal yrBP at 200-cm depth) (Fig. 6-5, Table 6-1). Several sandy layers were deposited inside the dominant muddy sediment. The peaty sediment at 100–120-cm depth was accumulated on the sandy layer, which was high C_{org}, ^{13}C-depleted. The section above the peaty layer (75–100-cm depth) showed the rapid SAR and the increase in $\delta^{13}C$. In the top 75 cm section, C/N ratio and $\delta^{13}C$ fluctuated and the SAR was relatively slow.

Both the decadal- and millennial scale SARs were slow in the core H12 (Fig. 6-5, Table 6-1). The grain size distribution was heterogeneous and the coarse sand layer was distributed in the muddy sand sediment. The $\delta^{13}C$ signature was the highest among the sediments of Hichirippu Lagoon. C_{org} concentration was lower than 1% through the profile. The SAR accelerated around 1900–2200 Cal yr BP at 75–130-cm depth.

Composition of C_{org} sources in sediments

The C_{org} source mixing model showed the temporal and spatial variation in the C_{org} sources in the sediment of the coastal vegetated habitats. In Furen Lagoon, TerrOM was the most dominant source in the cores F8 and F41. The average contributions of TerrOM were 79% (78–81%, 95% confidence interval) and 79% (76–81%) in cores F8 and F41, respectively (Fig. 6-6a,b). In these cores, seagrass and microalgae were less important sources of C_{org} than TerrOM. The average contribution of TerrOM was significantly lower in the F25 sediment (20–24%, 95% CI) than at the inner sites (Fig. 6-6c). Seagrass (29–32%) and microalgae (46–49%) were the dominant components in the F25 sediment (Fig. 6-6c).

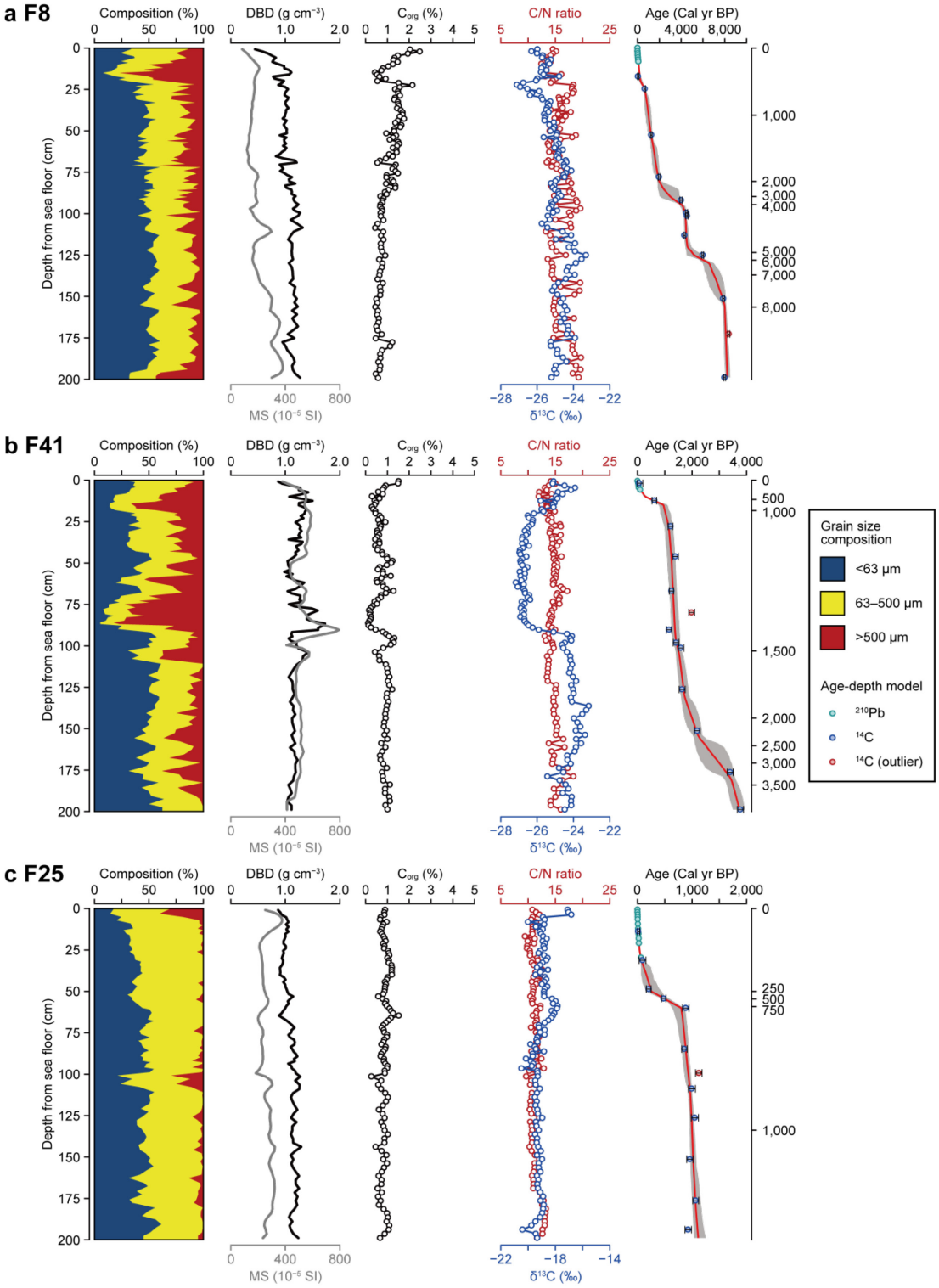

Fig. 6-4. Vertical profiles of grain size composition, dry bulk density (DBD), magnetic susceptibility (MS), organic carbon (C_{org}) concentration, C/N ratio, $\delta^{13}C$, and age–depth model at sampling sites in Furen Lagoon. In the age–depth model, red lines and gray areas represent the weighted mean estimates and 95% confidence intervals.

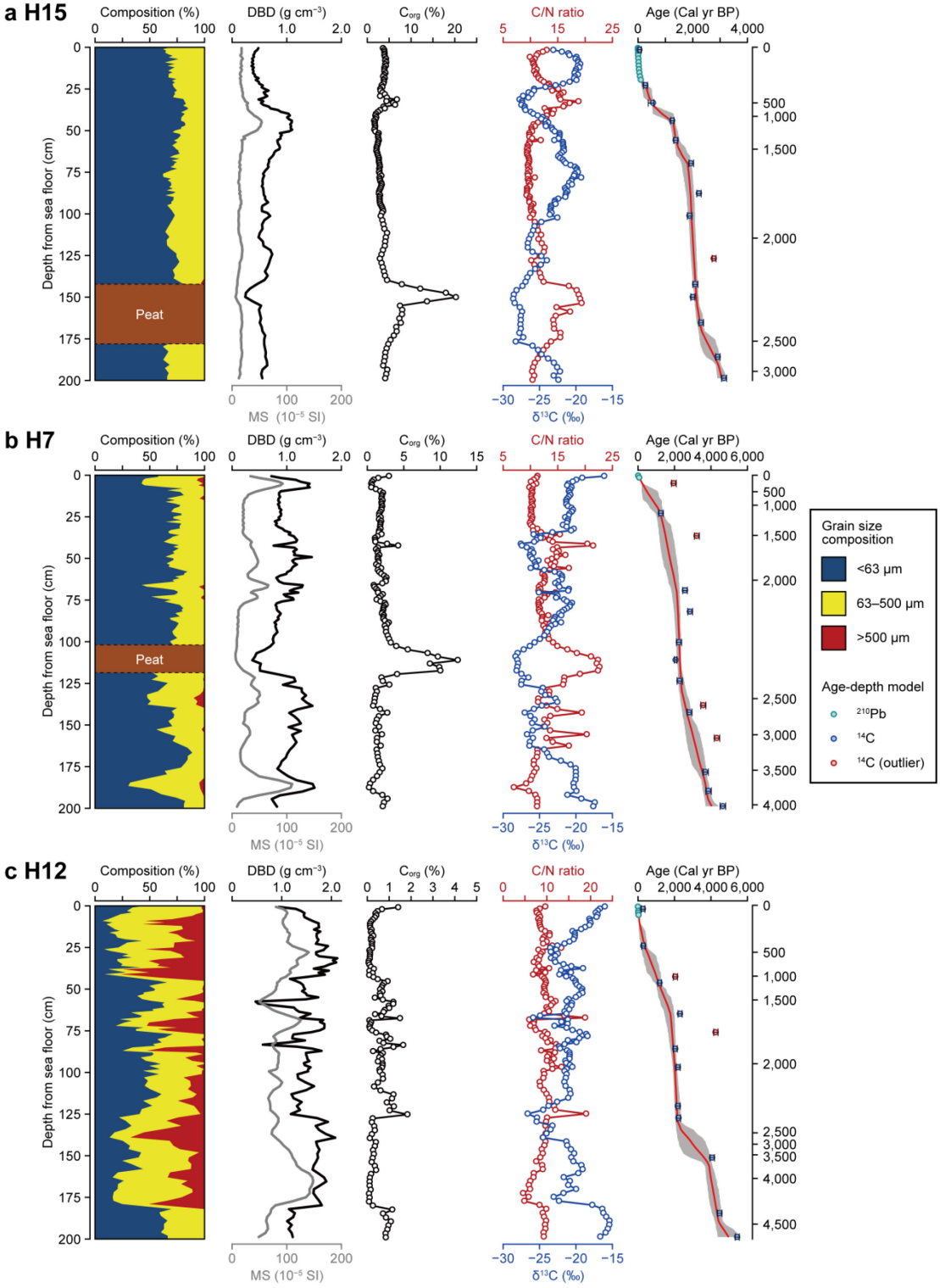

Fig. 6-5. Vertical profiles of grain size composition, dry bulk density (DBD), magnetic susceptibility (MS), organic carbon (C_{org}) concentration, C/N ratio, $\delta^{13}C$, and age–depth model at sampling sites in Hichirippu Lagoon. In the age–depth model, the red lines and gray areas represent the weighted mean estimates and 95% confidence intervals.

The dominant C_{org} sources temporally changed in the sediment cores collected in Hichirippu Lagoon. TerrOM occupied more than 90% and the contributions of seagrass and microalgae were near 0 at the peaty layers in the cores H15 and H7 (Fig. 6-7). The contribution of microalgae and seagrass increased at the upper section of the peaty layers. In the core H12, the peaty layer was not distributed but the contribution of TerrOM was high around 2400 Cal yr BP.

C_{org} stocks and accumulation rates

The top two meter C_{org} stocks of sand-dominant cores (F8, F41, F25, and H12; 19600, 18400, 18600, and 13900 g C_{org} m^{-2}, respectively) were lower than half those of mud-dominant cores (H15 and H7; 48700 and 38400 g C_{org} m^{-2}, respectively). The averaged mud content (< 63 μm) was significantly correlated with the top two-meter C_{org} stocks ($R^2 = 0.95$, $p < 0.001$, N = 6; Fig. 6-8a). The integrated analysis of the six cores showed that mud content (< 63 μm) was significantly correlated with C_{org} concentration ($R^2 = 0.48$, $p < 0.001$, N = 677) but the samples from the peaty layers were plotted out of this regression (Fig. 6-8b).

The decadal-scale C_{org} accumulation rate in the core F25 (41.6 g C_{org} m^{-2} yr^{-1}) was higher than those at the inner sites (F8 and F41, 11.7 and 7.5 g C_{org} m^{-2} yr^{-1}, respectively) in Furen Lagoon (Table 6-1). The highest millennial-scale C_{org} accumulation rate was also found in core F25 (11.8 g C_{org} m^{-2} yr_{-1}). In Hichirippu Lagoon, both the decadal- and millennial-scale C_{org} accumulation rates in core H15 (31.0 and 14.8 g C_{org} m^{-2} yr^{-1}) were higher than those at the other sites in Hichirippu Lagoon, which was comparable to those in the core F25 (Table 6-1). The decadal-scale C_{org} accumulation rates were significantly higher than those at the millennial scale except for the cores F41 and H7 (*t* test, $p < 0.01$). A generalized linear model supported

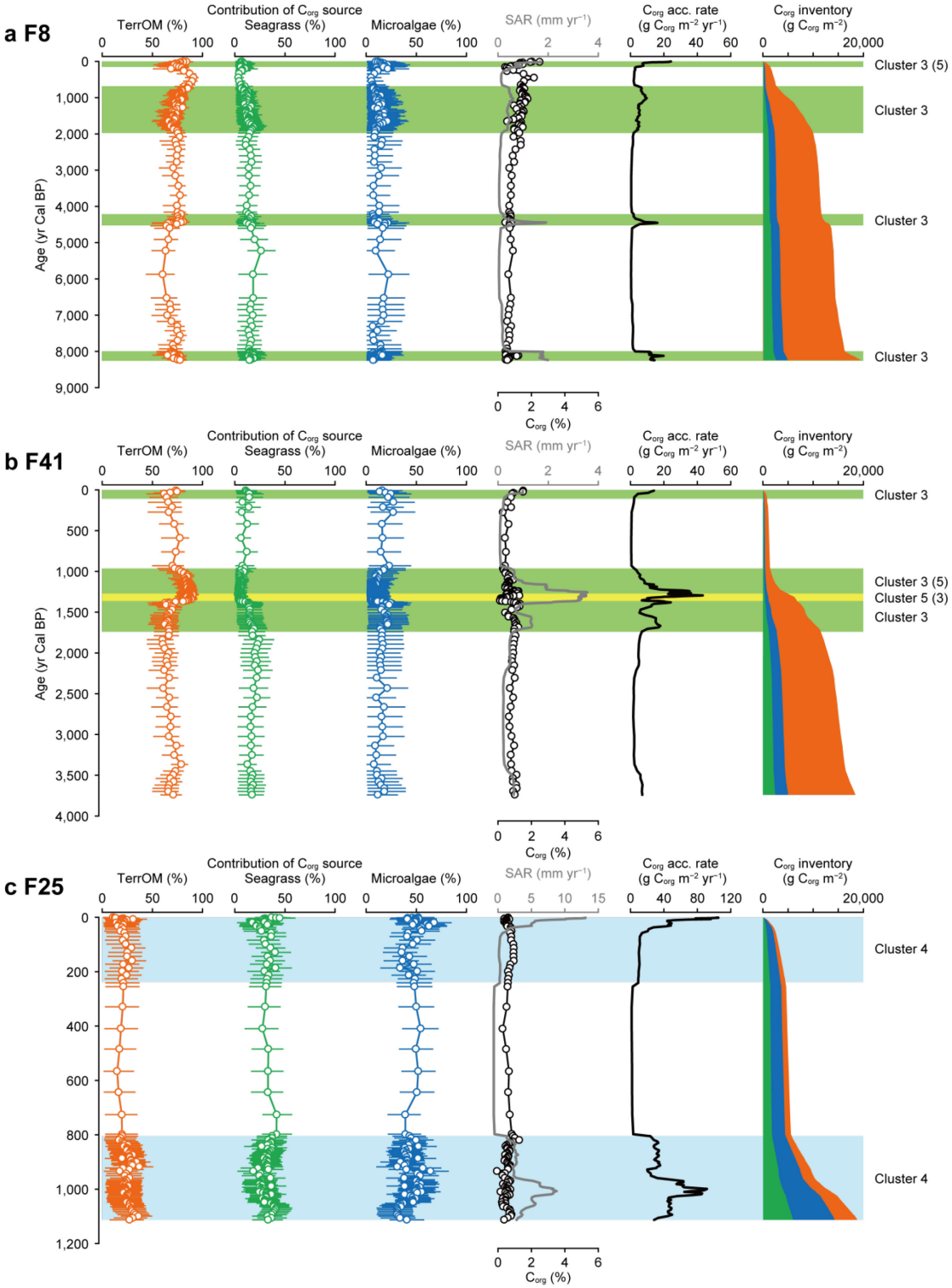

Fig. 6-6. Historical records from Furen Lagoon cores. Temporal changes in the contribution of each organic carbon (C_{org}) source, C_{org} concentration, sediment accretion rate (SAR), C_{org} accumulation rate, and C_{org} inventories in F8 (**a**), F41 (**b**), and F25 (**c**). Color shadings mark the time periods of rapid C_{org} accumulation. These periods were classified with a hierarchical

clustering analysis based on C_{org} concentration, grain-size composition, and C_{org} source composition of the sediment samples. In addition to the major clusters, minor clusters were shown in parentheses. Error bars show the 95% confidence intervals of the estimates.

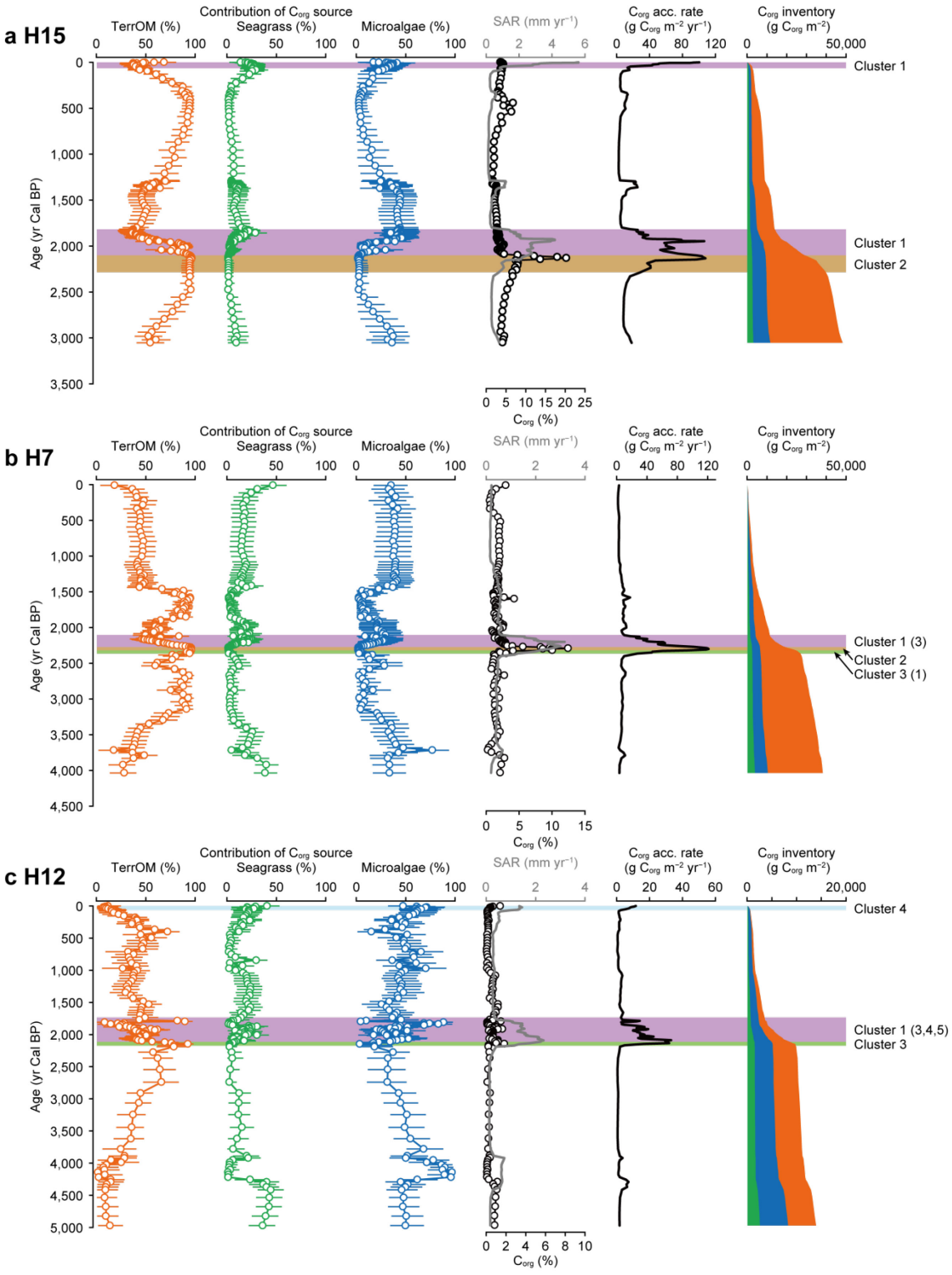

Fig. 6-7. Historical records from Hichirippu Lagoon cores. Temporal changes in the contribution of each organic carbon (C_{org}) source, C_{org} concentration, sediment accretion rate (SAR), C_{org} accumulation rate, and C_{org} inventories in H15 (**a**), H7 (**b**), and H12 (**c**). Color shadings mark the time periods of rapid C_{org} accumulation. These periods were classified with a

hierarchical clustering analysis based on C_{org} concentration, grain-size composition, and C_{org} source composition of the sediment samples. In addition to the major clusters, minor clusters were shown in parentheses. Error bars show the 95% confidence intervals of the estimates.

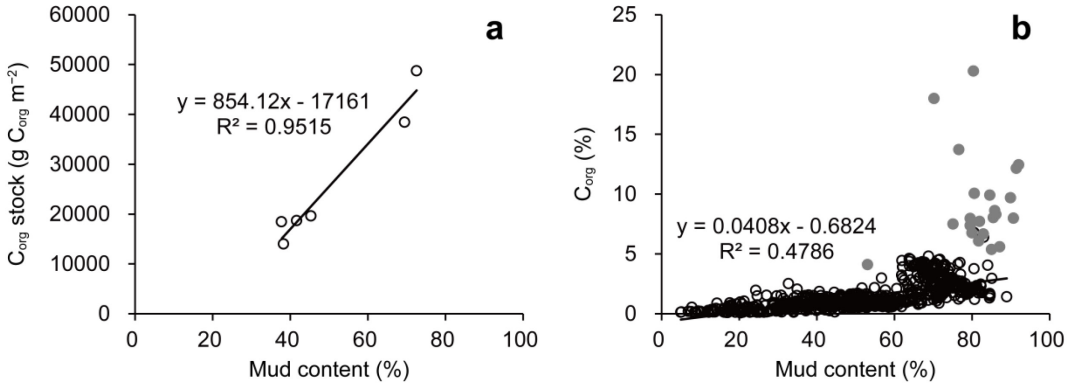

Fig. 6-8. (**a**) The relationship between mean mud (< 63 μm fraction) contents and 2 m C_{org} stocks in six sediment cores. (**b**) The relationship between mud contents and C_{org} concentrations in each sample. Closed gray circles show the samples taken from peaty layers.

that both MARs and mud contents significantly control C_{org} accumulation rates (Fig. 6-9, Table 6-2).

The age–depth model showed that C_{org} accumulation rates had spatial and temporal variations (Figs. 6-6 and 6-7). The sediment samples identified as the time periods of rapid C_{org} accumulation were classified into five clusters (Fig. 6-10). Cluster 1 was classified as the muddy sediment composed of TerrOM, seagrass, and microalgae. Cluster 2 was classified as the peaty sediment with a high C_{org} content. Cluster 3 was the sandy sediment which was dominated by TerrOM. Cluster 4 was the sandy sediment with a high contribution of seagrass and microalgae. Cluster 5 was the sediment containing coarse sand and grain.

In Furen Lagoon, rapid sediment accretion enhanced C_{org} accumulation from and in the last century (Fig. 6-6). At the inner lagoon sites, the average C_{org} accumulation rates around 1800 Cal yr BP to 800 Cal yr BP (F8, 5.8 g C_{org} m^{-2} yr^{-1}; F41, 15.0 g C_{org} m^{-2} yr^{-1}) were higher than the millennial-scale rates (Fig. 6-6, Table 6-1). C_{org} accumulation rates from 1100 Cal yr BP to 800 Cal yr BP (43.9 g C_{org} m^{-2} yr^{-1}) were higher at F25 than at the inner sites (Fig. 6-6). In contrast, C_{org} accumulation was inhibited from 800 Cal yr BP to 200 Cal yr BP in Furen Lagoon (Fig. 6-6).

In Hichirippu Lagoon, C_{org} accumulation rates were enhanced in two types of depositional environments. In H15 and H7, the C_{org} accumulation rates were high in the peaty layers (Cluster 2) which were deposited around 2400 Cal yr BP. Average C_{org} accumulation rates were 59.0 and 117 g C_{org} m^{-2} yr^{-1} in H15 and H7, respectively, during this period (Fig. 6-7). Also, the C_{org} accumulation rates were high from 2400 Cal yr BP to around 1800 Cal yr BP (Cluster 1), with the averages of 56.2, 46.1, and 13.1 g C_{org} m^{-2} yr^{-1} in H15, H7, and H12, respectively (Fig. 6-7). In H15 and H12, the C_{org} accumulation rates in the last century increased markedly (Fig. 6-7).

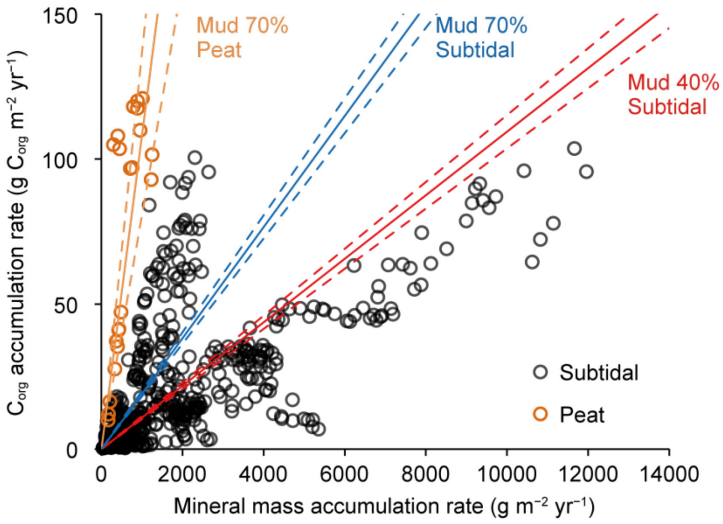

Fig. 6-9. Relationships between organic carbon (C_{org}) accumulation rate, mineral mass accumulation rate, mud (<63 μm) content, and sediment type (peat/subtidal) analyzed with a generalized linear model. The solid and dashed lines indicate the linear models and their 95% confidence intervals, respectively.

Table 6-2 Generalized linear model result for the effect of mineral mass accumulation rate (MAR), mud content, and sediment type (peat/subtidal) on organic carbon (C_{org}) accumulation rate. The best model according to its Akaike information criterion (AIC) value is shown.

	Estimate	SE	*t*	*P* (>*t*)
C_{org} acc. rate ~ MAR × mud × type, family = Gamma, AIC = 4431.5				
Intercept	−0.09279	0.07965	−1.165	0.244
MAR × mud × peat	0.001548	0.0002034	7.61	<0.0001
MAR × mud × subtidal	0.000274	0.000007499	36.537	<0.0001

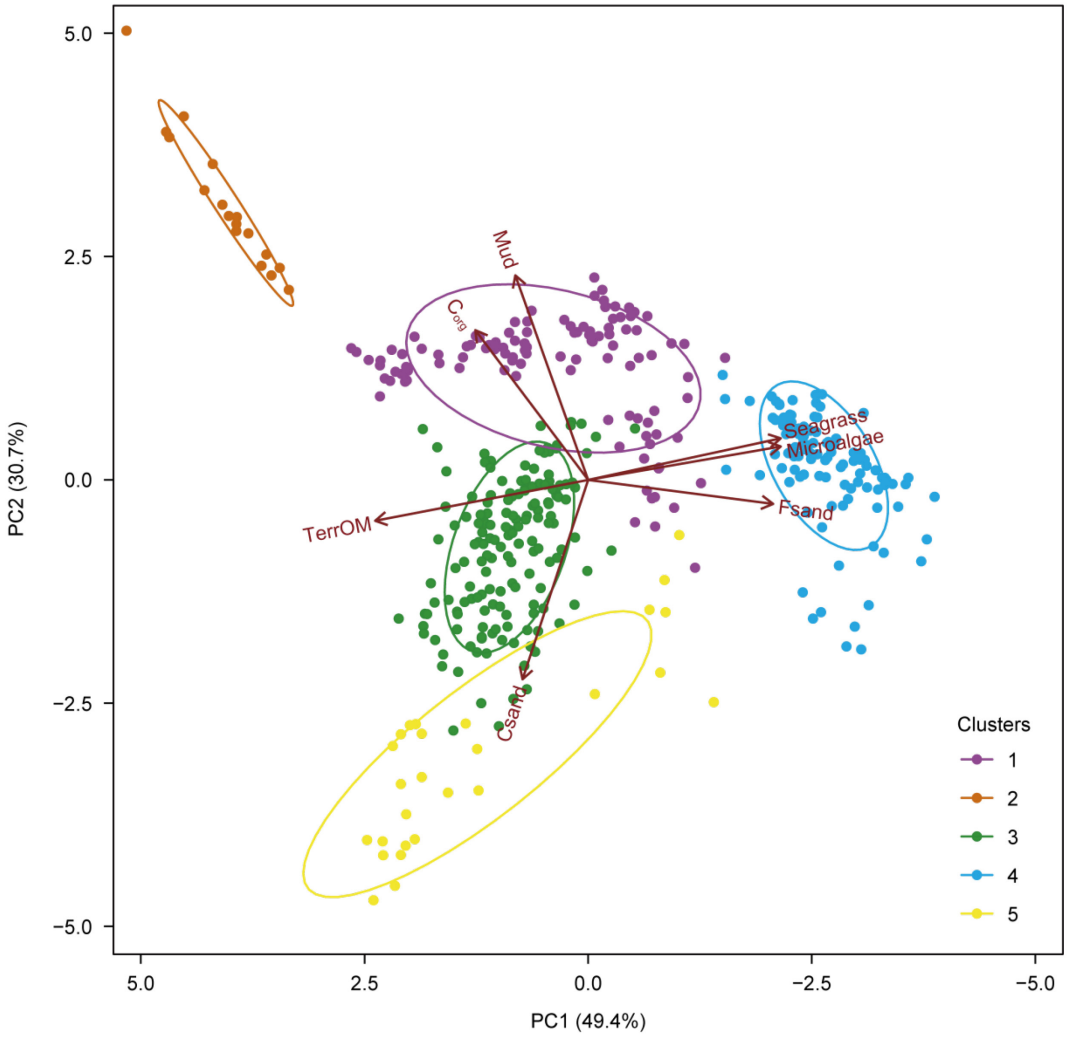

Fig. 6-10. Principal component analysis of C_{org} concentration, grain-size composition (Csand, >500 μm; Fsand, 63–500 μm; Mud, <63 μm), and C_{org} source composition of the sediment samples identified by the change point analysis. The first two axes accounted for 80.1% of the variance. TerrOM, terrestrial-derived organic matter.

Discussion

Historical depositional environment and C_{org} accumulation rate

On both decadal and millennial timeframes, C_{org} accumulation rates were controlled largely by sediment accretion, which has fluctuated historically in Hichirippu and Furen lagoons (Figs. 6-6, 6-7, and 6-9, Table 6-2). Vertical analysis of the geological and biogeochemical features showed that changes of C_{org} accumulation rates were related to historical changes of the depositional environment in eastern Hokkaido. Recent studies have shown that RSL changed locally caused by aperiodic large earthquakes in the late Holocene in the eastern Hokkaido (Nanayama et al., 2003; Kelsey et al., 2006; Sawai et al., 2009). The RSL fluctuations affected the changes in depositional environment and habitat relocations.

The dominant C_{org} sources fluctuated over time in the Hichirippu Lagoon sediment cores (Figs. 6-5 and 6-7). Around 2400 Cal yr BP, microalgae-dominated and low-C_{org} deposits became high-C_{org} deposits dominated by TerrOM (Fig. 6-7a,b). Regarding the formation of these peaty layers (Fig. 6-5 a,b), Sawai et al. (2009) found peaty deposits distributed on a tsunami deposit and have suggested that seismic land uplift abruptly transformed a subtidal environment into a swamp around 2400 Cal yr BP in a lagoon located beside Hichirippu Lagoon. The profile of core H7 also revealed a transition from a sandy layer to an overlying peaty sediment at a depth of 120–140 cm (Fig. 6-5b) at an estimated time of 2400 Cal yr BP (Fig. 6-7b). Although a sandy deposit was not found around 2400 Cal yr BP in core H15 (Fig. 6-5a), peaty sediment was identified at almost the same time (Fig. 6-7a). Peaty sediment was not found in core H12, but the contribution of TerrOM increased above a coarse sand layer (depths of 126–140 cm, Fig. 6-5c) around 2500 Cal yr BP (Fig. 6-7c). These changes in depositional environments occurred simultaneously, driven by a seismic land uplift (Sawai et al., 2009). The C_{org} accumulation rates increased markedly due to the habitat shift from the subtidal zone to the

saltmarsh (Fig. 6-7). These high C_{org} accumulation rates were supported by the rapid supply of saltmarsh debris, which contained high C_{org} (Fig. 6-9, Table 6-2).

The contributions of microalgae and seagrass increased in the upper section of the peaty layers (Fig. 6-7a–c). The reestablishment of a subtidal environment soon after the peaty sediment was deposited in Hichirippu Lagoon demonstrated that the saltmarsh was submerged by the RSL rise. This RSL rise occurred locally and was driven by post-seismic land subsidence (Sawai et al., 2004, 2009). The C_{org} accumulation rate was enhanced by the RSL rise (Fig. 6-7). Rapid sediment accretion was responsible for the rapid C_{org} accumulation under subtidal conditions (Fig. 6-7). The low magnetic susceptibility of these deposits suggests that the SAR was enhanced by the greater water depth and associated attenuation of wave energy and bottom velocities but not by an abrupt increase in riverine sediment load (Fig. 6-5) (Morris et al., 2002; Woodroffe et al., 2016; Collins et al., 2017).

In Furen Lagoon, rapid sediment accretion corresponding to RSL rise enhanced C_{org} accumulation from around 1800 Cal yr BP to 800 Cal yr BP (Fig. 6-6). A previous study identified four seismic uplift events during the past 2000 years: 300 Cal yr BP, 400–600 Cal yr BP, 1400 Cal yr BP, and 1900 Cal yr BP (Kelsey et al., 2006). The periods of rapid accretion and C_{org} accumulation could be linked with the inter-seismic subsidence and RSL rise. C_{org} accumulation rates from 1100 Cal yr BP to 800 Cal yr BP were higher at F25 than at the inner sites. Because F25 was located close to the barrier spits of the lagoon mouth, the abundant sediment supply from outside would have contributed to the high rate of C_{org} accumulation (Theuerkauf and Rodriguez, 2017). In contrast, C_{org} accumulation was inhibited from 800 Cal yr BP to 200 Cal yr BP in Furen Lagoon (Fig. 6-6). The fall of RSL that occurred with land uplift during this period (Kelsey et al., 2006) would have enhanced sediment erosion and reduced C_{org} accumulation rates.

The increase of decadal (the last century) C_{org} accumulation rates in both lagoons could be explained by RSL rise. Geodetic measurements have shown that submergence (including land subsidence and recent sea-level rise due to global climate change) averaged 5–10 mm yr^{-1} during the past century along the Pacific coast of eastern Hokkaido (Atwater et al., 2004). The SAR would be increased by the greater depths of the water columns in both lagoons, but the SARs varied among sites as functions of erosion rates and sediment loading. The C_{org} accumulation rate was significantly higher at the decadal scale than at the millennial scale, except for cores H7 and F41. A caveat to this conclusion is that the dating methods and the cumulative amount of degradation differed for the decadal- and millennial-scale analyses, and sediment compression may have caused the C_{org} accumulation rate in the upper sediment to be overestimated relative to the older sediment (Breithaupt et al., 2018). The depositional environment during the last century, however, would have favored rapid C_{org} accumulation.

Regulating factors of C_{org} accumulation rates in coastal vegetated habitats

Our findings show that RSL changes affect the spatial distribution of habitats and SARs, regulating the decadal- and millennial-scale C_{org} accumulation rates. From these results, the regulating factors of C_{org} accumulation rates were summarized (Figs. 6-11 and 6-12).

The potential of C_{org} accumulation rates is different among habitat types. In this study, the deposits under the saltmarsh conditions represent more rapid C_{org} accumulation rates than those under subtidal conditions (Fig. 6-11). The differences in C_{org} production rate, the recalcitrance of C_{org}, redox condition, and the frequency of inundation would affect the C_{org} accumulation rates (Duarte et al., 2013; Trevathan-Tackett et al., 2015; Watanabe and Kuwae, 2015a).

The present study shows that RSL rise initially increased C_{org} accumulation rates by enhancing sediment accretion in subtidal seagrass meadows. By expanding the area where

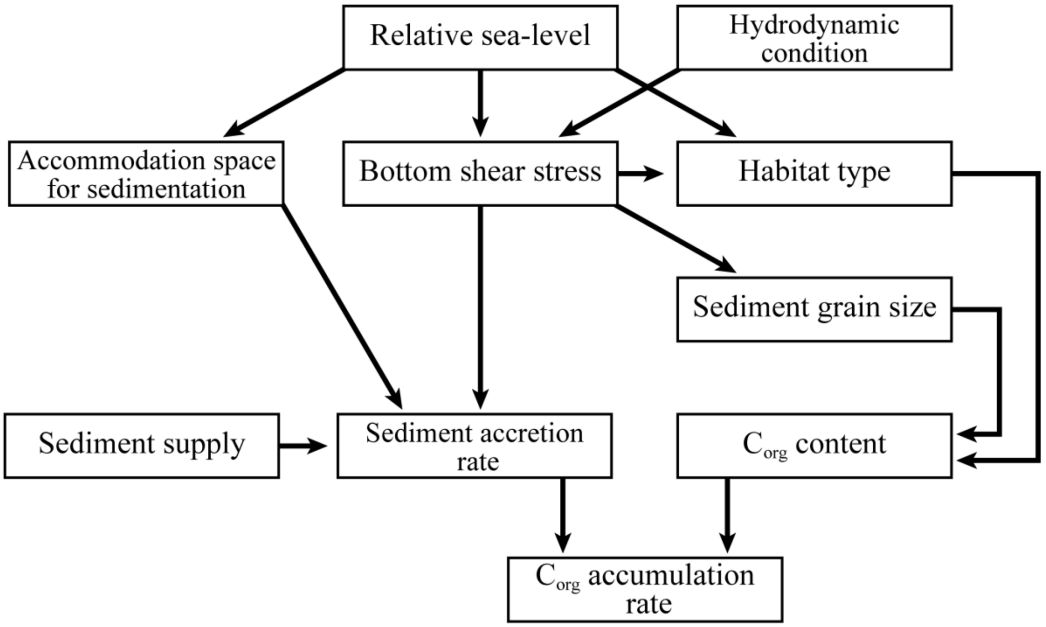

Fig. 6-11. Flow diagram of the regulating factors of C_{org} accumulation rates.

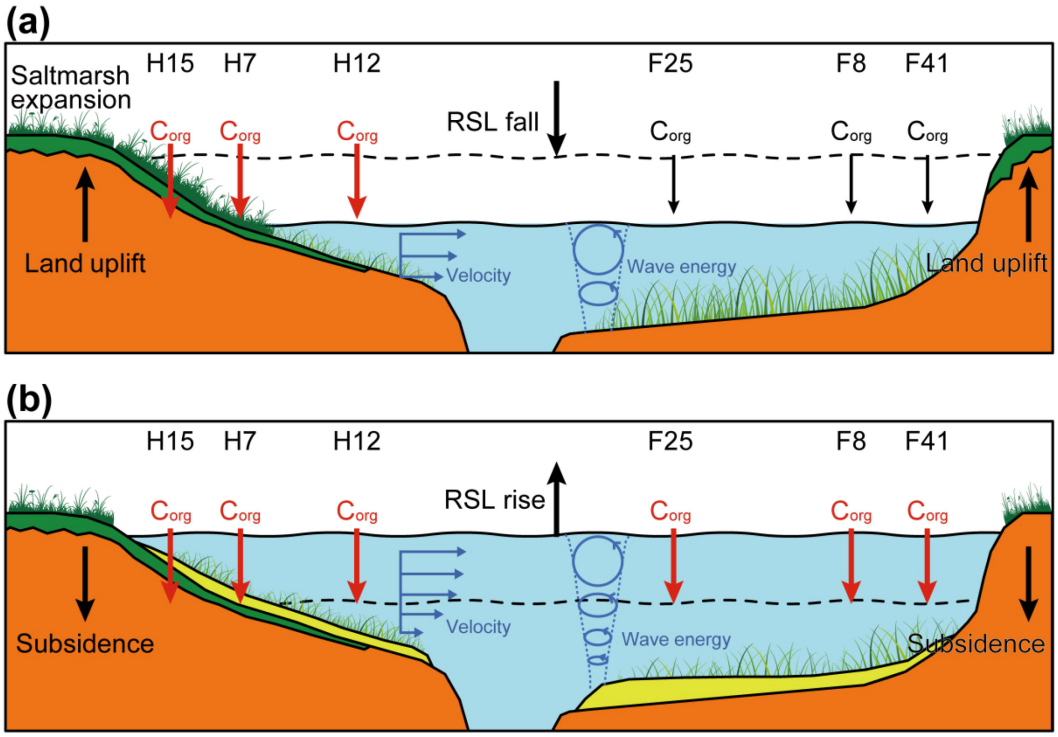

Fig. 6-12. Conceptual diagram of the impact of relative sea-level (RSL) changes on C_{org} accumulation rates in contiguous seagrass–saltmarsh habitats. In inner lagoonal habitats, expansion of saltmarsh habitats to the deeper zone as RSL falls induces the rapid deposition of saltmarsh-derived C_{org} in the supratidal and intertidal zones (**a**). RSL rise induces saltmarsh inundation, which relocates saltmarsh habitats to seagrass meadows (**b**). While RSL rises, the expansion of space to accommodate suspended sediment and the decrease in bottom shear stress accelerate multi-source C_{org} accumulation rates in the subtidal zone (**b**).

sedimentation can occur (Morris et al., 2002; Woodroffe et al., 2016; Collins et al., 2017) and decreasing bottom shear stress, RSL rise enhances sediment accretion in subtidal zones (Figs. 6-11 and 6-12). The high sediment accretion rates during RSL rise in seagrass meadows close to the mouth of Furen Lagoon (Fig. 6-6c) contributed to the high C_{org} accumulation rates. Sediment accretion rates may therefore respond more strongly to sea-level rise in geomorphological settings where sediment loads are abundant. The variable impact of RSL rise on C_{org} accumulation is a function of geomorphological settings, habitats, and hydrodynamic conditions (Fig. 6-11). Furthermore, land-level subsidence locally enhances the influence of sea-level rise (Shields et al., 2017). The rates of sediment supply and the grain size were direct regulators of C_{org} accumulation rates (Figs. 6-9 and 6-11). Global meta-analysis shows that grain size (e.g., specific surface area) is related to C_{org} concentration in *Zostera* meadows (Serrano et al., 2016; Miyajima et al., 2017). These results support that the stabilization of C_{org} by mineral particles (Hedges and Keil, 1995; Zonneveld et al., 2010) is an important mechanism for the long-term C_{org} sequestration.

Future studies concerned with the variability of these factors are needed to enhance understanding of the functionality of vegetated coastal habitats and thereby inform coastal conservation and restoration strategies to mitigate climate change impacts.

Chapter 7

General discussion

What factors determine biological production in a continuum between a river, an estuary, and an adjacent coastal zone?

In this study, I investigated relationships between biogeochemical and hydrological structures and biological production in a continuum between a river, an estuary, and an adjacent coastal zone. Seasonal fluctuations in river discharge regulated hydrological structures in the downstream of the Yura River estuary, which determined habitability and nutrient availability for primary and secondary producers (Chapter 2). The increase in water residence time encouraged biological production under salt-wedge regime in the river. In contrast, high river discharge under the freshwater regime (from winter to spring) flushed out the salt-wedge and discourages biological production in the river. In the adjacent coastal zone, estuarine circulation was driven by river discharge, with high fluxes of nutrients between winter and early spring, enhanced by nutrient supply to the surface water via vertical mixing (Chapter 3). In contrast, low-nutrient seawater was delivered to the coastal zone between late spring and summer. In this model site, iron was mostly transported from the river, and the supply of riverine iron to the coastal ecosystem was substantially affected by the iron removal process in the estuary (Chapter 4). These findings suggest that seasonal changes in hydrological and physical structures (i.e., river discharge, tidal mixing, vertical mixing, and wind) determines the spatial and temporal distribution of the hotspot of biological production in the ecosystem continuum.

The spatial and temporal convergence of primary and secondary production would affect the distribution of fishes in a river–coastal zone continuum. In the Tango Bay coastal zone, primary production increases from winter to early spring, which encourages secondary

production by zooplankton and mysids (Chapter 2 and 3; Akiyama et al., 2015). The larvae and juveniles of commercially important fishes, temperate seabass and flounder, settle in the coastal zone and use the high production of their prey organisms during this period (Takeno et al., 2008; Islam et al., 2010; Fuji et al., 2018; Kasai et al., 2018). Temperate seabass juveniles have partial migration strategy, and use both coastal zones and estuaries as their nurseries (Fuji et al., 2018; Kasai et al., 2018). When coastal biological production is limited by nutrient availability from late spring to summer, a part of juveniles migrate into the river, where the abundant prey enhances their growth relative to individuals remaining in the coastal zone (Chapter 2 and 3; Fuji et al., 2011, 2014, 2018; Kasai et al., 2018; Omweri et al., 2018). The strategy using multi ecosystems would increase total carrying capacity for juveniles (Kasai et al., 2018). The linkage and connectivity between individual ECEs are one of the basis of ecosystem functions (Barbier et al., 2011; Watanabe et al., 2018). The present study indicates that seasonal relocation of the hotspot of biological production would regulate the fishery-related services through the network among ECEs. Future anthropogenic activities and climate change will change the seasonal patterns of river discharge, impacting the biological production processes in ECEs.

What factors affect carbon sequestration processes in shallow coastal ecosystems?

This study investigated the dynamics of organic and inorganic carbon derived from multiple sources at multiple timescales. And then, I assessed the controlling factors of carbon sequestration processes in shallow coastal ecosystems. Shallow coastal ecosystems functioned as carbon sequestration filters through the processes including carbon storage in sediments, carbon sequestration in the water column, and air–water CO_2 exchange (Fig. 5-9) (Chapter 5). The methodology inferring the origin and fates of organic and inorganic carbon revealed the factors affecting these three processes.

Benthic and pelagic primary producers play a major role in converting DIC to C_{org} and thereby decreasing the fCO_2 of the water column, which enhance an influx of atmospheric CO_2 (Chapter 5; Maher and Eyre, 2012; Tokoro et al., 2014; Kubo et al., 2017; Tokoro et al., 2019). In contrast, the inflow of freshwater with the general high-fCO_2 and high-DOC caused the low-salinity zone to be a source of atmospheric CO_2. The balance between biological metabolism and allochthonous carbon input is the key for determining air–water CO_2 flux at biological timescales.

Long-term DOC retention in water column has been overlooked as a carbon sequestration process (Jiao et al., 2014). However, this process can play a substantial role in sequestering atmospheric CO_2 because DOC is a dominant fraction of the water column C_{org} pool and includes a large proportion of refractory C_{org}. Seagrasses directly release refractory DOC that may be preserved in the water column (Chapter 5; Barrón and Duarte, 2009; Opsahl and Benner, 1993). Both macroalgae and microalgae also produce a substantial amount of autochthonous DOC (Carlson, 2002; Wada et al., 2008; Agustí et al., 2013). Because macroalgae grow on rocky shores where sediment accretion does not occur, DOC export would be an important process for sequestering carbon (Krause-Jensen and Duarte, 2016; Krause-Jensen et al., 2018). Future studies should assess the fate of DOC derived from ECEs over long-term timescales.

The recalcitrance of C_{org} differs depending on the origin of C_{org} source, which is one of the factors determining the efficiency of C_{org} storage in sediments (Chapter 5; Zonneveld et al., 2010; Trevathan-Tackett et al., 2015, 2017). Thermogravimetric analysis showed that vascular plant (i.e., seagrasses, mangroves, and saltmarshes) tissues generally exhibited greater stability than macroalgae, consistent with the lignocellulose matrix of vascular plants (Trevathan-Tackett et al., 2015). Also, this study found that terrestrial C_{org} and seagrass-derived C_{org} were stored more efficiently than phytoplankton-derived C_{org} in seagrass meadow sediments, suggesting that

the variability of the composition of C_{org} affects the carbon burial rate (Chapter 5). Geomorphological processes and the subsequent habitat relocation regulated C_{org} accumulation rates at the decadal- and millennial-timescales (Chapter 6). RSL rise enhanced C_{org} accumulation rates by increasing sediment accretion in shallow coastal ecosystems (Figs. 6-11 and 6-12). RSL changes relocate habitat distribution, affecting C_{org} accumulation. Sediment loads and sediment grain size directly regulates C_{org} accumulation (Chapter 6; Zonneveld et al., 2010; Serrano et al., 2016; Miyajima et al., 2019).

Future works: tradeoffs and synergies among ecosystem services

In this thesis, I investigated the regulating drivers of both biological production and carbon sequestration functions in ECEs. These ecosystem functions and services are regulated by interrelated factors. Thus, there is trade-offs and/or synergies among ecosystem functions and services (Carpenter et al., 2009). Without knowledge about the relationships among ecosystem functions and services, we are at risk of incurring unexpected trade-offs, missing opportunities to take advantage of synergies (Bennett et al., 2009). For example, fertilizer use can improve crop production but can have a negative effect on local provision of clean water (Carpenter et al., 1998). In this case, the regulating driver (i.e., fertilizer use) can be in opposite directions, leading to a trade-off. On the other hand, wetland restoration improves both water quality and flood control (Zedler, 2003). In this case, response to a driver that aims to enhance one service can lead to a synergy. In other cases, there are interactions among functions and services. In marine protected areas near coral reefs, conservation of fish populations for tourism also maintains algae-grazing function. Algae-grazing fish helps coral reefs (Hughes et al., 2005). Coral reef provides more habitats for fish populations, enhancing the grazing functioning, as well as improving reef quality for tourism (Bellwood et al., 2004).

How are the relationships between fishery production and carbon sequestration in ECEs? Large amount of nutrient input enhances primary production, which positively affects both of these functions (Kuwae et al., 2016, 2019). Excessive nutrient loads cause hypoxia in enclosed ecosystems, damaging benthic and pelagic populations and decreasing habitable zones. However, from the point of carbon sequestration, the presence of oxygen minimum zone would suppress the mineralization of sedimentary C_{org}, and enhancing C_{org} burial (Kuwae et al., 2016, 2019). Restoration of submerged aquatic vegetation (e.g., seagrass meadows and macroalgal beds) encourages C_{org} storage in sediments and CO_2 absorption (Duarte et al., 2013; Krause-Jensen et al., 2018), and provides habitats and nursery grounds for coastal fishes. In contrast, phytoplankton primary production would be inhibited due to the restoration of submerged aquatic vegetation because they are competitors for nutrients. The appropriate management of river discharge and nutrient loads would keep the biological production of ECEs in a health condition. Meanwhile, the management of excess nutrient inputs is one of the effective strategies for enhancing carbon sequestration function (Macreadie et al., 2017).

Recent studies propose integrated coastal ecosystem management that effectively utilize the connectivity of ECEs and maximize benefits from coastal ecosystems (Barbier et al., 2011; Hori et al., 2018; Watanabe et al., 2018). Future studies should reveal trade-offs and synergies among ecosystem functions and services in ECE networks and propose management strategies. Both field experiments and numerical simulations are necessary (Hori et al., 2018; Itoh et al., 2018; Sohma et al., 2018; Abo et al., 2019; Kuwae et al., 2019). Better understanding of the relationships among multiple ecosystem functions and the mechanisms behind these relationships will improve our strategy to sustainably manage coastal areas to maximize its benefits for the various stakeholders.

Acknowledgements

I am deeply grateful to Dr. Yoh Yamashita of Field Science Education and Research Center, Kyoto University, for his invaluable support and guidance over the years. I owe my deep gratitude to Dr. Tomohiro Kuwae of Port and Airport Research Institute. Without their support and encouragement, this thesis would have never been completed.

I am also grateful to Dr. Akihide Kasai of Hokkaido University, Dr. Takahito Yoshioka and Dr. Shigeki Sawayama of Kyoto University, Dr. Shigeru Montani of Hokkaido University, and Dr. Kazuhiko Ichimi of Kagawa University for giving insightful comments and powerful support. I sincerely thank Dr. Reiji Masuda, Dr. Masahiro Ueno, Dr. Yoshiaki Kai, Dr. Keita Suzuki, Dr. Masatomo Tagawa, Dr. Koji Nakayama, Dr. Keitaro Fukushima, Dr. Koji Fukuzaki, Dr. Kenji Minami, Dr. Emily S. Antonio, Dr. Satoshi Akiyama, Dr. Shoko Akiyama, Mr. Kentaro Suzuki, Dr. Koji Takahashi, Dr. Yuko Taga, Mr. Makoto Taga, Mr. Koji Tokuda, Captain Kazuo Sato, Dr. Taiki Fuji, and Mr. Tatsuhiro Funahashi of Kyoto University for their constructive suggestions and help for sampling and student life in Kyoto.

I specially thank to Mr. Eiichi Miyoshi, Dr. Tatsuki Tokoro, Dr. Hirotada Moki, Ms. Toko Tanaya, Mr. Kazufumi Tada, Mr. Junichi Kyoda, Dr. Tetsunori Inoue, and Dr. Shinya Hosokawa of Port and Airport Research Institute for their valuable comments and help for fieldwork. I also thank to Mrs. Kiori Sakihara, Ms. Ayami Okuno, and Ms. Naoko Umegaki for chemical analysis. I would like to express my gratitude to Dr. Koji Seike of National Institute of Advanced Industrial Science and Technology, Dr. Rumiko Kajihara of Civil Engineering Research Institute for Cold Region, Mr. Seiichiro Shibanuma and Dr. Yasuyo Tsuji of Hokkaido University for help the study in Hokkaido. I also thank to Dr. Michihiro Aimoto of Nippon Steel and Sumitomo Metal Corporation for iron analysis.

Sediment core analysis in Chapter 6 was performed under the cooperative research program of the Center for Advanced Marine Core Research (CMCR), Kochi University (accept no. 12B041, 13A026, and 13B023).

Finally, I would like to express my deep and sincere gratitude to my family for their continuous support and encouragement throughout my studies. I am grateful to my wife, Momoko Watanabe, for encouraging me to proceed to write this thesis. I am grateful to my parents, my brother, and my grandparents for supporting my life and giving me an opportunity to study marine ecology and coastal biogeochemistry.

References

Abo, K., Sugimatsu, K., Hori, M., Yoshida, G., Shimabukuro, H., Yagi, H., Nakayama, A., and Tarutani, K. 2019. Quantifying the Fate of Captured Carbon: From Seagrass Meadows to the Deep Sea. In Kuwae, T., Hori, M. (Eds.), Blue Carbon in Shallow Coastal Ecosystems: Carbon Dynamics, Policy, and Implementation, Springer, Singapore, pp.251–271.

Adachi, H., Yamano, H., Miyajima, T., and Nakaoka, M. 2010. A simple and robust procedure for coring unconsolidated sediment in shallow water. Journal of Oceanography **66**: 865–872.

Agustí, S., and Duarte, C. M. 2013. Phytoplankton lysis predicts dissolved organic carbon release in marine plankton communities. Biogeosciences **10**: 1259–1264.

Aimoto, M., Kato, T., Kiso, E., Tsutsumi, N., and Miki, O. 2011. Analysis of trace iron (Fe) in sea water by using inductively coupled plasma mass spectrometry with solid phase chelate extraction technique. Nippon Steel Technical Report **100**: 85–91.

Akaike, H. 1974. A new look at the statistical model identification. IEEE Transactions on Automatic Control **19**: 716–723.

Akiyama, S., Ueno, M., and Yamashita, Y. 2015. Population dynamics and reproductive biology of the mysid *Orientomysis japonica* in Tango Bay, Japan. Plankton and Benthos Research **10**: 121–131.

Antonio, E. S., Kasai, A., Ueno, M., Kurikawa, Y., Tsuchiya, K., Toyohara, H., Ishihi, Y., Yokoyama, H., and Yamashita, Y. 2010a. Consumption of terrestrial organic matter by estuarine molluscs determined by analysis of their stable isotopes and cellulase activity. Estuarine, Coastal and Shelf Science **86**: 401–407.

Antonio, E. S., Kasai, A., Ueno, M., Won, N., Ishihi, Y., Yokoyama, H., and Yamashita, Y. 2010b. Spatial variation in organic matter utilization by benthic communities from Yura River-Estuary to offshore of Tango Sea, Japan. Estuarine, Coastal and Shelf Science **86**: 107–117.

Antonio, E. S., Kasai, A., Ueno, M., Ishihi, Y., Yokoyama, H., and Yamashita, Y. 2012. Spatial-temporal feeding dynamics of benthic communities in an estuary-marine gradient. Estuarine, Coastal and Shelf Science **112**: 86–97.

Aoki, T., Kasai, A., Fuji, T., Ueno, M., and Yamashita, Y. 2014. Seasonal variation in the fish community and their prey organisms in the Yura River estuary. Bulletin of Japanese Society of Fisheries Oceanography **78**: 1–12. (in Japanese with English abstract)

Appleby, P., and Oldfield, F. 1978. The calculation of lead-210 dates assuming a constant rate of supply of unsupported ^{210}Pb to the sediment. Catena **5**: 1–8.

Armitage, A. R., and Fourqurean, J. W. 2016. Carbon storage in seagrass soils: long-term nutrient history exceeds the effects of near-term nutrient enrichment. Biogeosciences **13**: 313–321.

Artigas, M. L., Llebot, C., Ross, O. N., Neszi, N. Z., Rodellas, V., Garcia-Orellana, J., Masqué, P., Piera, J., Estrada, M., and Berdalet, E. 2014. Understanding the spatio-temporal variability of phytoplankton biomass distribution in a microtidal Mediterranean estuary. Deep-Sea Research Part II **101**: 180–192.

Astoreca, R., Rousseau, V., and Lancelot, C. 2009. Coloured dissolved organic matter (CDOM) in Southern North Sea waters: Optical characterization and possible origin. Estuarine, Coastal and Shelf Science **85**: 633–640.

Atwater, B. F., Furukawa, R., Hemphill-Haley, E., Ikeda, Y., Kashima, K., Kawase, K., Kelsey, H. M., Moore, A. L., Nanayama, F., Nishimura, Y., Odagiri, S., Ota, Y., Park, S-C., Satake,

K., Sawai, Y., and Shimokawa, K. 2004. Seventeenth-century uplift in eastern Hokkaido, Japan. Holocene **14**: 487–501.

Atwood, T. B., Connolly, R. M., Ritchie, E. G., Lovelock, C. E., Heithaus, M. R., Hays, G. C., Fourqurean, J. W., and Macreadie, P. I. 2015. Predators help protect carbon stocks in blue carbon ecosystems. Nature Climate Change **5**: 1038–1045.

Balzano, S., Sarno, D., and Kooistra, W. H. C. F. 2011. Effects of salinity on the growth rate and morphology of ten *Skeletonema* strains. Journal of Plankton Research **33**: 937–945.

Barbier, E. B., Hacker, S. D., Kennedy, C., Koch, E. W., Stier, A. C., and Silliman, B. R. 2011. The value of estuarine and coastal ecosystem services. Ecological Monographs **81**: 169–193.

Barrón, C., and Duarte, C. M. 2009. Dissolved organic matter release in a *Posidonia oceanica* meadow. Marine Ecology Progress Series **374**: 75–84.

Bauer, J. E., Cai, W.-J., Raymond, P. A., Bianchi, T. S., Hopkinson, C. S., and Regnier, P. A. G. 2013. The changing carbon cycle of the coastal ocean. Nature **504**: 61–70.

Bellwood, D. R., Hughes, T. P., Folke, C., and Nystrom, M. 2004. Confronting the coral reef crisis. Nature **429**: 827–833.

Bennett, E. M., Peterson, G. D., and Gordon, L. J. 2009. Understanding relationships among multiple ecosystem services. Ecology Letters **12**: 1394–1404.

Bergamaschi, B. A., Krabbenhoft, D. P., Aiken, G. R., Patino, E., Rumbold, D. G., and Orem, W. H. 2012. Tidally driven export of dissolved organic carbon, total mercury, and methylmercury from a mangrove-dominated estuary. Environmental Science and Technology **46**: 1371–1378.

Bergquist, B. A., Wu, J., and Boyle, E. A. 2007. Variability in oceanic dissolved iron is dominated by the colloidal fraction. Geochimica et Cosmochimica Acta **71**: 2960–2974.

Bergström, S., Carlsson, B., Gardelin, M., Lindström, G., Petterson, A., and Rummukainen, M. 2001. Climate change impacts on runoff in Sweden—assessments by global climate models, dynamical downscaling and hydrological modeling. Climate Research **16**: 101–112.

Bianchi, T. S. 2007. Biogeochemistry of estuaries. Oxford University Press, New York, USA.

Biddanda, B., and Benner, R. 1997. Carbon, nitrogen, and carbohydrate fluxes during the production of particulate and dissolved organic matter by marine phytoplankton. Limnology and Oceanography **42**: 506–518.

Blaauw, M., and Christen, J. A. 2011. Flexible paleoclimate age-depth models using an autoregressive gamma process. Bayesian Analysis **6**: 457–474.

Borges, A. V. 2005. Do we have enough pieces of the jigsaw to integrate CO_2 fluxes in the coastal ocean? Estuaries **28**: 3–27.

Borges, A. V., Dellile, B., and Frankignoulle, M. 2005. Budgeting sinks and sources of CO_2 in the coastal ocean: diversity of ecosystems counts. Geophysical Research Letters **32**: L14601.

Botto, F., Gaitan, E., Mianzan, H., Acha, M., Giberto, D., Schiariti, A., and Iribarne, O. 2011. Origin of resources and trophic pathways in a large SW Atlantic estuary: An evaluation using stable isotopes. Estuarine, Coastal and Shelf Science **92**: 70–77.

Boyd, P. W., and Ellwood, M. J. 2010. The biogeochemical cycle of iron in the ocean. Nature Geoscience **3**: 675–682.

Boyd, P. W., Strzepek, R., Fu, F. X., and Hutchins, D. A. 2010. Environmental control of open-ocean phytoplankton groups: now and in the future. Limnology and Oceanography **55**: 1353–1376.

Boyle, E., Collier, R., Dengler, A. T., Edmond, J. M., Ng, A. C., and Stallard, R. F. 1974. On the

chemical mass-balance in estuaries. Geochimica et Cosmochimica Acta **38**: 1719–1728.

Boyle, E. A., Edmond, J. M., and Sholkovitz, E. R. 1977. Mechanism of iron removal in estuaries. Geochimica et Cosmochimica Acta **41**: 1313–1324.

Breithaupt, J. L., Smoak, J. M., Byrne, R. H., Waters, M. N., Moyer, R. P., and Sanders, C. J. 2018. Avoiding timescale bias in assessments of coastal wetland vertical change. Limnology and Oceanography **63**: S477–S495.

Bricaud, A., Morel, A., and Prieur, L. 1981. Absorption by dissolved organic matter of the sea (yellow substance) in the UV and visible domains. Limnology and Oceanography **26**: 43–53.

Brzezinski, M. A. 1985. The Si:C:N ratio of marine diatoms: interspecific variability and the effect of some environmental variables. Journal of Phycology **21**: 347–357.

Buck, K. N., Lohan, M. C., Berger, C. J. M., and Bruland, K. W. 2007. Dissolved iron speciation in two distinct river plumes and an estuary: implications for riverine iron supply. Limnology and Oceanography **52**: 843–855.

Bundy, R. M., Abdulla, H. A. N., Hatcher, P. G., Biller, D. V., Buck, K. N., and Barbeau, K. A. 2015. Iron-binding ligands and humic substances in the San Francisco Bay estuary and estuarine-influenced shelf regions of coastal California. Marine Chemistry **173**: 183–194.

Caddy, J. F., and Bakun, A. 1994. A tentative classification of coastal marine ecosystems based on dominant processes on nutrient supply. Ocean and Coastal Management **23**: 201–211.

Cahoon, D. R., Hensel, P., Rybczyk, J., McKee, K. L., Proffitt, C. E., and Perez, B. C. 2003. Mass tree mortality leads to mangrove peat collapse at Bay Islands, Honduras after Hurricane Mitch. Journal of Ecology **91**: 1093–1105.

Cai, W.-J. 2011. Estuarine and coastal ocean carbon paradox: CO_2 sinks or sites of terrestrial carbon incineration? Annual Review of Marine Science **3**: 123–145.

Cai, W.-J., Dai, M., and Wang, Y. 2006. Air-sea exchange of carbon dioxide in ocean margins: a province-based synthesis. Geophysical Research Letters **33**: L12603.

Carlson, C. A. 2002. Production and removal processes. In Hansell, D. A., and Carlson, C. A. (Eds.), Biogeochemistry of marine dissolved organic matter, Academic Press, Waltham, Massachusetts, USA, pp. 91–151.

Carpenter, S. R., Caraco, N. F., Corell, D. L., Howarth, R. W., Sharpley, A. N., and Smith, V. H. 1998. Nonpoint pollution of surface waters with phosphorus and nitrogen. Ecological Applications **8**: 559–568.

Carpenter, S. R., Mooney, H. A., Agard, J., Capistrano, D., Defries, R. S., Diaz, S., Dietz, T., Duraiappah, A. K., Oteng-Yeboah, A., Pereira, H. M., Perrings, C., Reid, W. V., Sarukhan, J., Scholes, R. J., and Whyte, A. 2009. Science for managing ecosystem services: beyond the millennium ecosystem assessment. Proceedings of the National Academy of Sciences of the United States of America **106**: 1305–1312.

Cauwet, G. 1991. Carbon inputs and biogeochemical processes at the halocline in a stratified estuary—Krka River, Yugoslavia. Marine Chemistry **32**: 269–283.

Chan, T. U., and Hamilton, D. P. 2001. Effect of freshwater flow on the succession and biomass of phytoplankton in a seasonal estuary. Marine and Freshwater Research **52**: 869–884.

Chen, C.-T. A., and Borges, A. V. 2009. Reconciling opposing views on carbon cycling in the coastal ocean: continental shelves as sinks and near-shore ecosystems as sources of atmospheric CO_2. Deep-Sea Research Part II 56: 578–590.

Chen, C.-T. A., Huang, T. H., Fu, Y. H., Bai, Y., and He, X. 2012. Strong sources of CO_2 in upper estuaries become sinks of CO_2 in large river plumes. Current Opinion in Environmental Sustainability **4**: 179–185.

Chen, M., Price, R. M., Yamashita, Y., and Jaffé, R. 2010. Comparative study of dissolved

organic matter from groundwater and surface water in the Florida coastal Everglades using multi-dimensional spectrofluorometry combined with multivariate statistics. Applied Geochemistry **25**: 872–880.

Chen, Z., Hu, C., Conmy, R. N., Muller-Karger, F., and Swarzenski, P. 2007. Colored dissolved organic matter in Tampa Bay, Florida. Marine Chemistry **104**: 98–109.

Clesceri, L. S., Greenberg, A. E., and Eaton, A. D. 1998. Standard Methods for the Examination of Water and Wastewater. APHA, AWWA, and WEF, Maryland.

Cloern, J. E. 1996. Phytoplankton bloom dynamics in coastal ecosystems: A review with some general lessons from sustained investigation of San Francisco Bay, California. Reviews of Geophysics **34**: 127–168.

Cloern, J. E., and Jassby, A. D. 2008. Complex seasonal patterns of primary producers at the land–sea interface. Ecology Letters **11**: 1294–1303.

Cloern, J. E., Foster, S. Q., and Kleckner, A. E. 2014. Phytoplankton primary production in the world's estuarine-coastal ecosystems. Biogeosciences **11**: 2477–2501.

Coale, K. H., Fitzwater, S. E., Gordon, R. M., Johnson, K. S., and Barber, R. T. 1996. Control of community growth and export production by upwelled iron in the equatorial Pacific Ocean. Nature **379**: 621–624.

Coble, P. G., Del Castillo, C. E., and Avril, B. 1998. Distribution and optical properties of CDOM in the Arabian Sea during the 1995 Southwest Monsoon. Deep-Sea Research Part II **45**: 2195–2223.

Collins, D. S., Avdis, A., Allison, P. A., Johnson, H. D., Hill, J., Piggott, M. D., Hassan, M. H. A., and Damit, A. R. 2017. Tidal dynamics and mangrove carbon sequestration during the Oligo–Miocene in the South China Sea. Nature Communications **8**: 15698.

Connolly, R. M., Schlacher, T. A., and Gaston, T. F. 2009. Stable isotope evidence for trophic

subsidy of coastal benthic fisheries by river discharge plumes off small estuaries. Marine Biology Research **5**: 164–171.

Cory, R. M., and McKnight, D. M. 2005. Fluorescence spectroscopy reveals ubiquitous presence of oxidized and reduced quinones in dissolved organic matter. Environmental Science and Technology **39**: 8142–8149.

Cossa, D., Tremblay, G. H., and Gobeil, C. 1990. Seasonality in iron and manganese concentrations of the St. Lawrence River. Science of the Total Environment **97**(**98**): 185–190.

Costa, L. S., Huszar, V. L. M., and Ovalle, A. R. 2009. Phytoplankton functional groups in a tropical estuary: Hydrological control and nutrient limitation. Estuaries and Coasts **32**: 508–521.

Costanza, R., dArge, R., de Groot, R., Farber, S., Grasso, M., Hannon, B., Limburg, K., Naeem, S., O'Neill, R. V., Paruelo, J., Raskin, R. G., Sutton, P., and van den Belt, M. 1997. The value of the world's ecosystem services and natural capital. Nature **387**: 253–260.

Costanza, R., de Groot, R., Sutton, P., van der Ploeg, S., Anderson, S. J., Kubiszewski, I., Farber, S., and Turner, R. K. 2014. Changes in the global value of ecosystem services. Global Environmental Change **26**: 152–158.

Craft, C., Clough, J., Ehman, J., Joye, S., Park, R., Pennings, S., Guo, H., and Machmuller, M. 2009. Forecasting the effects of accelerated sea-level rise on tidal marsh ecosystem services. Frontiers in Ecology and the Environment **7**: 73–78.

Dabrin, A., Schäfer, J., Blanc, G., Strady, E., Masson, M., Bossy, C., Castelle, S., Girardot, N., and Coynel, A. 2009. Improving estuarine net flux estimates for dissolved cadmium export at the annual timescale: application to the Gironde Estuary. Estuarine, Coastal and Shelf Science **84**: 429–439.

Davis, K. A., Banas, N. S., Giddings, S. N., Siedlecki, S. A., MacCready, P., Lessard, E. J., Kudela, R. M., and Hickey, B. M. 2014. Estuary-enhanced upwelling of marine nutrients fuels coastal productivity in the U.S. Pacific Northwest. Journal of Geophysical Research: Oceans **119**: 8778–8799.

de Baar, H. J. W., de Jong, J. R. M., Bakker, D. C. E., Löscher, B. M., Veth, C., Bathmann, U., and Smetacek, V. 1995. Importance of iron for plankton blooms and carbon dioxide drawdown in the Southern Ocean. Nature **373**: 412–415.

Determann, S., Reuter, R., Wagner, P., and Willkomm, R. 1994. Fluorescent matter in the eastern Atlantic Ocean. Part 1: method of measurement and near-surface distribution. Deep-Sea Research Part I **41**: 659–675.

Dortch, Q., and Whitledge, T. E. 1992. Does nitrogen or silicon limit phytoplankton production in the Mississippi River plume and nearby regions? Continental Shelf Research **12**: 1293–1309.

Duarte, C. M., Losada, I. J., Hendriks, I. E., Mazarrasa, I., and Marbà, N. 2013. The role of coastal plant communities for climate change mitigation and adaptation. Nature Climate Change **3**: 961–968.

Duarte, C. M., Marbà, N., Gacia, E., Fourqurean, J. W., Beggins, J., Barrón, C., and Apostolaki, E. T. 2010. Seagrass community metabolism: Assessing the carbon sink capacity of seagrass meadows. Global Biogeochemical Cycles **24**: GB4032.

Dubois, S., Savoye, N., Grémare, A., Plus, M., Charlier, K., Beltoise, A., and Blanchet, H. 2012. Origin and composition of sediment organic matter in a coastal semi-enclosed ecosystem: An elemental and isotopic study at the ecosystem space scale. Journal of Marine Systems **94**: 64–73.

Durham, W. M., and Stocker, R. 2012. Thin phytoplankton layers: characteristics, mechanisms,

and consequences. Annual Review of Marine Science **4**: 177–207.

Elliott, M., and Whitfield, A. K. 2011. Challenging paradigms in estuarine ecology and management. Estuarine, Coastal and Shelf Science **94**: 306–314.

Elrod, V. A., Berelson, W. M., Coale, K. H., and Johnson, K. S. 2004. The flux of iron from continental shelf sediments: a missing source for global budgets. Geophysical Research Letters **31**: L12307.

Falco, S., Niencheski, L. F., Rodilla, M., Romero, I., González del Río, J., Sierra, J. P., and Mösso, C. 2010. Nutrient flux and budget in the Ebro estuary. Estuarine, Coastal and Shelf Science **87**: 92–102.

Ferguson, A. J. P., Gruber, R., Potts, J., Wright, A., Welsh, D. T., and Scanes, P. 2017. Oxygen and carbon metabolism of *Zostera muelleri* across a depth gradient – Implications for resilience and blue carbon. Estuarine, Coastal and Shelf Science **187**: 216–230.

Fichot, C. G., and Benner, R. 2012. The spectral slope coefficient of chromophoric dissolved organic matter ($S_{275–295}$) as a tracer of terrigenous dissolved organic carbon in river-influenced ocean margins. Limnology and Oceanography **57**: 1453–1466.

Finlayson, B. L., and McMahon, T. A., 1988. Australia vs the world: A comparative analysis of stream flow characteristics. In Warner, R. F. (Eds.), Fluvial Geomorphology of Australia. Academic Press, Sydney, pp. 17–40.

Fourqurean, J. W., Duarte, C. M., Kennedy, H. Marbà, N., Holmer, M., Mateo, M. A., Apostolaki, E. T., Kendrick, G. A., Krause-Jensen, D., McGlathery, K. J., and Serrano, O. 2012. Seagrass ecosystems as a globally significant carbon stock. Nature Geoscience **5**: 505–509.

Fox, L. E., and Wofsy, S. C. 1983. Kinetics of removal of iron colloids from estuaries. Geochimica et Cosmochimica Acta **47**: 211–216.

Fox, L. E., Sager, S. L., and Wofsy, S. C. 1986. The chemical control of soluble phosphorus in the Amazon estuary. Geochimica et Cosmochimica Acta **50**: 783–794.

Fry, B. 2006. Stable Isotope Ecology. Springer, New York, USA.

Fuji, T., Kasai, A., Suzuki, W. K., Ueno, M., and Yamashita, Y. 2010. Freshwater migration and feeding habits of juvenile temperate seabass *Lateolabrax japonicus* in the stratified Yura River estuary, the Sea of Japan. Fisheries Science **76**: 643–652.

Fuji, T., Kasai, A., Suzuki, W. K., Ueno, M., and Yamashita, Y. 2011. Migration ecology of juvenile temperate seabass *Lateolabrax japonicus*: a carbon stable-isotope approach. Journal of Fish Biology **78**: 2010–2025.

Fuji, T., Kasai, A., Ueno, M., and Yamashita, Y. 2014. Growth and migration patterns of juvenile temperate seabass *Lateolabrax japonicus* in the Yura River estuary, Japan—combination of stable isotope ratio and otolith microstructure analyses. Environmental Biology of Fishes **97**: 1221–1232.

Fuji, T., Kasai, A., and Yamashita, Y. 2018. Upstream migration mechanisms of juvenile temperate sea bass *Lateolabrax japonicus* in the stratified Yura River estuary. Fisheries Science **84**: 163–172.

Fujii, M., Rose, A. L., Waite, T. D., and Omura, T. 2008. Effect of divalent cations on the kinetics of Fe(III) complexation by organic ligands in natural waters. Geochimica et Cosmochimica Acta **72**: 1335–1349.

Fujita, S., Kuma, K., Ishikawa, S., Nishimura, S., Nakayama, Y., Ushizaka, S., Isoda, Y., Otosaka, S., and Aramaki, T. 2010. Iron distributions in the water column of the Japan Basin and Yamato Basin (Japan Sea). Journal of Geophysical Research: Oceans **115**: C12001.

Fujiwara, T., Fukui, S., and Sugiyama, Y. 1996. Seasonal variation in stratification and estuarine

circulation of Ise Bay. Oceanography in Japan **5**: 235–244. (in Japanese with English abstract)

Fuks, D., Devescovi, M., Precali, R., Krstulovic, N., and Solic, M. 1991. Bacterial abundance and activity in the highly stratified estuary of the Krka river. Marine chemistry **32**: 333–346.

Fukuzaki, K., Imai, I., Fukushima, K., Ishii, K., Sawayama, S., and Yoshioka, T. 2014. Fluorescent characteristics of dissolved organic matter produced by bloom-forming coastal phytoplankton. Journal of Plankton Research **36**: 685–694.

Funahashi, T., Kasai, A., Ueno, M., Yamashita, Y. 2013. Effects of Short Time Variation in the River Discharge on the Salt Wedge Intrusion in the Yura Estuary, a Micro Tidal Estuary, Japan. Journal of Water Resource and Protection **5**: 29226.

Gaulke, A. K., Wetz, M. S., and Paerl, H. W. 2010. Picophytoplankton: A major contributor to planktonic biomass and primary production in a eutrophic, river-dominated estuary. Estuarine, Coastal and Shelf Science **90**: 45–54.

Gledhill, M., and van den Berg, C. M. G. 1994. Determination of complexation of iron(III) with natural organic complexing ligands in seawater using cathodic stripping voltammetry. Marine Chemistry **47**: 41–54.

Goñi, M. A., Teixeira, M. J., and Perkey, D. W. 2003. Sources and distribution of organic matter in a river-dominated estuary (Winyah Bay, SC, USA). Estuarine, Coastal and Shelf Science **57**: 1023–1048.

González del Río, J., Romero, I., Falco, S., Rodilla, M., Saez, M., Sierra, J. P., Sánchez-Arcilla, A., and Mösso, C. 2007. Changes in phytoplankton population along the saline gradient of the Júcar Estuary and Plume. Journal of Coastal Research **47**: 63–68.

Graham, L. P. 2004. Climate change effects on river flow to the Baltic Sea. Ambio **33**: 235–241.

Guan, J., Yan, B., Zhu, H., Wang, L., Lu, D., and Cheng, L. 2015. Flux characteristics of total dissolved iron and its species during extreme rainfall event in the midstream of the Heilongjiang River. Journal of Environmental Sciences **30**: 74–80.

Guerra, R., Pistocchi, R., and Vanucci, S. 2013. Dynamics and sources of organic carbon in suspended particulate matter and sediments in Pialassa Baiona lagoon (NW Adriatic Sea, Italy). Estuarine, Coastal and Shelf Science **135**: 24–32.

Gullström, M., Lyimo, L. D., Dahl, M., Samuelsson, G. S., Eggertsen, M., Anderberg, E., Rasmusson, L. M., Linderholm, H. W., Knudby, A., Bandeira, S., Nordlund, L. M., and Björk, M. 2018. Blue carbon storage in tropical seagrass meadows relates to carbonate stock dynamics, plant–sediment processes, and landscape context: insights from the western Indian Ocean. Ecosystems **21**: 551–566.

Halpern, B. S., Longo, C., Hardy, D., McLeod, K. L., Samhouri, J. F., Katona, S. K., Kleisner, K., Lester, S. E., O'Leary, J., Ranelletti, M., Rosenberg, A. A., Scarborough, C., Selig, E. R., Best, B. D., Brumbaugh, D. R., Chapin, F. S., Crowder, L. B., Daly, K. L., Doney, S. C., Elfes, C., Fogarty, M. J., Gaines, S. D., Jacobsen, K. I., Karrer, L. B., Leslie, H. M., Neeley, E., Pauly, D., Polasky, S., Ris, B., St Martin, K., Stone, G. S., Sumaila, U. R., and Zeller, D. 2012. An index to assess the health and benefits of the global ocean. Nature 488: 615–620.

Hammes, F., Vital, M., and Egli, T. 2010. Critical evaluation of the volumetric "bottle effect" on microbial batch growth. Applied and Environmental Microbiology **76**: 1278–1281.

Haralambidou, K., Sylaios, G., and Tsihrintzis, V. A. 2010. Salt-wedge propagation in a Mediterranean micro-tidal river mouth. Estuarine, Coastal and Shelf Science **90**: 174–184.

Harmelin-Vivien, M., Dierking, J., Bănaru, D., Fontaine, M. F., and Arlhac, D. 2010. Seasonal

variation in stable C and N isotope ratios of the Rhone River inputs to the Mediterranean Sea (2004–2005). Biogeochemistry **100**: 139–150.

Harrison, P. J., Yin, K., Lee, J. H. W., Gan, J., and Liu, H. 2008. Physical–biological coupling in the Pearl River Estuary. Continental Shelf Research **28**: 1405–1415.

Hedges, J. I., Cowie, G. L., Richey, J. E., Quay, P. D., Brenner, R., Strom, M., and Forsberg, B. 1994. Origin and processing of organic matter in the Amazon River as indicated by carbohydrates and amino acids. Limnology and Oceanography **39**: 743–761.

Hedges, J. I., and Keil, R. G. 1995. Sedimentary organic matter preservation: an assessment and speculative synthesis. Marine Chemistry **49**: 81–115.

Heller, M. I., Gaiero, D. M., and Groot, P. L. 2013. Basin scale survey of marine humic fluorescence in the Atlantic: relationship to iron solubility and H_2O_2. Global Biogeochemical Cycles **27**: 88–100.

Helms, J. R., Stubbins, A., Ritchie, J. D., Minor, E. C., Kieber, D. J., and Mopper, K. 2008. Absorption spectral slopes and slope ratios as indicators of molecular weight, source, and photobleaching of chromophoric dissolved organic matter. Limnology and Oceanography **53**: 955–969.

Hioki, N., Kuma, K., Morita, Y., Sasayama, R., Ooki, A., Kondo, Y., Obata, H., Nishioka, J., Yamashita, Y., Nishino, S., Kikuchi, T., and Aoyama, M. 2014. Laterally spreading iron, humic-like dissolved organic matter and nutrients in cold, dense subsurface water of the Arctic Ocean. Scientific Reports **4**: 6775.

Hirota, R., and Hara, M. 1975. Zooplankton investigations in Yatsushiro-kai, western Kyushu, I. regional and seasonal occurrences of the important zooplankton. Journal of the Oceanographical Society of Japan **31**: 115–123.

Hori, M., Hamaoka, H., Hirota, M., Lagarde, F., Vaz, S., Hamaguchi, M., Hori, J., and Makino,

M. 2018. Application of the coastal ecosystem complex concept toward integrated management for sustainable coastal fisheries under oligotrophication. Fisheries Science **84**: 283–292.

Hori, M., and Kuwae, T. (Eds.) 2017. Blue carbon: hidden processes for CO_2 uptake and carbon storage in shallow water ecosystems, policy and implementation, Chijinshokan Press, Tokyo. (in Japanese)

House, W.A. 2003. Geochemical cycling of phosphorus in rivers. Applied Geochemistry **18**: 739–748.

Hughes, T. P., Bellwood, D. R., Folke, C., Steneck, R. S., and Wilson, J. 2005. New paradigms for supporting the resilience of marine ecosystems. Trends in Ecology & Evolution **20**: 380–386.

Hur, J., Park, M. H., and Schlautman, M. A. 2009. Microbial transformation of dissolved leaf litter organic matter and its effects on selected organic matter operational descriptors. Environmental Science and Technology **43**: 2315–2321.

Inoue, T., and Ebise, S. 1991. Runoff characteristics of COD, BOD, C, N and P loadings from rivers to enclosed coastal seas. Marine Pollution Bulletin **23**: 11–14.

IPCC. 2013. Carbon and other biogeochemical cycles. In Stocker, T. F., Qin, D., Plattner, G. K. et al. (Eds.), Climate Change 2013: The Physical Science Basis. Contribution of Working Group I to the Fifth Assessment Report of the Intergovernmental Panel on Climate Change, Cambridge University Press, Cambridge, UK and New York, USA, pp. 465–570.

Islam, M. S., Ueno M., and Yamashita, Y. 2010. Growth-dependent survival mechanisms during the early life of a temperate seabass (*Lateolabrax japonicus*): field test of the 'growth-mortality' hypothesis. Fisheries Oceanography **19**: 230–242.

Itoh, S., Kasai, A., Takeshige, A., Zenimoto, K., Kimura, S., Suzuki, K. W., Miyake, Y.,

Funahashi, T., Yamashita, Y., and Watanabe, Y. 2016. Circulation and haline structure of a microtidal bay in the Sea of Japan influenced by the winter monsoon and the Tsushima Warm Current. Journal of Geophysical Research: Oceans **121**: 6331–6350.

Itoh, S., Takeshige, A., Kasai, A., and Kimura, S. 2018. Modeling the coastal ecosystem complex: present situation and challenges. Fisheries Science **84**: 293–307.

Jang, D., Hwang, J. H., Park, Y. G., and Park, S. H. 2012. A study on salt wedge and river plume in the Seom-Jin River and Estuary. KSCE Journal of Civil Engineering **16**: 676–688.

Jenkins, G. P., Conron, S., and Morison, A. K. 2010. Highly variable recruitment in an estuarine fish is determined by salinity stratification and freshwater flows: implications of a changing climate. Marine Ecology Progress Series **417**: 249–261.

Jiao, N., Herndl, G. J., Hansell, D. A., Benner, R., Kattner, G., Wilhelm, S. W., Kirchman, D. L., Weinbauer, M. G., Luo, T., Chen, F., and Azam, F. 2010. Microbial production of recalcitrant dissolved organic matter: long-term carbon storage in the global ocean. Nature Reviews Microbiology **8**: 593–599.

Jiao, N., Robinson, C., Azam, F., Thomas, H., Baltar, F., Dang, H., Hardman-Mountford, N. J., Johnson, M., Kirchman, D. L., Koch, B. P., Legendre, L., Li, C., Liu, J., Luo, T., Luo, Y.-W., Mitra, A., Romanou, A., Tang, K., Wang, X., Zhang, C., and Zhang, R. 2014. Mechanisms of microbial carbon sequestration in the ocean – future research directions. Biogeosciences **11**: 5285–5306.

Kajihara, R., Komorita, T., Hamada, A., Shibanuma, S., Yamada, T., Montani, S. 2010. Possibility of direct utilization of seagrass and algae as main food resources by small gastropod, *Lacuna decorata*, in a subarctic lagoon, Hichirippu, eastern Hokkaido, Japan with stable isotope evidences of carbon and nitrogen. Plankton and Benthos Research **5**: 90–97.

Kasai, A., Fuji, T., Suzuki, K. W., and Yamashita, Y. 2018. Partial migration of juvenile temperate seabass *Lateolabrax japonicus*: a versatile survival strategy. Fisheries Science **84**: 153–162.

Kasai, A., Kurikawa, Y., Ueno, M., Robert, D., and Yamashita, Y. 2010. Salt-wedge intrusion of seawater and its implication for phytoplankton dynamics in the Yura River estuary, Japan. Estuarine, Coastal and Shelf Science **86**: 408–414.

Kawabata, K., and Defaye, D. 1994. Description of planktonic copepods from Lake Kahoku-gata, Japan. Japanese Journal of limnology **55**: 143–158.

Kelleway, J. J., Saintilan, N., Macreadie, P. I., and Ralph, P. J. 2016. Sedimentary factors are key predictors of carbon storage in SE Australian saltmarshes. Ecosystems **19**: 865–880.

Kelleway, J. J., Saintilan, N., Macreadie, P. I., Baldock, J. A., Heijnis, H., Zawadzki, A., Gadd, P., Jacobsen, G., and Ralph, P. J. 2017a. Geochemical analyses reveal the importance of environmental history for blue carbon sequestration. Journal of Geophysical Research: Biogeosciences **122**: 1789–1805.

Kelleway, J., Serrano, O., Baldock, J., Cannard, T., Lavery, P., Lovelock, C. E., Macreadie, P., Masqué, P., Saintilan, N., and Steven, A. D. L. 2017b. Technical review of opportunities for including blue carbon in the Australian Government's Emissions Reduction Fund (CSIRO, Australia).

Kelsey, H., Satake, K., Sawai, Y., Sherrod, B., Shimokawa, K., and Shishikura, M. 2006. Recurrence of postseismic coastal uplift, Kuril subduction zone, Japan. Geophysical Research Letters **33**: L13315.

Kennedy, H., and Björk, M. 2009. Seagrass meadows. In Laffoley, D., and Grimsditch, G. (Eds.), The Management of Natural Coastal Carbon Sinks, IUCN, Gland, Switzerland, pp. 23–30.

Kennedy, H., Beggins, J., Duarte, C. M., Fourqurean, J. W., Holmer, M., Marbà, N., and Middelburg, J. J. 2010. Seagrass sediments as a global carbon sink: Isotopic constraints. Global Biogeochemical Cycles **24**: GB4026.

Killick, R., and Eckley, I. A. 2014. changepoint: an R package for changepoint analysis. Journal of Statistical Software **58**: 1–19.

Kim, D., Yang, E. J., Kim, K. H., Shin, C.-W., Park, J., Yoo, S., and Hyun, J.-H. 2012. Impact of an anticyclonic eddy on the summer nutrient and chlorophyll *a* distributions in the Ulleung Basin, East Sea (Japan Sea). ICES Journal of Marine Science **69**: 23–29.

Kimmerer, W. J. 2002. Physical, biological, and management responses to variable freshwater flow into the San Francisco Estuary. Estuaries **25**: 1275–1290.

Kitayama, S., Kuma, K., Manabe, E., Sugie, K., Takata, H., Isoda, Y., Toya, K., Saitoh, S., Takagi, S., Kamei, Y., and Sakaoka, K. 2009. Controls on iron distributions in the deep water column of the North Pacific Ocean: iron(III) hydroxide solubility and marine humic-type dissolved organic matter. Journal of Geophysical Research: Oceans **114**: C08019.

Knorr, K. H. 2013. DOC-dynamics in a small headwater catchment as driven by redox fluctuations and hydrological flow paths—are DOC exports mediated by iron reduction/oxidation cycles? Biogeosciences **10**: 891–904.

Komorita, T., Kajihara, R., Tsutsumi, H., Shibanuma, S., Yamada, T., Montani, S. 2014. Food sources for *Ruditapes philippinarum* in a coastal lagoon determined by mass balance and stable isotope approaches. PLOS ONE **9**: e86732.

Kostecki C., Le Loc'h, F., Roussel, J.-M., Desroy, N., Huteau, D., Riera, P., Le Bris, H., and Le Pape, O. 2010. Dynamics of an estuarine nursery ground: the spatio-temporal relationship between the river flow and the food web of the juvenile common sole (*Solea solea*, L.) as

revealed by stable isotopes analysis. Journal of Sea Research **64**: 54-60.

Koyama, A., Kuwahara, V. S., Shibata, A., Toda, T., Kikuchi, T., and Taguchi, S. 2007. Seasonal variability in chromophoric dissolved organic matter in the Sakawa River and Sagami Bay, Japan. Limnology **8**: 211–217.

Krachler, R., Krachler, R. F., Wallner, G., Hann, S., Laux, M., Cervantes Recalde, M. F., Jirsa, F., Neubauer, E., von der Kammer, F., Hofmann, T., and Keppler, B. K. 2015. River-derived humic substances as iron chelators in seawater. Marine Chemistry **174**: 85–93.

Krause-Jensen, D., and Duarte, C. M. 2016. Substantial role of macroalgae in marine carbon sequestration. Nature Geoscience **9**: 737–742.

Krause-Jensen, D., Lavery, P., Serrano, O., Marbà, N., Masque, P., and Duarte, C. M. 2018. Sequestration of macroalgal carbon: the elephant in the Blue Carbon room. Biology Letters **14**: 20180236.

Krüger, J. P., Leifeld, J., Glatzel, S., Szidat, S., and Alewell, C. 2015. Biogeochemical indicators of peatland degradation – a case study of a temperate bog in northern Germany. Biogeosciences **12**: 2861–2871.

Kubo, A., Maeda, Y., and Kanda, J. 2017. A significant net sink for CO_2 in Tokyo Bay. Scientific Reports **7**: 44355.

Kuma, K., Katsumoto, A., Shiga, N., Sawabe, T., and Matsunaga, K. 2000. Variation of size-fractionated Fe concentrations and Fe(III) hydroxide solubilities during a spring phytoplankton bloom in Funka Bay (Japan). Marine Chemistry **71**: 111–123.

Kuwae, T., and Hori, M. (Eds.) 2019. Blue Carbon in Shallow Coastal Ecosystems: Carbon Dynamics, Policy, and Implementation, Springer, Singapore.

Kuwae, T., Kanda, J., Kubo, A., Nakajima, F., Ogawa, H., Sohma, A., and Suzumura, M. 2016. Blue carbon in human-dominated estuarine and shallow coastal systems. Ambio **45**: 290–

301.

Kuwae, T., Kanda, J., Kubo, A., Nakajima, F., Ogawa, H., Sohma, A., and Suzumura, M. 2019. CO_2 Uptake in the Shallow Coastal Ecosystems Affected by Anthropogenic Impacts. In Kuwae, T., Hori, M. (Eds.), Blue Carbon in Shallow Coastal Ecosystems: Carbon Dynamics, Policy, and Implementation, Springer, Singapore, pp.295–319.

Kuwae, T., Miyoshi, E., Hosokawa, S., Ichimi, K., Hosoya, J., Amano, T., Moriya, T., Kondoh, M., Ydenberg, R. C., Elner, R. W. 2012. Variable and complex food web structures revealed by exploring missing trophic links between birds and biofilm. Ecology Letters **15**: 347–356.

Laglera, L. M., Battaglia, G., and van den Berg, C. M. G. 2007. Determination of humic substances in natural waters by cathodic stripping voltammetry of their complexes with iron. Analytica Chimica Acta **599**: 58–66.

Laglera, L. M., and van den Berg, C. M. G. 2009. Evidence for geochemical control of iron by humic substances in seawater. Limnology and Oceanography **54**: 610–619.

Lavery, P. S., Mateo, M. Á., Serrano, O., and Rozaimi, M. 2013. Variability in the carbon storage of seagrass habitats and its implications for global estimates of blue carbon ecosystem service. PLOS ONE **8**: e73748.

Legovic, T., Zutic, V., Grzetic, Z., Cauwet, G., Precali, R., and Vilicic, D. 1994. Eutrophication in the Krka Estuary. Marine Chemistry **46**: 203–215.

Liu, S., Jiang, Z., Zhang, J., Wu, Y., Huang, X., and Macreadie, P. I. 2017. Sediment microbes mediate the impact of nutrient loading on blue carbon sequestration by mixed seagrass meadows. Science of the Total Environment **599–600**: 1479–1484.

Liu, X., and Millero, F. J. 2002. The solubility of iron in seawater. Marine Chemistry 77:43–54.

Liu, Z., Zhang, L., Cai, W.-J., Wang, L., Xue, M., Zhang, X. 2014. Removal of dissolved

inorganic carbon in the Yellow River Estuary. Limnology and Oceanography **59**: 413–426.

Lønborg, C., and Søndergaard, M. 2009. Microbial availability and degradation of dissolved organic carbon and nitrogen in two coastal areas. Estuarine, Coastal and Shelf Science **81**: 513–520.

Lorenzen, C. J. 1967. Determination of chlorophyll and pheo-pigments: spectrophotometric equations. Limnology and Oceanography **12**: 343–346.

Lovelock, C. E., Cahoon, D. R., Friess, D. A., Guntenspergen, G. R., Krauss, K. W., Reef, R., Rogers, K., Saunders, M. L., Sidik, F., Swales, A., Saintilan, N., Thuyen, L. X., and Triet, T. 2015. The vulnerability of Indo-Pacific mangrove forests to sea-level rise. Nature **526**: 559–563.

Macreadie, P. I., Allen, K., Kelaher, B. P., Ralph, P. J., and Skilbeck, C. G. 2012. Paleoreconstruction of estuarine sediments reveal human-induced weakening of coastal carbon sinks. Global Change Biology **18**: 891–901.

Macreadie, P. I., Hughes, A. R., and Kimbro, D. L. 2013. Loss of 'blue carbon' from coastal salt marshes following habitat disturbance. PLOS ONE **8**: e69244.

Macreadie, P. I., Baird, M. E., Trevathan-Tackett, S. M., Larkum, A. W. D., and Ralph, P. J. 2014. Quantifying and modelling the carbon sequestration capacity of seagrass meadows – A critical assessment. Marine Pollution Bulletin **83**: 430–439.

Macreadie, P. I., Trevathan-Tackett, S. M., Skilbeck, C. G., Sanderman, J., Curlevski, N., Jacobsen, G., and Seymour, J. R. 2015. Losses and recovery of organic carbon from a seagrass ecosystem following disturbance. Proceedings of the Royal Society B **282**: 20151537.

Macreadie, P. I., Nielsen, D. A., Kelleway, J. J., Atwood, T. B., Seymour, J. R., Petrou, K.,

Connolly, R. M., Thomson, A. C. G., Trevathan-Tackett, S. M., and Ralph, P. J. 2017. Can we manage coastal ecosystems to sequester more blue carbon? Frontiers in Ecology and the Environment **15**: 206–213.

Magni, P., Como, S., Kamijo, A., and Montani, S. 2017. Effects of *Zostera marina* on the patterns of spatial distribution of sediments and macrozoobenthos in the boreal lagoon of Furen (Hokkaido, Japan). Marine Environmental Research **131**: 90–102.

Maher, D. T., and Eyre, B. D. 2012. Carbon budgets for three autotrophic Australian estuaries: Implications for global estimates of the coastal air-water CO_2 flux. Global Biogeochemical Cycles **26**: GB1032.

Maher, D. T., Santos, I. R., Schulz, K. G., Call, M., Jacobsen, G. E., and Sanders, C. J. 2017. Blue carbon oxidation revealed by radiogenic and stable isotopes in a mangrove system. Geophysical Research Letters **44**: 4889–4896.

Maksymowska, D., Richard, P., Piekarek-Jankowska, H., and Riera, P. 2000. Chemical and isotopic composition of the organic matter sources in the Gulf of Gdansk (southern Baltic Sea). Estuarine, Coastal and Shelf Science **51**: 585–598.

Maldonado, M. T., and Price, N. M. 1999. Utilization of iron bound to strong organic ligands by plankton communities in the subarctic Pacific Ocean. Deep-Sea Research Part II **46**: 2447–2473.

Mallin, M. A., Paerl, H. W., Rudek, J., and Bates, P. W. 1993. Regulation of estuarine primary production by watershed rainfall and river flow. Marine Ecology Progress Series **93**: 199–203.

Malone, T. C., Crocker, L. H., Pike, S. E., Wendler, B. W. 1988. Influences of river flow on the dynamics of phytoplankton production in a partially stratified estuary. Marine Ecology Progress Series **48**: 235–249.

Marbà, N., Arias-Ortiz, A., Masqué, P., Kendrick, G. A., Mazarrasa, I., Bastyan, G. R., Garcia-Orellana, J., and Duarte, C. M. 2015. Impact of seagrass loss and subsequent revegetation on carbon sequestration and stocks. Journal of Ecology **103**: 296–302.

Martin, J. H., and Fitzwater, S. E. 1988. Iron deficiency limits phytoplankton growth in the northeast Pacific subarctic. Nature **331**: 341–343.

Martin, J. H., Gordon, R. M., Fitzwater, S., and Broenkow, W. W. 1989. Vertex: phytoplankton/iron studies in the Gulf of Alaska. Deep Sea Research Part A **36**: 649–680.

Martin, J. H., Coale, K. H., Johnson, K. S., Fitzwater, S. E., Gordon, R. M., Tanner, S. J., Hunter, C. N., Elrod, V. A., Nowicki, J. L., Coley, T. L., Barber, R. T., Lindley, S., Watson, A. J., Vanscoy, K., Law, C. S., Liddicoat, M. I., Ling, R., Stanton, T., Stockel, J., Collins, C., Anderson, A., Bidigare, R., Ondrusek, M., Latasa, M., Millero, F. J., Lee, K., Yao, W., Zhang, J. Z., Friederich, G., Sakamoto, C., Chavez, F., Buck, K., Kolber, Z., Greene, R., Falkowski, P., Chisholm, S. W., Hoge, F., Swift, R., Yungel, J., Turner, S., Nightingale, P., Hatton, A., Liss, P., and Tindale, N. W. 1994. Testing the iron hypothesis in ecosystems of the equatorial Pacific-Ocean. Nature **371**: 123–129.

Mateo, M. A., Romero, J., Pérez, M., Littler, M. M., and Littler, D. S. 1997. Dynamics of millenary organic deposits resulting from the growth of the Mediterranean seagrass *Posidonia oceanica*. Estuarine, Coastal and Shelf Science **44**: 103–110.

Mayer, L. M. 1982. Retention of riverine iron in estuaries. Geochimica et Cosmochimica Acta **46**: 1003–1009.

McFadden, D. 1973. Conditional logit analysis of qualitative choice behavior. In Zarembka, P. (Eds.), Frontiers in Econometrics, Academic Press, New York, pp. 105–142.

McKee, K. L., Cahoon, D. R., and Feller, I. C. 2007. Caribbean mangroves adjust to rising sea level through biotic controls on change in soil elevation. Global Ecology and

Biogeography **16**: 545–556.

McLeod, E., Chmura, G. L., Bouillon, S., Salm, R., Björk, M., Duarte, C. M., Lovelock, C. E., Schlesinger, W. H., and Silliman, B. R. 2011. A blueprint for blue carbon: toward an improved understanding of the role of vegetated coastal habitats in sequestering CO_2. Frontiers in Ecology and the Environment **9**: 552–560.

Michel, P., Boutier, B., and Chiffoleau, J. F. 2000. Net fluxes of dissolved arsenic, cadmium, copper, zinc, nitrogen and phosphorus from the Gironde Estuary (France): seasonal variations and trends. Estuarine, Coastal and Shelf Science **51**: 451–462.

MEA (Millennium Ecosystem Assessment). 2005. Millennium Ecosystem Assessment: synthesis report. Island Press, Washington, DC.

Minami, T. 1982. The early life history of a flounder *Paralichthys olivaceus*. Bulletin of the Japanese Society of Scientific Fisheries **48**: 1581–1588. (in Japanese with English abstract)

Miwa, H., and Ikeno, H. 2008. Numerical analysis of tidal current and water quality in stratified field on summer in Maizuru Bay. Annual Journal of Hydraulic Engineering **52**: 1387–1392. (in Japanese with English abstract)

Miyajima, T., and Hamaguchi, M. 2019. Carbon Sequestration in Sediment as an Ecosystem Function of Seagrass Meadows. In Kuwae, T., Hori, M. (Eds.), Blue Carbon in Shallow Coastal Ecosystems: Carbon Dynamics, Policy, and Implementation, Springer, Singapore, pp.33–71.

Miyajima, T., Hori, M., Hamaguchi, M., Shimabukuro, H., and Yoshida, G. 2017. Geophysical constraints for organic carbon sequestration capacity of *Zostera marina* seagrass meadows and surrounding habitats. Limnology and Oceanography **62**: 954–972.

Montani, S., Managaki, Y., and Shibanuma, S. 2011. The structural changes in biological

productivity due to progress of dairy in Lake Furen. Bulletin on Coastal Oceanography **49**: 59–67. (in Japanese with English abstract)

Morris, J., Sundareshwar, P., and Nietch, C. 2002. Responses of coastal wetlands to rising sea level. Ecology **83**: 2869–2877.

Mudd, S. M., Howell, S. M., and Morris, J. T. 2009. Impact of dynamic feedbacks between sedimentation, sea-level rise, and biomass production on near-surface marsh stratigraphy and carbon accumulation. Estuarine, Coastal and Shelf Science **82**: 377–389.

Murakami, T., Isaji, C., Kuroda, N., Yoshida, K., and Haga, H. 1992. Potamoplanktonic diatoms in the Nagara River; Flora, population dynamics and influences on water quality. Japanese Journal of Limnology **53**: 1–12.

Murakami, T., Isaji, C., Kuroda, N., Yoshida, K., Haga, H., Watanabe, Y., and Saijo, Y. 1994. Development of potamoplanktonic diatoms in downreaches of Japanese rivers. Japanese Journal of Limnology **55**: 13–21.

Murrell, M. C., Hagy III, J. D., Lores, E. M., and Greene, R. M. 2007. Phytoplankton production and nutrient distributions in a subtropical estuary: Importance of freshwater flow. Estuaries and Coasts **30**: 390–402.

Muylaert, K., and Sabbe, K. 1999. Spring phytoplankton assemblages in and around the maximum turbidity zone of the estuaries of the Elbe (Germany), the Schelde (Belgium/The Netherlands) and the Gironde (France). Journal of Marine Systems **22**: 133–149.

Nagao, S., Terashima, M., Seki, O., Takata, H., Kawahigashi, M., Kodama, H., Kim, V. I., Shesterkin, V. P., Leveshina, S. I., and Makhinov, A. N. 2010. Biogeochemical behavior of iron in the lower Amur River and Amur-Liman. In Shiraiwa, T. (Eds.), Report on Amur-Okhotsk Project (No. 6). Amur-Okhotsk Project, Kyoto, pp 41–50.

Nagao, S., Yan, B., Kim, V. I., Shesterkin, V. P., Leveshina, S. I., Yoh, M., Suzuki, T., Kodama, H., Terashima, M., Seki, O., and Makhinov, A. N. 2014. Water chemistry of the Middle Amur River. In Haruyama, S., Shiraiwa, T. (Eds.), Environmental change and the social response in the Amur River Basin. Springer, Berlin, pp 105–127.

Nagata, T. 2008. Organic matter–bacteria interactions in seawater. In Kirchman, D. L. (Eds.), Microbial Ecology of the Oceans, Second Edition, John Wiley & Sons, New York, USA, pp. 207–242.

Naito, K., Imai, I., and Nakahara, H. 2008. Complexation of iron by microbial siderophores and effects of iron chelates on the growth of marine microalgae causing red tides. Phycological Research **56**: 58–67.

Nakayama, Y., Fujita, S., Kuma, K., and Shimada, K. 2011. Iron and humic-type fluorescent dissolved organic matter in the Chukchi Sea and Canada Basin of the western Arctic Ocean. Journal of Geophysical Research: Oceans **116**: C07031.

Nanayama, F., Satake, K., Furukawa, R., Shimokawa, K., Atwater, B. F., Shigeno, K., and Yamaki, S. 2003. Unusually large earthquakes inferred from tsunami deposits along the Kuril trench. Nature **424**: 660–663.

Nellemann, C., Corcoran, E., Duarte, C. M., Valdes, L., DeYoung, C., Fonseca, L., and Grimsditch, G. 2009. Blue Carbon. A Rapid Response Assessment. United Nations Environmental Programme, GRID-Arendal, Birkeland Trykkeri AS, Birkeland.

Nishimura, S., Kuma, K., Ishikawa, S., Omata, A., and Saitoh, S. 2012. Iron, nutrients, and humic-type fluorescent dissolved organic matter in the northern Bering Sea shelf, Bering Strait, and Chukchi Sea. Journal of Geophysical Research: Oceans **117**: C02025.

North, E. W., and Houde, E. D. 2001. Retention of white perch and striped bass larvae: biological-physical interactions in Chesapeake Bay estuarine turbidity maximum.

Estuaries **24**: 756–769.

North, E. W., and Houde, E. D. 2003. Linking ETM physics, zooplankton prey, and fish early life histories to striped bass *Morone saxatilis* and white perch *M. americana* recruitment. Marine Ecology Progress Series **260**: 219–236.

North, E. W., Houde, E. D. 2006. Retention mechanisms of white perch (*Morone americana*) and striped bass (*Morone saxatilis*) early-life stages in an estuarine turbidity maximum: an integrative fixed-location and mapping approach. Fisheries Oceanography **15**: 429–450.

Nowostawska, U., Kri, J. P., and Hunter, K. A. 2008. Aggregation of riverine colloidal iron in estuaries: a kinetic study using stopped-flow mixing. Marine Chemistry **110**: 205–210.

Omweri, J. O., Suzuki, K. W., Edouard, L., Yokoyama, H., and Yamashita, Y. 2018. Seasonality and occurrence of the dominant mysid *Neomysis awatschensis* (Brandt, 1851) in the Yura River estuary, central Sea of Japan. Estuarine, Coastal and Shelf Science **211**: 188–198.

Opsahl, S., and Benner, R. 1993. Decomposition of senescent blades of the seagrass *Halodule wrightii* in a subtropical lagoon. Marine Ecology Progress Series **94**: 191–205.

Oreska, M. P. J., McGlathery, K. J., and Porter, J. H. 2017. Seagrass blue carbon spatial patterns at the meadow-scale. PLOS ONE **12**: e0176630.

Orth, R. J., Carruthers, T. J. B., Dennison, W. C., Duarte, C. M., Fourqurean, J. W., Heck, K. L., Hughes, A. R., Kendrick, G. A., Kenworthy, W. J., Olyarnik, S., Short, F. T, Waycott, M., and Williams, S. L. 2006. A global crisis for seagrass ecosystems. BioScience **56**: 987–996.

Paerl, H. W., Rudek, J., and Mallin, M. A. 1990. Stimulation of phytoplankton production in coastal waters by natural rainfall inputs: Nutritional and trophic implications. Marine Biology **107**: 247–254.

Para, J., Charrière, B., Matsuoka, A., Miller, W. L., Rontani, J. F., and Sempéré, R. 2013. UV/PAR radiation and DOM properties in surface coastal waters of the Canadian shelf of the Beaufort Sea during summer 2009. Biogeosciences **10**: 2761–2774.

Parnell, A. C., Inger, R., Bearhop, S., Jackson, A. L. 2010. Source partitioning using stable isotopes: Coping with too much variation. PLOS ONE **5**: e9672.

Pendleton, L., Donato, D. C., Murray, B. C., Crooks, S., Jenkins, W. A., Sifleet, S., Craft, C., Fourqurean, J. W., Kauffman, J. B., Marbà, N., Megonigal, P., Pidgeon, E., Herr, D., Gordon, D., and Baldera, A. 2012. Estimating global "blue carbon" emissions from conversion and degradation of vegetated coastal ecosystems. PLOS ONE **7**: e43542.

Perdue, E. M., and Koprivnjak, J. F. 2007. Using the C/N ratio to estimate terrigenous inputs of organic matter to aquatic environments. Estuarine, Coastal and Shelf Science **73**: 65–72.

Pérez, A., Machado, W., Gutierrez, D., Stokes, D., Sanders, L., Smoak, J. M., Santos, I., and Sanders, C. J. 2017. Changes in organic carbon accumulation driven by mangrove expansion and deforestation in a New Zealand estuary. Estuarine, Coastal and Shelf Science **192**: 108–116.

R Core Team. 2017. R: a language and environment for statistical computing. R Foundation for Statistical Computing, Vienna, Austria, https://www.R-project.org/ (2017).

Redfield, A. C., Ketchum, B. H., and Richard, F. A. 1963. The influence of organisms on the composition of the sea water. In Hill, M. N. (Eds), The Sea, Vol. 2. Wiley, New York, pp. 26–77.

Regnier, P., Friedlingstein, P., Ciais, P., Mackenzie, F. T., Gruber, N., Janssens, I. A., Laruelle, G. G., Lauerwald, R., Luyssaert, S., Andersson, A. J., Arndt, S., Arnosti, C., Borges, A. V., Dale, A. D., Gallego-Sala, A., Goddéris, Y., Goossens, N., Hartmann, J., Heinze, C., Ilyina, T., Joos, F., LaRowe, D. E., Leifeld, J., Meysman, F. J. R., Munhoven, G.,

Raymond, P. A., Spahni, R., Suntharalingam. P., and Thullner, M. 2013. Anthropogenic perturbation of the carbon fluxes from land to ocean. Nature Geoscience **6**: 597–607.

Reimer, P. J., Bard, E., Bayliss, A., Beck, J. W., Blackwell, P. G., Ramsey, C. B., Buck, C. E., Cheng, H., Edwards, R. L., Friedrich, M., Grootes, P. M., Guilderson, T. P., Haflidason, H., Hajdas, I., Hatté, C., Heaton, T. J., Hoffmann, D. L., Hogg, A. G., Hughen, K. A., Kaiser, K. F., Kromer, B., Manning, S. W., Niu, M., Reimer, R. W., Richards, D. A., Scott, E. M., Southon, J. R., Staff, R. A., Turney, C. S. M., and van der Plicht, J. 2013. IntCal13 and Marine13 radiocarbon age calibration curves 0–50,000 years cal BP. Radiocarbon **55**: 1869–1887.

Ricart, A. M., York, P. H., Rasheed, M. A., Pérez, M., Romero, J., Bryant, C. V., and Macreadie, P. I. 2015. Variability of sedimentary organic carbon in patchy seagrass landscapes. Marine Pollution Bulletin **100**: 476–482.

Romera-Castillo, C., Sarmento, H., Alvarez-Salgado, X. A., Gasol, J. M., and Marrase, C. 2010. Production of chromophoric dissolved organic matter by marine phytoplankton. Limnology and Oceanography **55**: 446–454.

Rontani, J. F., Vaultier, F., and Bonin, P. 2014. Biotic and abiotic degradation of marine and terrestrial higher plant material in intertidal surface sediments from Arcachon Bay (France): a lipid approach. Marine Chemistry **158**: 69–79.

Saadi, I., Borisover, M., Armon, R., and Laor, Y. 2006. Monitoring of effluent DOM biodegradation using fluorescence, UV and DOC measurements. Chemosphere **63**: 530–539.

Saba, V. S., Hyde, K. J. W., Rebuck, N. D., Friedland, K. D., Hare, J. A., Kahru M., and Fogarty, M. J. 2015. Physical associations to spring phytoplankton biomass interannual variability in the U.S. Northeast Continental Shelf. Journal of Geophysical Research: Biogeosciences

120: 205–220.

Samper-Villarreal, J., Lovelock, C. E., Saunders, M. I., Roelfsema, C., and Mumby, P. J. 2016. Organic carbon in seagrass sediments is influenced by seagrass canopy complexity, turbidity, wave height, and water depth. Limnology and Oceanography **61**: 938–952.

Sato, T., Miyajima, T., Ogawa, H., Umezawa, Y., and Koike, I. 2006. Temporal variability of stable carbon and nitrogen isotopic composition of size-fractionated particulate organic matter in the hypertrophic Sumida River Estuary of Tokyo Bay, Japan. Estuarine, Coastal and Shelf Science **68**: 245–258.

Savoye, N., David, V., Morisseau, F., Etcheber, H., Abril, G., Billy, I., Charlier, K., Oggian, G., Derriennic, H., and Sautour, B. 2012. Origin and composition of particulate organic matter in a macrotidal turbid estuary: The Gironde Estuary, France. Estuarine, Coastal and Shelf Science **108**: 16–28.

Sawai, Y., Horton, B. P., and Nagumo, T. 2004. The development of a diatom-based transfer function along the Pacific coast of eastern Hokkaido, northern Japan—an aid in paleoseismic studies of the Kuril subduction zone. Quaternary Science Reviews **23**: 2467–2483.

Sawai, Y., Kamataki, T., Shishikura, M., Nasu, H., Okamura, Y., Satake, K., Thomson, K. H., Matsumoto, D., Fujii, Y., Komatsubara, J., and Aung, T. T. 2009. Aperiodic recurrence of geologically recorded tsunamis during the past 5500 years in eastern Hokkaido, Japan. Journal of Geophysical Research: Solid Earth **114**: B01319.

Scharler, U. M., and Baird, D. 2005. A comparison of selected ecosystem attributes of three South African estuaries with differing freshwater inflow regimes, using network analysis. Journal of Marine Systems **56**: 283–308.

Serrano, O., Lavery, P. S., Rozaimi, M., and Mateo, M. Á. 2014. Influence of water depth on the

carbon sequestration capacity of seagrasses. Global Biogeochemical Cycles **28**: 950–961.

Serrano, O., Lavery, P. S., Duarte, C. M., Kendrick, G. A., Calafat, A., York, P. H., Steven, A., and Macreadie, P. I. 2016. Can mud (silt and clay) concentration be used to predict soil organic carbon content within seagrass ecosystems? Biogeosciences **13**: 4915–4926.

Shields, M. R., Bianchi, T. S., Mohrig, D., Hutchings, J. A., Kenney, W. F., Kolker, A. S., and Curtis, J. H. 2017. Carbon storage in the Mississippi River delta enhanced by environmental engineering. Nature Geoscience **10**: 846–851.

Shiozaki, T., Ito, S.-I., Takahashi, K., Saito, H., Nagata, T., and Furuya, K. 2014. Regional variability of factors controlling the onset timing and magnitude of spring algal blooms in the northwestern North Pacific. Journal of Geophysical Research: Oceans **119**: 253–265.

Shoji, J., North, E. W., and Houde, E. D. 2005. The feeding ecology of *Morone americana* larvae in the Chesapeake Bay estuarine turbidity maximum: the influence of physical conditions and prey concentrations. Journal of Fish Biology **66**: 1328–1341.

Sholkovitz, E. R., Boyle, E. A., and Price, N. B. 1978. The removal of dissolved humic acids and iron during estuarine mixing. Earth and Planetary Science Letters **40**: 130–136.

Short, F. T., Kosten, S., Morgan, P. A., Malone, S., and Moore, G. E. 2016. Impacts of climate change on submerged and emergent wetland plants. Aquatic Botany **135**: 3–17.

Sierra, J. P., Sanchez-Arcilla, A., Gonzalez del Rio, J., Flos, J., Movellan, E., Mösso, C., Martinez, R., Rodilla, M., Falco, S., and Romero, I. 2002. Spatial distribution of nutrients in the Ebro estuary and plume. Continental Shelf Research **22**: 361–378.

Sierra, J. P., Sanchez-Arcila, A., Figueras, P. A., Gonzalez del Rio, J., Rassmussen, E. K., and Mösso, C. 2004. Effects of discharge reductions on salt wedge dynamics of the Ebro River. River Research and Applications **20**: 61–77.

Smith Jr., W. O., and Demaster, D. J. 1996. Phytoplankton biomass and productivity in the

Amazon River plume: correlation with seasonal river discharge. Continental Shelf Research **16**: 291–319.

Sohma, A., Shibuki, H., Nakajima, F., Kubo, A., and Kuwae, T. 2018. Modeling a coastal ecosystem to estimate climate change mitigation and a model demonstration in Tokyo Bay. Ecological Modelling **384**: 261–289.

Sohrin, Y., Urushihara, S., Nakatsuka, S., Kono, T., Higo, E., Minami, T., Norisuye, K., and Umetani, S. 2008. Multielemental determination of GEOTRACES key trace metals in seawater by ICPMS after preconcentration using an ethylenediaminetriacetic acid chelating resin. Analytical Chemistry **80**: 6267–6273.

Stedmon, C. A., Markager, S., and Bro, R. 2003. Tracing dissolved organic matter in aquatic environments using a new approach to fluorescence spectroscopy. Marine Chemistry **82**: 239–254.

Stedmon, C. A., and Bro, R. 2008. Characterizing dissolved organic matter fluorescence with parallel factor analysis: a tutorial. Limnology and Oceanography: Methods **6**: 572–579.

Stolpe, B., and Hassellöv, M. 2007. Changes in size distribution of fresh water nanoscale colloidal matter and associated elements on mixing with seawater. Geochimica et Cosmochimica Acta **71**: 3292–3301.

Strickland, J. D. H., and Parsons, T. R. 1972. A practical handbook of seawater analysis. Bulletin of the Fisheries Research Board of Canada **167**: 201–203.

Sugimoto, R., Kasai, A., Yamao, S., Fujiwara, T., and Kimura, T. 2004. Variation in particulate organic matter accompanying changes of river discharge in Ise Bay. Bulletin of the Japanese Society of Fisheries Oceanography **68**: 142–150. (in Japanese with English abstract)

Sugimoto, R., Kasai, A., Miyajima, T., and Fujita, K. 2010. Modeling phytoplankton production

in Ise Bay, Japan: Use of nitrogen isotopes to identify dissolved inorganic nitrogen sources. Estuarine, Coastal and Shelf Science **86**: 450–466.

Suzuki, K., Hattori-Saito, A., Sekiguchi, Y., Nishioka, J., Shigemitsu, M., Isada, T., and Liu, H. 2014. Spatial variability in iron nutritional status of large diatoms in the Sea of Okhotsk with special reference to the Amur River discharge. Biogeosciences **11**: 2503–2517.

Suzuki, K. W., Kasai, A., Isoda, T., Nakayama, K., and Tanaka, M. 2008. Distinctive stable isotope ratios in important zooplankton species in relation to estuarine salinity gradients: Potential tracer of fish migration. Estuarine, Coastal and Shelf Science **78**: 541–550.

Tagliabue, A., Bowie, A. R., Boyd, P. W., Buck, K. N., Johnson, K. S., and Saito, M. A. 2017. The integral role of iron in ocean biogeochemistry. Nature **543**: 51–59.

Takata, H., Kuma, K., Iwade, S., Yamajyoh, Y., Yamaguchi, A., Takagi, S., Sakaoka, K., Yamashita, Y., Tanoue, E., Midorikawa, T., Kimura, K., and Nishioka, J. 2004. Spatial variability of iron in the surface water of the northwestern North Pacific Ocean. Marine Chemistry **86**: 139–157.

Takata, H., Kuma, K., Iwade, S., Isoda, Y., Kuroda, H., and Senjyu, T. 2005. Comparative vertical distributions of iron in the Japan Sea, the Bering Sea, and the western North Pacific Ocean. Journal of Geophysical Research: Oceans **110**: C07004.

Takeno, K., Hamanaka, Y., and Okano, I. 2008. Differences in growth of young Japanese flounder *Paralichthys olivaceus* in two semi-enclosed bays of the Sea of Japan, Kyoto. Aquaculture Science **56**: 513–522.

Tanaya, T., Watanabe, K., Yamamoto, S., Hongo, C., Kayanne, H., and Kuwae, T. 2018. Contributions of the direct supply of belowground seagrass detritus and trapping of suspended organic matter to the sedimentary organic carbon stock in seagrass meadows. Biogeosciences **15**: 4033–4045.

Tani, H., Nishioka, J., Kuma, K., Takata, H., Yamashita, Y., Tanoue, E., and Midorikawa, T. 2003. Iron(III) hydroxide solubility and humic-type fluorescent organic matter in the deep water column of the Okhotsk Sea and the northwestern North Pacific Ocean. Deep-Sea Research Part I **50**: 1063–1078.

TEEB. 2010. The Economics of Ecosystems and Biodiversity Ecological and Economic Foundations. London and Washington, Earthscan.

Theuerkauf, E. J., and Rodriguez, A. B. 2017. Placing barrier-island transgression in a blue-carbon context. Earth's Future **5**: 789–810.

Tokoro, T., Hosokawa, S., Miyoshi, E., Tada, K., Watanabe, K., Montani, S., Kayanne, H., and Kuwae, T. 2014. Net uptake of atmospheric CO_2 by coastal submerged aquatic vegetation. Global Change Biology **20**: 1873–1884.

Tokoro, T., Watanabe, K., Tada, K., and Kuwae, T. 2019. Air–Water CO_2 Flux in Shallow Coastal Waters: Theory, Methods, and Empirical Studies. In Kuwae, T., Hori, M. (Eds.), Blue Carbon in Shallow Coastal Ecosystems: Carbon Dynamics, Policy, and Implementation, Springer, Singapore, pp.153–184.

Trevathan-Tackett, S. M., Kelleway, J., Macreadie, P. J., Beardall, J., Ralph, P., and Bellgrove, A. 2015. Comparison of marine macrophytes for their contributions to blue carbon sequestration. Ecology **96**: 3043–3057.

Trevathan-Tackett, S. M., Macreadie, P. I., Sanderman, J., Baldock, J., Howes, J. M., and Ralph, P. J. 2017. A Global Assessment of the Chemical Recalcitrance of Seagrass Tissues: Implications for Long-Term Carbon Sequestration. Frontiers in Plant Science **8**: 925.

Tseng, Y.-F, Lin, J., Dai, M., and Kao, S.-J. 2014. Joint effect of freshwater plume and coastal upwelling on phytoplankton growth off the Changjiang River. Biogeosciences **11**: 409–423.

Tsuji, Y., and Montani, S. 2017. Spatial variability in an estuarine phytoplankton and suspended microphytobenthos community. Plankton and Benthos Research **12**: 190–200.

Twomey, L., and John, J. 2001. Effects of rainfall and salt-wedge movement on phytoplankton succession in the Swan-Canning Estuary, Western Australia. Hydrological Processes **15**: 2655–2669.

Ueda, H. 1991. Horizontal distribution of planktonic copepods in inlet waters. Proceedings of the Fourth International Conference on Copepoda, Karuizawa, Japan, 16-20 September 1990. Plankton Society of Japan, Hiroshima, pp. 143–160.

Ueda, H., Terao, A., Tanaka, M., Hibino, M., and Islam, M. S. 2004. How can river-estuarine planktonic copepods survive river floods? Ecological Research **19**: 625–632.

Uye, S., Shimazu, T., Yamamuro, M., Ishitobi, Y., and Kamiya, H. 2000. Geographical and seasonal variations in mesozooplankton abundance and biomass in relation to environmental parameters in Lake Shinji – Ohashi River – Lake Nakaumi brackish-water system, Japan. Journal of Marine Systems **26**: 193–207.

Van Mooy, B. A. S., Keil, R. G., and Devol, A. H. 2002. Impact of suboxia on sinking particulate organic carbon: Enhanced carbon flux and preferential degradation of amino acids via denitrification. Geochimica et Cosmochimica Acta **66**: 457–465.

Vidjak, O., Bojanić, N., Kušplić, G., Grbec, B., Glandan, Z. N., Matijević, S., and Brautović, I. 2009. Population structure and abundance of zooplankton along the Krka river estuary in spring 2006. Acta Adriatica **50**: 45–58.

Vraspir, J. M., and Butler, A. 2009. Chemistry of marine ligands and siderophores. Annual Review of Marine Science **1**: 43–63.

Wada, S., Aoki, M. N., Mikami, A., Komatsu, T., Tsuchiya, Y., Sato, T., Shinagawa, H., and Hama, T. 2008. Bioavailability of macroalgal dissolved organic matter in seawater.

Marine Ecology Progress Series **370**: 33–44.

Watanabe, K., Kasai, A., Antonio, E. S., Suzuki, K., Ueno, M., and Yamashita, Y. 2014. Influence of salt-wedge intrusion on ecological processes at lower trophic levels in the Yura River estuary, Japan. Estuarine, Coastal and Shelf Science **139**: 67–77.

Watanabe, K., and Kuwae, T. 2015a. How organic carbon derived from multiple sources contributes to carbon sequestration processes in a shallow coastal system? Global Change Biology **21**: 2612–2623.

Watanabe, K., and Kuwae, T. 2015b. Radiocarbon isotopic evidence for assimilation of atmospheric CO_2 by the seagrass *Zostera marina*. Biogeosciences **12**: 6251–6258.

Watanabe, K., Kasai, A., Fukuzaki, K., Ueno, M., and Yamashita, Y. 2017. Estuarine circulation-driven entrainment of oceanic nutrients fuels coastal phytoplankton in an open coastal system in Japan. Estuarine, Coastal and Shelf Science **184**: 126–137.

Watanabe, Y., Kawamura, T., and Yamashita, Y. 2018. Introduction: the coastal ecosystem complex as a unit of structure and function of biological productivity in coastal areas. Fisheries Science **84**: 149–152.

WBCSD. 2011. Guide to Corporate Ecosystem Valuation. Atar Roto Presse SA, Switzerland.

Weishaar, J. L., Aiken, G. R., Bergamaschi, B. A., Fram, M. S., Fujii, R., and Mopper, K. 2003. Evaluation of specific ultraviolet absorbance as an indicator of the chemical composition and reactivity of dissolved organic carbon. Environmental Science and Technology **37**: 4702–4708.

Weston, N. B., Giblin, A. E., Banta, G. T., Hopkinson, C. S., Tucker, J. 2010a. The effects of varying salinity on ammonium exchange in estuarine sediments of the Parker River, Massachusetts. Estuaries and Coasts **33**: 985–1003.

Weston, N. B., Vile, M. A., Neubauer, S. C., and Velinsky, D. J. 2010b. Accelerated microbial

organic matter mineralization following salt-water intrusion into tidal freshwater marsh soils. Biogeochemistry **102**: 135–151.

Williams, J., Hindell, J. S., Swearer, S. E., and Jenkins, G. P. 2012. Influence of freshwater flows on the distribution of eggs and larvae of black bream *Acanthopagrus butcheri* within a drought-affected estuary. Journal of Fish Biology **80**: 2281–2301.

Woodroffe, C. D., Rogers, K., McKee, K. L., Lovelock, C. E., Mendelssohn, I. A., and Saintilan, N. 2016. Mangrove sedimentation and response to relative sea-level rise. Annual Review of Marine Science **8**: 243–266.

Yamamoto, T., Yoshikawa, S., Hashimoto, T., Takasugi, Y., and Matsuda, O. 2000. Estuarine circulation process in the northern Hiroshima Bay, Japan. Bulletin on Coastal Oceanography **37**: 111–118. (in Japanese with English abstract)

Yamashita, Y., and Tanoue, E. 2003. Chemical characterization of protein-like fluorophores in DOM in relation to aromatic amino acids. Marine Chemistry **82**: 255–271.

Yamashita, Y., Jaffé, R., Maie, N., and Tanoue, E. 2008. Assessing the dynamics of dissolved organic matter (DOM) in coastal environments by excitation emission matrix fluorescence and parallel factor analysis (EEM-PARAFAC). Limnology and Oceanography **53**: 1900–1908.

Yamashita, Y., Cory, R. M., Nishioka, J., Kuma, K., Tanoue, E., and Jaffé, R. 2010. Fluorescence characteristics of dissolved organic matter in the deep waters of the Okhotsk Sea and the northwestern North Pacific Ocean. Deep-Sea Research Part II **57**: 1478–1485.

Yang, R., Su, H., Qu, S., and Wang, X. 2017. Capacity of humic substances to complex with iron at different salinities in the Yangtze River estuary and East China Sea. Scientific Reports **7**: 1381.

Yoshioka, T., Mostofa, K. M. G., Konohira, E., Tanoue, E., Hayakawa, K., Takahashi, M., Ueda,

S., Katsuyama, M., Khodzher, T., Bashenkhaeva, N., Korovyakova, I., Sorokovikova, L., and Gorbunova, L. 2007. Distribution and characteristics of molecular size fractions of freshwater-dissolved organic matter in watershed environments: its implication to degradation. Limnology **8**: 29–44.

Zedler, J. B. 2003. Wetlands at your service: reducing impacts of agriculture at the watershed scale. Frontiers in Ecology and the Environment **1**: 65–72.

Zeitzschel, B. 1970. The quantity, composition and distribution of suspended particulate matter in the Gulf of California. Marine Biology **7**: 305–318.

Zonneveld, K. A. F., Versteegh, G. J. M., Kasten, S., Eglinton, T. I., Emeis, K.-C., Huguet, C., Koch, B. P., de Lange, G. J., de Leeuw, J. W., Middelburg, J. J., Mollenhauer, G., Prahl, F. G., Rethemeyer, J., and Wakeham, S. G. 2010. Selective preservation of organic matter in marine environments; processes and impact on the sedimentary record. Biogeosciences **7**: 483–511.

Zurbrügg, R., Suter, S., Lehmann, M. F., Wehrli, B., and Senn, D. B. 2013. Organic carbon and nitrogen export from a tropical dam-impacted floodplain system. Biogeosciences **10**: 23–38.

Zutic, V., and Legovic, T. 1987. A film of organic matter at the fresh-water/sea-water interface of an estuary. Nature **328**: 612–614.

Appendix

Table S3-1. Results of a generalized linear model to estimate extinction coefficients (k) from turbidity.

Coefficients	Estimate	Standard error	p
Intercept	0.162	0.009	<0.001
Turbidity	0.108	0.007	<0.001

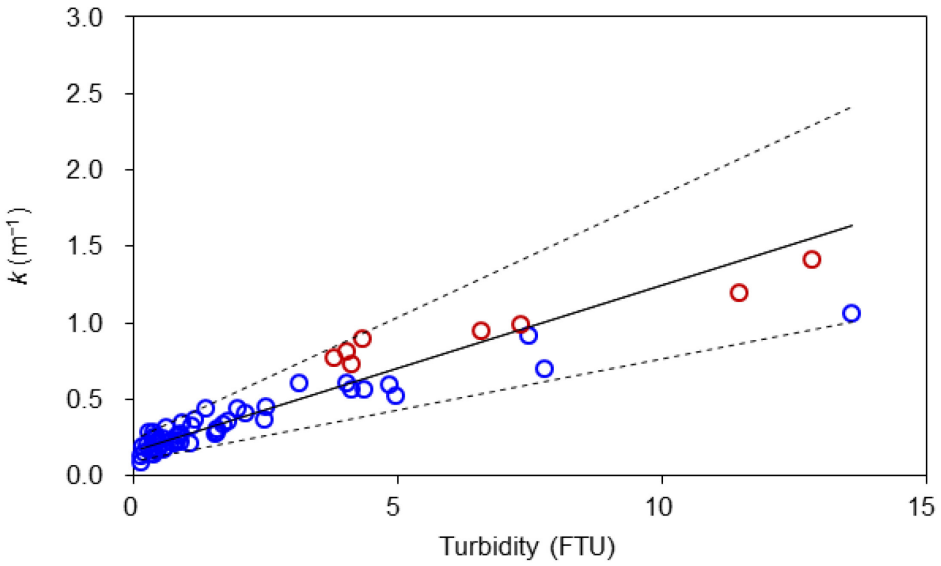

Fig. S3-1. Relationship between turbidity (FTU) and extinction coefficients (k, m^{-1}) in Tango Bay coastal zone. Red and blue circles indicate surface and bottom waters, respectively. A solid line represents the fitting model of a generalized linear model with identity link and gamma distribution. Dashed lines indicate the 95% prediction interval.

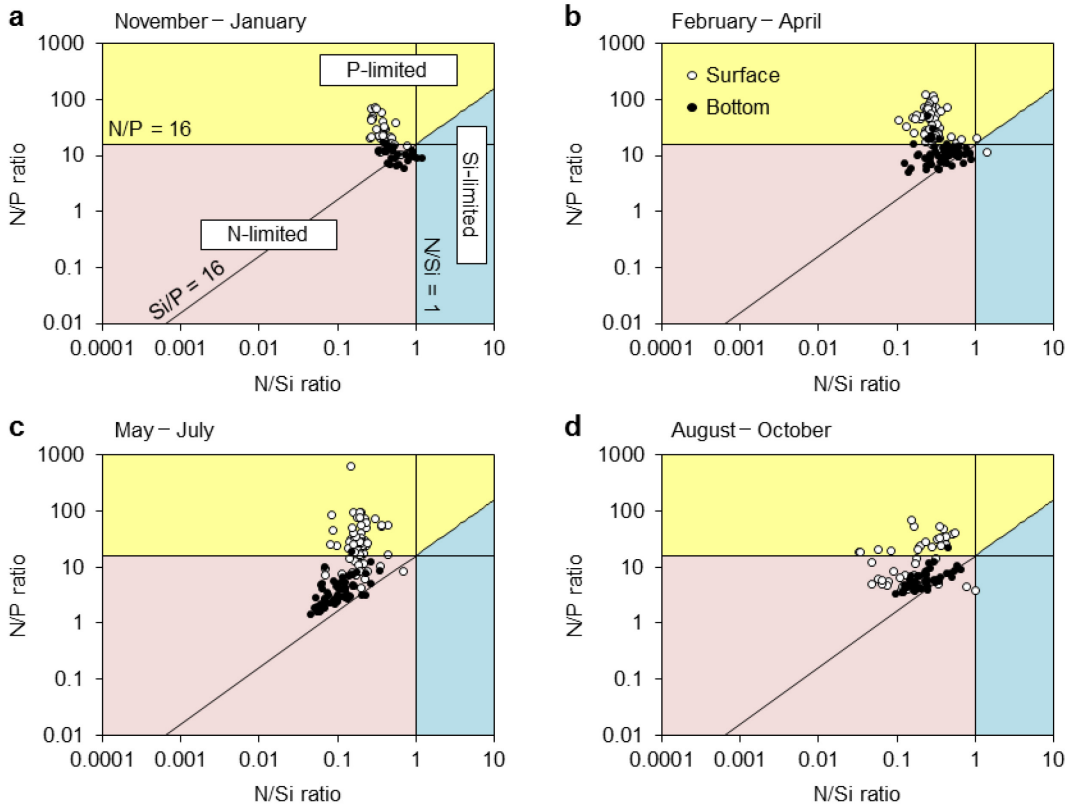

Fig. S3-2. N:P:Si molar ratios (log N/Si ratio vs. log N/P ratio) in the coastal waters of Tango Bay (**a**) from November to January, (**b**) from February to April, (**c**) from May to July, and (**d**) from August to October in 2010 and 2011. N, P and Si indicate DIN (NO_x + NH_4^+), PO_4^{3-} and DSi, respectively. NH_4^+ concentration data were obtained at stations T1 and T2 from July 2007 to March 2008 (monthly surveys; Watanabe et al., 2014). We used the mean NH_4^+ concentration for each period and layer. The three areas delimited by the Redfield ratio (N:P:Si = 16:1:16) are characterized by different potentially limiting nutrients. Open and closed circles indicate nutrient ratios in the surface and bottom water, respectively.

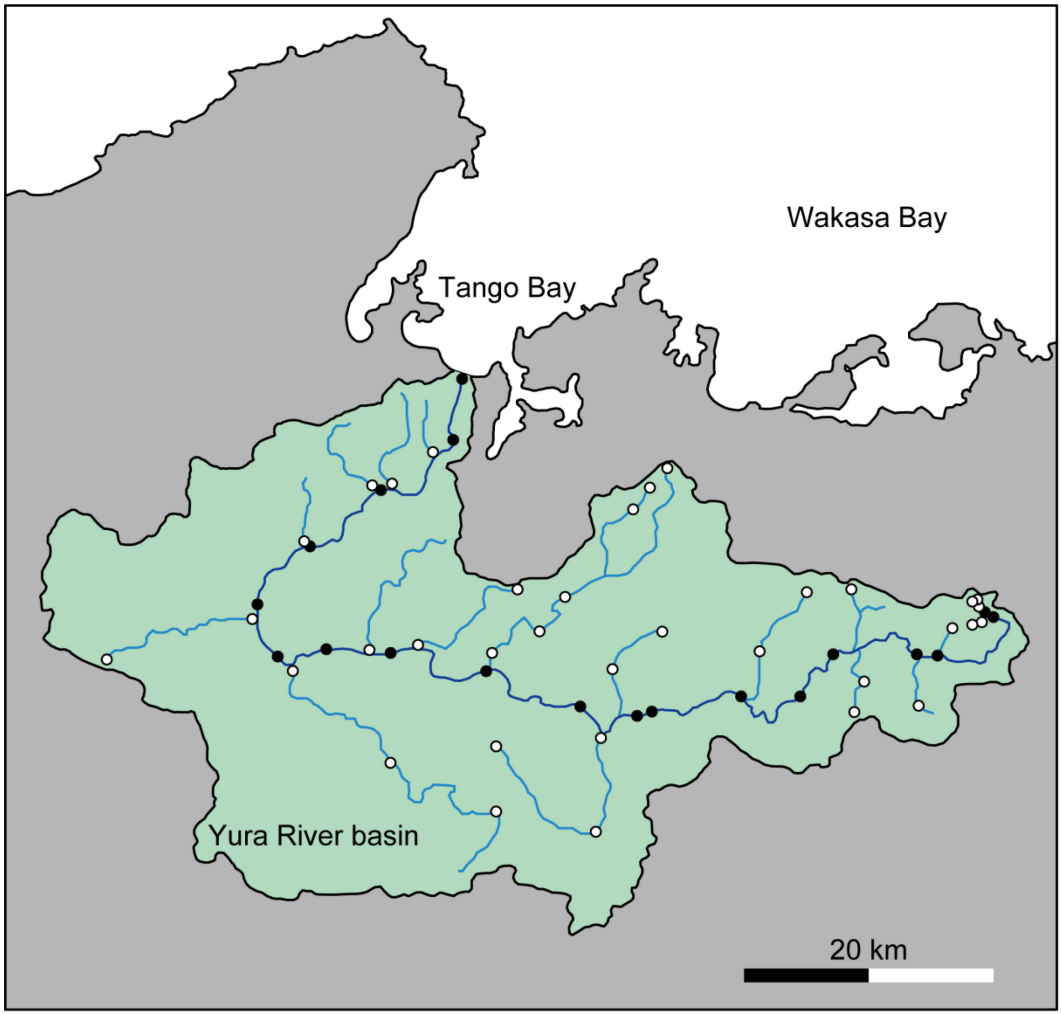

Fig. S4-1. Locations of the Yura River basin and the river and sream water sampling sites for the PARAFAC model. Closed and open circles indicate the main river and tributary stations, respectively. The PARAFAC model used in this study included 1,088 EEMs from the estuarine and coastal water samples taken during the field survey in this study and the stream and river water samples from the Yura River basin.

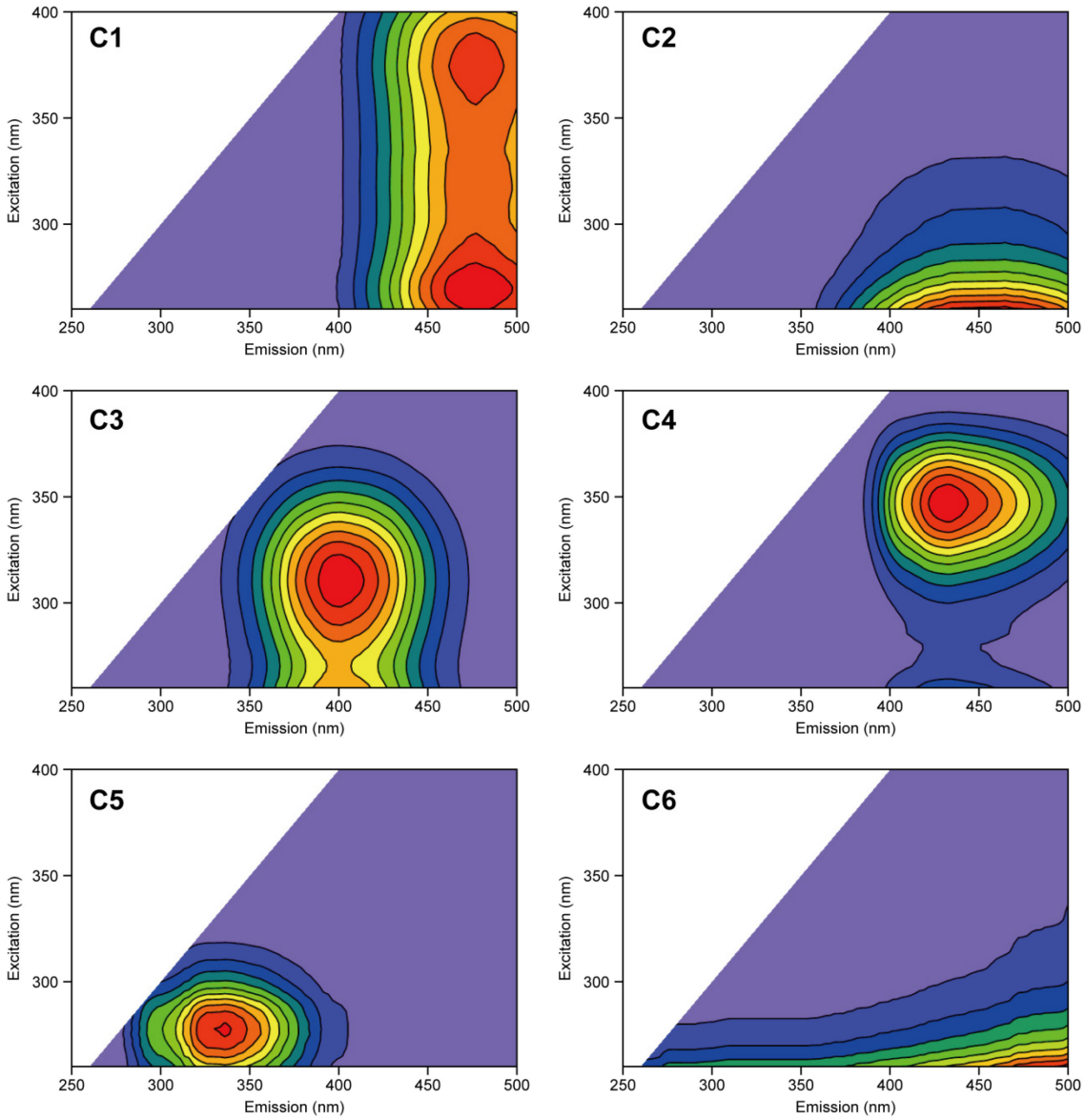

Fig. S4-2. Spectral characteristics of six PARAFAC components identified in the Yura River–Tango Bay system.

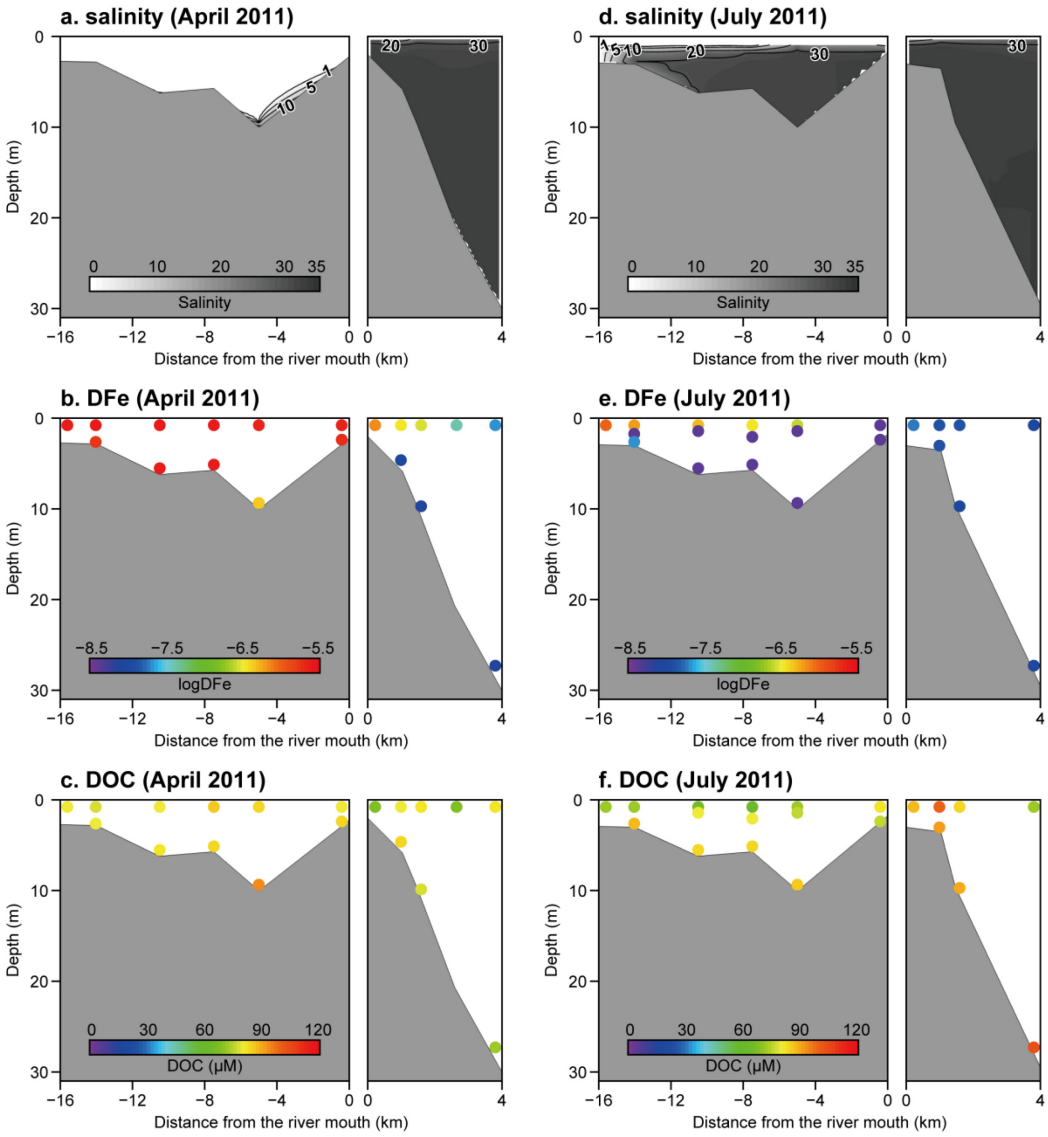

Fig. S4-3. Spatial distributions of salinity, dissolved iron (DFe), and dissolved organic carbon (DOC) concentrations in (**a**–**c**) April 2011 and (**d**–**f**) July 2011. The DFe concentration is represented as logDFe.

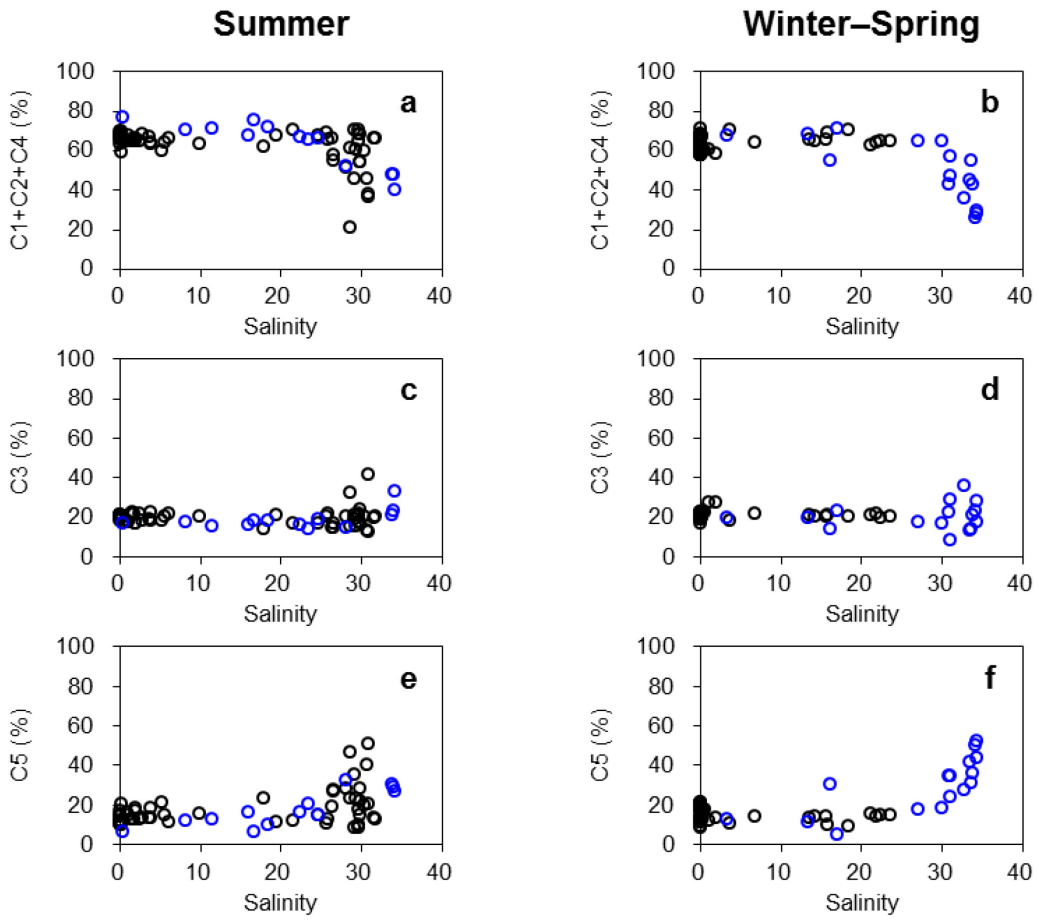

Fig. S4-4. Variations in the relative contribution of FDOM components (C1–C5) that result from PARAFAC analysis in the Yura River–Tango Bay system. Black and blue circles indicate the values obtained in the river and coastal zones, respectively.

Table S5-1. Isotopic and elemental signatures of OM sources.

Source	n	$\delta^{13}C$		$\delta^{15}N$		C/N	
		Mean	SD	Mean	SD	Mean	SD
Terrestrial OM	5	−28.3	1.1	2.4	0.5	12.5	0.6
Lagoon OM	3	−23.1	1.2	6.0	0.3	6.9	0.0
Coastal OM	3	−20.4	1.1	5.3	0.3	6.9	0.1
Phytobenthos-derived OM	12	−13.7	0.6	10.3	0.7	17.1	1.2
Seagrass	12	−10.9	1.9	10.7	1.3	21.6	2.3
epiphyte	12	−17.0	2.7	9.4	0.9	13.9	2.6